MASTER THESIS IN PHYSICS

First-principles investigation of charge and spin currents in magnetic nanostructures

by

Sascha Brinker

A thesis submitted to the Faculty of Mathematics, Computer Science and
Natural Sciences at RWTH Aachen University

October 2016

PGI-1 and IAS-1, Forschungszentrum Jülich

Supervisor
Prof. Dr. Samir Lounis

Eidesstattliche Versicherung

____________________________ ____________________________
Name, Vorname Matrikelnummer (freiwillige Angabe)

Ich versichere hiermit an Eides Statt, dass ich die vorliegende Arbeit/Bachelorarbeit/ Masterarbeit* mit dem Titel

____

____

____

selbständig und ohne unzulässige fremde Hilfe erbracht habe. Ich habe keine anderen als die angegebenen Quellen und Hilfsmittel benutzt. Für den Fall, dass die Arbeit zusätzlich auf einem Datenträger eingereicht wird, erkläre ich, dass die schriftliche und die elektronische Form vollständig übereinstimmen. Die Arbeit hat in gleicher oder ähnlicher Form noch keiner Prüfungsbehörde vorgelegen.

____________________________ ____________________________
Ort, Datum Unterschrift

*Nichtzutreffendes bitte streichen

Belehrung:

§ 156 StGB: Falsche Versicherung an Eides Statt

Wer vor einer zur Abnahme einer Versicherung an Eides Statt zuständigen Behörde eine solche Versicherung falsch abgibt oder unter Berufung auf eine solche Versicherung falsch aussagt, wird mit Freiheitsstrafe bis zu drei Jahren oder mit Geldstrafe bestraft.

§ 161 StGB: Fahrlässiger Falscheid; fahrlässige falsche Versicherung an Eides Statt

(1) Wenn eine der in den §§ 154 bis 156 bezeichneten Handlungen aus Fahrlässigkeit begangen worden ist, so tritt Freiheitsstrafe bis zu einem Jahr oder Geldstrafe ein.

(2) Straflosigkeit tritt ein, wenn der Täter die falsche Angabe rechtzeitig berichtigt. Die Vorschriften des § 158 Abs. 2 und 3 gelten entsprechend.

Die vorstehende Belehrung habe ich zur Kenntnis genommen:

____________________________ ____________________________
Ort, Datum Unterschrift

Contents

1. Introduction

Information technology is an ever-growing field, which is indispensable for contemporary society. The main foundation for the rapid growth of this field is the progress in data storage and data processing technologies, which are based on the progress in the field of magnetism. A milestone was the discovery of the giant magnetoresistance (GMR) by P. Grünberg [1] and A. Fert [2], which was awarded with the Nobel price in 2007. Nowadays the GMR is considered to be the groundbreaking starting point of the field of spintronics. In addition to the electron's charge, in spintronics the electron's spin degree of freedom is used as an information carrier, which has a lot of potential advantages in devices [3]. Besides spin and charge, the spin-orbit interaction provides a third ingredient, which gives rise to new properties and is conceptually important for the detection and the generation of spin-currents [4]. The new field of nano-spin-orbitronics aims to combine all the three degrees of freedom to investigate new nanotechnologies rising from fundamental physics. To push further the field of nano-spin-orbitronics, a deep theoretical understanding of the fundamental processes is needed. The main technological aim of the research in these fields is the optimization of data storage and data processing. Minimizing the size of the used devices enables a faster processing speed and higher storage densities. The smallest devices one can think of is a single atom, in which quantum mechanical effects play a crucial role. The storage and manipulation of magnetic information within small devices containing only a few atoms demands for a fundamental understanding of the ground state properties as well as the their excited states.

Regarding the ground state properties, the magnetic moment itself, which is a combination of the spin magnetic moment and the orbital magnetic moment, is of huge technological interest. On the one hand the spin magnetic moment, which originates from the many-body exchange interactions among the electrons, is well understood. On the other hand the orbital magnetic moment, which arises from the orbital motion of the electrons, is still part of current research. The orbital motion of the electrons is also responsible for charge currents, so there should be a deep connection between these and orbital magnetism.

Exciting the system induces a motion of the magnetic moment when brought from one state to the other, during which the magnetic moment interacts with the enviroment and emits spin currents [5]. Furthermore, spin currents can interact with the magnetic moments yielding for example current-induced magnetization switching [6]. My aim in this thesis is to lay the theoretical groundwork for the first-principles exploration of static and dynamical charge and spin currents, and to present my first numerical results on these topics.

The density functional theory (DFT) approach enables a theoretical investigation of the electronic structure of many-body systems from first principles. These include charge currents, spin currents and of course the orbital magnetic moment. To computationally solve the DFT problem there are several different methods – for example the plane wave approach, which is widely used for periodic systems. In this thesis I employ the Korringa-Kohn-Rostoker (KKR) Green function method, which can be utilized within a real space approach, thus being perfectly suited to describe finite nanostructures like single magnetic adatoms deposited on a surface.

Conventional DFT only describes static ground state properties. Therefore, ground state currents and the orbital magnetic moment are accessible. However, the investigation of dynamical spin currents requires access to excitations out of the ground state, which is accomplished by time-dependent DFT (TDDFT). Further simplifications can be done for small perturbations, which allow the treatment within linear response, such that the computational demands are decreased.

In this work, a KKR Green function-based method for the calculation of ground state charge and spin currents and dynamical spin currents is developed. Small magnetic nanostructures consisting of iron atoms deposited on platinum surfaces are used to enlighten the fundamental processes concerning the currents. The work is structured as follows:
In *chapter 2*, the physical background of charge currents and spin currents is discussed. The Schrödinger equation and a relativistic single-particle Hamiltonian are used to define the charge and spin currents via a continuity equation. In addition, the relation between charge currents and the orbital magnetic moment is discussed. *Chapter 3* gives an introduction of the DFT approach. Apart from the ground state spin-polarized DFT, the theory is extended to the time-dependent case. Furthermore, I discuss the description of currents within the DFT approach. In *chapter 4*, the KKR Green function method is discussed. Following the discussion of the most important concepts concerning the Green function, the KKR Green function method in the atomic sphere approximation is explained. Furthermore, a calculation scheme for ground state currents within the KKR approach is developed. The results of the ground state calculation are presented in *chapter 5*. Different nanostructures consisting of iron atoms deposited on platinum surfaces are used. In the first part charge currents resulting from spin-orbit coupling and the related orbital magnetic moments are shown. To support the understanding of the simulation results, a simple model describing an adatom on top of a surface is developed. In addition, charge currents resulting from a non-collinear alignment of the magnetic moment in an iron trimer ring are analyzed. In the second part, the ground state spin currents in an iron adatom on top of Pt(111) are presented. In *chapter 6*, I introduce the linear response theory, which is used to describe the dynamical spin-currents induced by a time-dependent external magnetic field. The induced spin-currents are closely related to the magnetic excitations, which are described by the magnetic susceptibility. I discuss the implementation within the KKR method and the time-dependent DFT approach. Furthermore, I present a phenomenological model – the Landau-Lifshitz-Gilbert model – which is used to describe magnetization dynamics. The resulting dynamical spin-currents in an iron adatom on top of Pt(111) are shown in *chapter 7*. The frequency dependence of the induced spin currents as well as the static limit of the simulation are discussed. Finally, in *chapter 8* the central results of this work are summarized and a short outlook is given.

2. Charge and spin currents

In this chapter we discuss the fundamental background for understanding charge and spin currents. Therefore, we start with the basic quantum mechanical equation – the Schrödinger equation. For the reason of simplicity we work within a single particle description, which is extended in the next chapter when the density functional theory is introduced.
We present a convenient definition of currents using continuity equations and include relativistic effects contributing to the current. At the end of the chapter, we discuss the orbital magnetic moment, which is a measurable quantity depending on groundstate charge currents.

2.1. Schrödinger equation

The time-dependent Schrödinger equation describes the dynamics of a non-relativistic quantum mechanical system by using the so called wavefunction $|\psi\rangle$

$$i\frac{\partial}{\partial t}|\psi(t)\rangle = \mathcal{H}|\psi(t)\rangle = \left(\vec{p}^{\,2} + v(\vec{r};t)\right)|\psi(t)\rangle \quad , \tag{2.1}$$

with the Hamiltonian $\mathcal{H}$, the momentum operator $\vec{p}$, the electron mass m and the potential $v(\vec{r},t)$. In the real space representation the momentum operator is given by $\langle\vec{r}|\vec{p}\rangle = -i\vec{\nabla}$, which yields

$$i\frac{\partial}{\partial t}\psi(\vec{r};t) = \left(-\vec{\nabla}^2 + v(\vec{r};t)\right)\psi(\vec{r};t) \quad . \tag{2.2}$$

The wavefunction enables the calculation of the expectation value of any physical observable described by a possibly time-dependent operator $\hat{A}_t$, which is given in the Schrödinger picture by

$$\langle\hat{A}_t\rangle_{|\psi(t)\rangle} = \langle\psi(t)|\hat{A}_t|\psi(t)\rangle \quad . \tag{2.3}$$

The most important property of the wavefunction is its relation to the probability density $n(\vec{r})$ of the electron

$$n(\vec{r};t) = \langle\psi(t)|\vec{r}\rangle\langle\vec{r}|\psi(t)\rangle = |\psi(\vec{r};t)|^2 \quad . \tag{2.4}$$

For a time-independent Hamiltonian it is sufficient to calculate the stationary solutions of the Schrödinger equation, which are given by the time-independent Schrödinger equation

$$\mathcal{H}|\psi\rangle = E|\psi\rangle \quad . \tag{2.5}$$

The eigenvalues E_n of the Hamiltonian are the energies of the system in the associated eigenstates $|\psi_n\rangle$. These eigenstates form a complete basis set $\{|\psi_n\rangle\}$, such that any state can be described by a linear combination of these eigenstates. The time evolution of the eigenstates follows from eq. (2.1)

$$|\psi_n(t)\rangle = e^{-iE_nt}|\psi_n(0)\rangle \quad . \tag{2.6}$$

Thus solving the time-independent Schrödinger equation is sufficient to describe every system and its time evolution for a time-independent Hamiltonian.

The Schrödinger equation in its presented form is only valid for spin-less particles without magnetic field. In this work we deal with magnetism, which demands for a proper description of the spin of a particle and of the magnetic field. In addition to the scalar potential an interaction with an external magnetic field $\vec{B}(\vec{r})$ and the corresponding vector potential $\vec{A}$ is possible. Furthermore, the introduction of two separate wave functions for the different spin configurations $\{\uparrow, \downarrow\}$ is needed. In total, for a spin 1/2-particle one finds the Pauli equation

$$i\frac{\partial}{\partial t}|\Psi(t)\rangle = \mathcal{H}|\Psi(t)\rangle = \left[\left(\boldsymbol{\vec{\sigma}} \cdot \left(\vec{p} - e\vec{A}(\vec{r};t)\right)\right)^2 + v(\vec{r};t)\right]|\Psi(t)\rangle \quad , \tag{2.7}$$

where $|\Psi(t)\rangle = \begin{pmatrix} \psi^{\uparrow}(t) \\ \psi^{\downarrow}(t) \end{pmatrix}$ is the so-called spinor, $\vec{A}$ is the vector potential which is related to the magnetic field $\vec{B} = \vec{\nabla} \times \vec{A}$ (see appendix B) and $\vec{\sigma}$ is the vector of Pauli matrices

$$\boldsymbol{\sigma}_x = \begin{pmatrix} 0 & 1 \\ 1 & 0 \end{pmatrix} \quad , \quad \boldsymbol{\sigma}_y = \begin{pmatrix} 0 & \text{-i} \\ \text{i} & 0 \end{pmatrix} \quad \text{and} \quad \boldsymbol{\sigma}_z = \begin{pmatrix} 1 & 0 \\ 0 & \text{-1} \end{pmatrix} \quad . \tag{2.8}$$

Using the commutation relations of the Pauli matrices the Pauli equation simplifies to

$$i\frac{\partial}{\partial t}|\Psi(t)\rangle = \left[\left(\vec{p} - e\vec{A}(\vec{r};t)\right)^2 - \mu_B \boldsymbol{\vec{\sigma}} \cdot \vec{B}(\vec{r};t) + v(\vec{r};t)\right]|\Psi(t)\rangle \quad , \tag{2.9}$$

where $\mu_B \boldsymbol{\vec{\sigma}} \cdot \vec{B}$ is the Zeeman term and $\mu_B = \frac{e\hbar}{2m}$ is the Bohr magneton.
In addition to the probability density, the solutions of the Pauli equation enable us to calculate the spin density:

$$\vec{m}(\vec{r};t) = \mu_B \langle\Psi(t)|\vec{r}\rangle \boldsymbol{\vec{\sigma}} \langle\vec{r}|\Psi(t)\rangle = \mu_B \Psi^{\dagger}(\vec{r};t) \boldsymbol{\vec{\sigma}} \Psi(\vec{r};t) \quad . \tag{2.10}$$

A more rigorous derivation of the Pauli equation can be done by taking the non-relativistic limit of the Dirac equation (see appendix C) which includes naturally the spin of the electron.
In the next section we discuss relativistic corrections to the presented Hamiltonian.

2.2. Relativistic corrections to the Schrödinger equation

The theory discussed in the previous section neglected any relativistic effects, since the Pauli equation itself is non-relativistic. To describe relativistic particles properly one has to start from the Dirac equation [7]. Fortunately, it is possible to derive relativistic corrections to the Schrödinger equation using an expansion of the Dirac equation (see Appendix C).
The Hamiltonian up to first order in the speed of light c is given by:

$$\begin{aligned} \mathcal{H} = \quad & \underbrace{\left(\boldsymbol{\vec{\sigma}} \cdot \left(\vec{p} - e\vec{A}\right)\right)^2}_{\text{kinetic energy (KE) + Zeeman}} + \underbrace{v}_{\text{Potential}} \underbrace{-\frac{1}{c^2}\left(\boldsymbol{\vec{\sigma}} \cdot \left(\vec{p} - e\vec{A}\right)\right)^4}_{\text{rel. corrections to KE}} \underbrace{-\frac{1}{2c^2}\left(\vec{\nabla} \cdot \vec{E}\right)}_{\text{Darwin term}} \\ + \quad & \underbrace{i\frac{\mu_B}{2c^2}\boldsymbol{\vec{\sigma}} \cdot \frac{\partial \vec{B}}{\partial t}}_{\text{interaction with time-dep. B-field}} + \underbrace{\frac{\mu_B}{c^2}\boldsymbol{\vec{\sigma}} \cdot \left(\vec{E} \times \left(\vec{p} - \vec{A}\right)\right)}_{\text{SOC term}} \end{aligned} \quad , \tag{2.11}$$

with $\vec{E}$ being the electric field, which originates in a solid from the atomic nuclei potential, so that the strongest fields are found around each atomic nucleus. Therefore the relativistic corrections are more important in the vicinity of the atomic nucleus.
Thus up to first order in c there are four different corrections to the Hamiltonian.
The first term is a relativistic correction to the kinetic energy and to the Zeeman term. The second term is the so called Darwin term, which is only important for s-like electrons with finite probability density at $\vec{r} = 0$. The third term describes an additional correction for time-dependent magnetic fields. The last term is the so called spin-orbit coupling (SOC) term.
For this work the SOC term is the most important one, since it couples the spin degree of freedom to the orbital degree of freedom, which is needed for finite ground state charge and spin currents. Furthermore, the SOC term is responsible for many interesting and important effects like the orbital magnetic moment, the mangetocrystalline anisotropy [8], the Rashba effect [9], the Dresselhaus effect [10] or Dzyaloshinskii-Moriya interactions [11, 12].
In the next section we connect the Schrödinger equation to charge and spin currents by using the continuity equation.

2.3. Continuity equation

The concept of continuity equations is used widely in different fields of physics, e.g. hydrodynamics or electrodynamics [13]. The underlying property of the systems is always a conservation law. In the case of the charge continuity equation it is the charge conservation law. Consider a charge distribution $\rho(\vec{r};t)$ in a volume $\mathcal{V}$ enclosed by a surface $\partial\mathcal{V}$ as shown in figure 2.1. The total charge Q in the volume is given by

$$Q(t) = \int_{\mathcal{V}} \mathrm{d}V \; \rho(\vec{r};t) \quad . \tag{2.12}$$

Due to charge conservation all transferred charge has to flow through the surface, since there can not be any source or sink inside the volume. By defining the current density $\vec{j}(\vec{r})$ by the flow of charges per unit time, the change of charge inside the volume is given by

$$\frac{\mathrm{d}Q(t)}{\mathrm{d}t} = \int_{\mathcal{V}} \mathrm{d}V \; \frac{\partial}{\partial t}\rho(\vec{r};t) = -\int_{\partial\mathcal{V}} \mathrm{d}A \; \hat{n}(\vec{r}) \cdot \vec{j}(\vec{r};t) \quad , \tag{2.13}$$

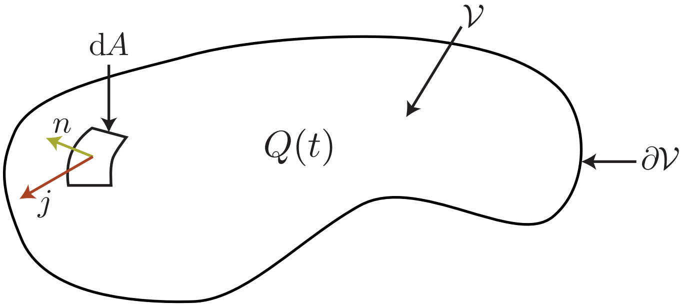

Figure 2.1.: Concept of a continuity equation: The change of the charge $Q(t)$ in a volume $\mathcal{V}$ is equal to the flow j through the surface $\partial\mathcal{V}$.

where $\hat{n}$ is the normal vector to the surface $\partial\mathcal{V}$.
Applying Gauss's theorem yields

$$\int_{\mathcal{V}} \mathrm{d}V \, \frac{\partial}{\partial t}\rho(\vec{r};t) = -\int_{\mathcal{V}} \mathrm{d}V \, \vec{\nabla}\cdot\vec{j}(\vec{r};t) \quad . \tag{2.14}$$

Since the volume $\mathcal{V}$ is arbitrary the integrands have to match pointwise which yields the differential form of the continuity equation:

$$\frac{\partial}{\partial t}\rho(\vec{r};t) + \vec{\nabla}\cdot\vec{j}(\vec{r};t) = 0 \quad . \tag{2.15}$$

Thus via the continuity equation we can connect changes in the density to the divergence of the current. Starting from the Schrödinger equation with relativistic corrections we can use a continuity equation to define currents in terms of the wavefunctions.

2.3.1. Charge continuity equation

For charge currents the proper starting point is the charge density, which is just the probability density $n = \Psi^\dagger\Psi$ defined in section 2.1 multiplied by the electric charge e. The time derivative of the charge density can be connected to the Hamiltonian via the Schrödinger equation (2.2)

$$\begin{aligned} i\partial_t\rho = ie\partial_t\left(\Psi^\dagger\Psi\right) &= e\left[\Psi^\dagger\left(i\partial_t\Psi\right) + \left(i\partial_t\Psi^\dagger\right)\Psi\right] && (2.16)\\ &= e\left[\Psi^\dagger\overrightarrow{\mathcal{H}}\Psi - \Psi^\dagger\overleftarrow{\mathcal{H}}\Psi\right] && (2.17)\\ &= -i\vec{\nabla}\cdot\vec{j} \quad , && (2.18) \end{aligned}$$

where we used the $\overleftarrow{\mathcal{H}}$ notation to indicate the action of $\mathcal{H}$ to the left. The action of the momentum operator to the left is given by

$$\left(\vec{p}\Psi\right)^\dagger = \vec{p}^{\,\dagger}\Psi^\dagger = -\Psi^\dagger\overleftarrow{p} \quad . \tag{2.19}$$

First, let us consider the non-relativistic Pauli Hamiltonian (2.9). The kinetic energy yields

$$\begin{aligned} \Psi^\dagger\overrightarrow{\mathcal{H}}_{\text{kin}}\Psi - \Psi^\dagger\overleftarrow{\mathcal{H}}_{\text{kin}}\Psi &= \left[\Psi^\dagger\left(\vec{p} - e\vec{A}\right)^2\Psi - \Psi^\dagger\left(-\overleftarrow{p} - e\vec{A}\right)^2\Psi\right] && (2.20)\\ &= \left[\Psi^\dagger\vec{p}^{\,2}\Psi - \Psi^\dagger\overleftarrow{p}^{\,2}\Psi\right] - e\vec{A}\left[\Psi^\dagger\vec{p}\Psi + \Psi^\dagger\overleftarrow{p}\Psi\right] && (2.21)\\ &= -\frac{i}{e}\vec{\nabla}\cdot\left\{\underbrace{e\left[\Psi^\dagger\vec{p}\Psi - \Psi^\dagger\overleftarrow{p}\Psi\right]}_{\vec{j}_{\text{para}}}\underbrace{-e^2\vec{A}\Psi^\dagger\Psi}_{\vec{j}_{\text{dia}}}\right\} \quad , && (2.22) \end{aligned}$$

where $\vec{j}_{\text{para}}$ is the paramagnetic current and $\vec{j}_{\text{dia}}$ is the diamagnetic current. In the real space representation the paramagnetic current operator can be written as:

$$\hat{\vec{j}}_{\text{para}} = -i\mu_B\left(\overrightarrow{\nabla} - \overleftarrow{\nabla}\right) \quad . \tag{2.23}$$

These are the only finite contributions evolving from the non-relativistic Schrödinger equation. From eq. (2.17) it is clear, that only the parts of the Hamiltonian including a momentum operator which acts explicitly on the wavefunction contribute to the current. The potential and the Zeeman

term do not contribute, because they do not depend on the momentum operator.
However, one can show that the Zeeman term yields a finite current, which does not contribute to the divergence of the current [14]:

$$\vec{j}_{\text{Zeeman}} = \mu_B \vec{\nabla} \times \left(\Psi^\dagger \vec{\boldsymbol{\sigma}} \Psi \right) = \vec{\nabla} \times \vec{m} \quad . \tag{2.24}$$

Let us consider the terms of the Hamiltonian with relativistic corrections from eq. (2.11). The Darwin term and the interaction with a time-dependent magnetic field do not contribute to the divergence of the current. The relativistic corrections to the kinetic energy contribute to the current, but they are not considered in more detail in this work, since they are a small correction with the same structure as the non-relativistic paramagnetic current.
The SOC term is linear in the momentum and therefore contributes to the charge current:

$$\begin{aligned} \Psi^\dagger \overrightarrow{\mathcal{H}}_{\text{SOC}} \Psi - \Psi^\dagger \overleftarrow{\mathcal{H}}_{\text{SOC}} \Psi =& \frac{\mu_B}{c^2} \Psi^\dagger \left[\vec{\boldsymbol{\sigma}} \cdot \left(\vec{E} \times \left(\vec{p} - \vec{A} \right) \right) - \vec{\boldsymbol{\sigma}} \cdot \left(\left(\overleftarrow{p} + \vec{A} \right) \times \vec{E} \right) \right] \Psi & (2.25) \\ =& \frac{\mu_B}{c^2} \Psi^\dagger \left[\epsilon_{abc} \boldsymbol{\sigma}^a E^b \left(\vec{p} + \overleftarrow{p} \right)^c \right] \Psi & (2.26) \\ =& - i \vec{\nabla} \cdot \left[\frac{\mu_B}{c^2} \Psi^\dagger \left(\vec{\boldsymbol{\sigma}} \times \vec{E} \right) \Psi \right] = -i \vec{\nabla} \cdot \underbrace{\left[\frac{1}{c^2} \vec{m} \times \vec{E} \right]}_{\vec{j}_{\text{SOC}}} \quad . & (2.27) \end{aligned}$$

Thus in total the charge continuity equation is given by

$$\partial_t n + \vec{\nabla} \cdot \left[\vec{j}_{\text{para}} + \vec{j}_{\text{dia}} + \vec{j}_{\text{Zeeman}} + \vec{j}_{\text{SOC}} \right] = 0 \quad . \tag{2.28}$$

2.3.2. Spin continuity equation

Another important continuity equation follows from the spin density $\vec{m} = \mu_B \Psi^\dagger \vec{\boldsymbol{\sigma}} \Psi$. A crucial difference to the charge density is that the magnetization density is a vector quantity by itself. Thus one can set up a continuity equation for each component of the magnetization yielding a spin current for each polarization, such that in total the spin current is a tensor. Starting from the Schrödinger equation one finds for the time derivative of the a-component of the magnetization

$$i \partial_t m^a = \mu_B \partial_t \Psi^\dagger \boldsymbol{\sigma}^a \Psi = \mu_B \Psi^\dagger \left[\boldsymbol{\sigma}^a \overrightarrow{\mathcal{H}} - \overleftarrow{\mathcal{H}} \boldsymbol{\sigma}^a \right] \Psi \quad , \quad \text{with} \quad a = \{x, y, z\} \quad . \tag{2.29}$$

The approach is similar to the case of charge currents, but now the commutation relations of the Pauli matrices have to be considered, which yields additional terms.
The kinetic energy yields the paramagnetic and the diamagnetic term of the a-polarized spin current:

$$\begin{aligned} \vec{j}^{\,a}_{\text{para}} =& \mu_B \Psi^\dagger \boldsymbol{\sigma}^a \left[\vec{p} - \overleftarrow{p} \right] \Psi = -i \mu_B \Psi^\dagger \boldsymbol{\sigma}^a \left[\vec{\nabla} - \overleftarrow{\nabla} \right] \Psi \quad , & (2.30) \\ \vec{j}^{\,a}_{\text{dia}} =& - 2 \vec{A} \Psi^\dagger \boldsymbol{\sigma}^a \Psi \quad . & (2.31) \end{aligned}$$

The non-magnetic potential v does not contribute to the spin currents, since it commutes with the Pauli matrices and it is independent of the momentum. However, the Zeeman term does not vanish:

$$\mu_B^2 \Psi^\dagger \left[-\boldsymbol{\sigma}^a \vec{\boldsymbol{\sigma}} \cdot \vec{B} + \vec{\boldsymbol{\sigma}} \cdot \vec{B} \boldsymbol{\sigma}^a \right] \Psi = 2 i \mu_B^2 \Psi^\dagger \left(\vec{\boldsymbol{\sigma}} \times \vec{B} \right)^a \Psi = 2 i \mu_B \left(\vec{m} \times \vec{B} \right)^a \quad . \tag{2.32}$$

The resulting term – the so called spin torque – cannot be written as the divergence of a current. The relativistic corrections in eq. (2.11) give rise to an additional current and an additional torque. The interaction with the time-dependent magnetic field yields a torque:

$$i\frac{\mu_B^2}{2c^2}\Psi^\dagger\left[\boldsymbol{\sigma}^a\vec{\boldsymbol{\sigma}}\cdot\frac{\partial\vec{B}}{\partial t}-\vec{\boldsymbol{\sigma}}\cdot\frac{\partial\vec{B}}{\partial t}\boldsymbol{\sigma}^a\right]\Psi=-\frac{\mu_B^2}{c^2}\Psi^\dagger\left(\frac{\partial\vec{B}}{\partial t}\times\vec{\boldsymbol{\sigma}}\right)^a\Psi=-\frac{\mu_B}{c^2}\left(\frac{\partial\vec{B}}{\partial t}\times\vec{m}\right)^a \quad . \tag{2.33}$$

The SOC term gives a correction to the spin current and a torque:

$$\frac{\mu_B}{c^2}\Psi^\dagger\left[\boldsymbol{\sigma}^a\vec{\boldsymbol{\sigma}}\cdot\left(\vec{E}\times\left(\vec{p}-e\vec{A}\right)\right)-\vec{\boldsymbol{\sigma}}\cdot\left(\left(\overleftarrow{p}+e\vec{A}\right)\times\vec{E}\right)\boldsymbol{\sigma}^a\right]\Psi \tag{2.34}$$

$$=\frac{\mu_B}{c^2}\left\{-i\partial_c\Psi^\dagger\left[\epsilon_{abc}E_b\right]\Psi-i\Psi^\dagger\left[\epsilon_{abc}\partial_bE_c\right]\Psi+iE_kj_k^a-iE_aj_k^k\right\} \tag{2.35}$$

$$=-i\vec{\nabla}\cdot\underbrace{\left[\frac{\mu_B}{c^2}n\epsilon_{abc}E_b\hat{e}_c\right]}_{\vec{j}^a_{\mathrm{SOC}}}+i\underbrace{\frac{\mu_B}{c^2}\left[-n\left(\vec{\nabla}\times\vec{E}\right)^a+\vec{E}\cdot\vec{j}^a-E^aj_k^k\right]}_{T^a_{\mathrm{SOC}}} \tag{2.36}$$

where we defined $j_k^a=j_{k,\mathrm{para}}^a+j_{k,\mathrm{dia}}^a$ as the sum of the paramagnetic and diamagnetic spin currents with a-polarization in the direction k and T^a_{SOC} as the spin-orbit coupling contribution to the torque.

In total, the continuity equation of the magnetization is given by

$$\frac{\partial m^a}{\partial t}+\vec{\nabla}\cdot\left[\vec{j}^a_{\mathrm{para}}+\vec{j}^a_{\mathrm{dia}}+\vec{j}^a_{\mathrm{SOC}}\right]=-2\mu_B\left(\vec{m}\times\vec{B}\right)^a-\frac{\mu_B}{c^2}\left(\frac{\partial\vec{B}}{\partial t}\times\vec{m}\right)^a+T^a_{\mathrm{SOC}} \tag{2.37}$$

2.4. Orbital magnetic moment

The total magnetic moment in a magnetic solids can be separated in two parts – the spin magnetic moment (SMM) and the orbital magnetic moment (OMM) [15]. The spin magnetic moment is roughly speaking generated by the population imbalance between the spin up and the spin down electrons, whereas the orbital magnetic moment is generated by the motion of the electrons. In most technological relevant magnetic materials the spin magnetic moment is much larger than the orbital magnetic moment, e.g. in bulk iron the orbital moment is only a few percent of the total magnetic moment. Therefore, the orbital magnetic moment was overlooked for a long period of time. However, it is a part of the total magnetic moment and for a precise investigation of any material it has to be considered. Furthermore, it is not small for all systems – there are even systems in which the orbital magnetic moment cancels the spin magnetic moment [16] and systems where the net magnetic moment is purely of orbital origin [17]. In addition, there are a few effects being directly related to the orbital magnetization and its derivatives [15].

In the previous sections we discussed charge and spin currents and their emergence in continuity equations. The charge current describes a flow of charge mediated by the electrons. From classical electrodynamics it is known that a moving electron generates a magnetic moment $\vec{m}_{\mathrm{orb}}$ – the orbital magnetic moment – which is proportional to the angular moment $\vec{L}$ of the electron [13]:

$$\vec{m}_{\mathrm{orb}}=\mu_B\vec{L}=\mu_B\vec{r}\times\vec{p} \quad . \tag{2.38}$$

Thus, there should be a connection between the charge current describing the motion of the electrons and the orbital magnetic moment generated by this motion.

Starting from the quantum mechanical expectation value of the angular momentum one finds:

$$\mu_B\langle\vec{L}\rangle = \mu_B \int \mathrm{d}\vec{r}\ \Psi^\dagger \left[\frac{\vec{L}+\vec{L}^\dagger}{2}\right]\Psi \tag{2.39}$$

$$= \mu_B \int \mathrm{d}\vec{r}\ \vec{r}\times\left[\Psi^\dagger \frac{\vec{p}-\overleftarrow{p}}{2}\Psi\right] \tag{2.40}$$

$$= \frac{1}{2}\int \mathrm{d}\vec{r}\ \vec{r}\times\vec{j}_{\mathrm{para}} \quad . \tag{2.41}$$

Thus the orbital magnetic moment is given by the integral of the cross product of $\vec{r}$ and the paramagnetic charge current $\vec{j}_{\mathrm{para}}$.

The calculation shown above works fine for finite systems. However, for periodic infinite systems, e.g. a bulk solid or an infinite two dimensional slab, the method breaks down. The main problem are the charge currents, which are periodically repeated so that there is no spatial decay, even if the currents are bound within the unit cell. Therefore, the integral in eq. (2.41) does not converge. The breakdown can also be explained in another perspective: The common solution of the Schrödinger equation for periodic systems are so-called Bloch states, which are extended functions. Within this Bloch states, the position operator is ill-defined, so that the evaluation of the angular momentum operator is not possible via eq. (2.39).

Another problem occurs, when we relate the orbital magnetic moment to the charge current via the Maxwell equations [18]:

$$\vec{\nabla}\times\vec{m}_{\mathrm{orb}} = \vec{j}_{\mathrm{para}} \quad , \tag{2.42}$$

which shows that $\vec{m}_{\mathrm{orb}}$ and

$$\vec{m}'_{\mathrm{orb}}(\vec{r}) = \vec{m}_{\mathrm{orb}}(\vec{r}) + \vec{m}^0_{\mathrm{orb}} + \vec{\nabla}\xi(\vec{r}) \quad , \tag{2.43}$$

yield the same ground state current. For finite systems the orbital magnetic moment has to vanish for $\vec{r}\to\infty$ so that the orbital magnetic moment in (2.41) is well-defined.

To overcome the discussed problems a couple of theories were developed, which are combined in *the modern theory of orbital magnetism.* One approach being applicable for insulators is to use localized Wannier functions to evaluate eq. (2.39) in reciprocal space [19, 20]. In the set of exponentially localized Wannier functions the position operator is well-defined. In this approach two contributions to the orbital magnetic moment arise – a local contribution and an itinerant surface contribution, which is even relevant in the bulk. After finding both contributions a transformation back to the Bloch states can be done, so that the calculation of the orbital magnetic moment is even possible using the common Bloch states.

However, in this work we do not consider periodic systems but restrict ourselves to small finite clusters with magnetic adatoms, in which the modern theory of orbital magnetism is not applicable, since it is designed for periodic systems.

In this chapter we presented the three main observables discussed in this work. We showed how to calculate charge currents, spin currents and orbital magnetic moments within a single particle description. However, the simulation of real solids demands a treatment of all particles and their interactions. For this purpose, in the next chapter the density functional theory is discussed.

3. Density functional theory

The density functional theory (DFT) is a scheme for calculating the electronic ground state properties of a many-body system. In this chapter we will discuss the ground state DFT as well as its time-dependent extension which is used for the linear response calculations in this work. The following chapter is based on the book of Martin [21].

3.1. Many-body Schrödinger equation

The time-dependent Schrödinger equation of an non-relativistic N-particle system is given by

$$i\frac{\partial}{\partial t}\psi(\vec{r_1},...,\vec{r_N};t) = \mathcal{H}\ \psi(\vec{r_1},...,\vec{r_N};t) \quad , \tag{3.1}$$

where $\mathcal{H}$ is the many-body Hamiltonian and $\psi(\vec{r_1},...,\vec{r_N};t)$ is the many-body wavefunction.
For a static system not evolving in time the Schrödinger equation simplifies to its time-independent version:

$$\mathcal{H}\ \psi(\vec{r_1},...,\vec{r_N};t) = E\ \psi(\vec{r_1},...,\vec{r_N};t) \quad . \tag{3.2}$$

For an exact solution one has to consider all the particles (electrons and nuclei) and their interactions in the Hamiltonian. A first simplification is given by the so called Born-Oppenheimer approximation which decouples the electronic motion from the nuclear motion [22]. The motivation is that the nuclear mass is more than three orders of magnitude larger than the electronic mass. Therefore the electron system evolves much faster than the nuclei system and the kinetic energy of the nuclei can be neglected. Thus the electrons can be considered as a system inside a potential arising from a static nuclear configuration.
Denoting the electron positions with $\vec{r_i}$ and the nuclei positions with $\vec{R_j}$ the Hamiltonian of an N-electron system is given by

$$\mathcal{H} = -\sum_i \nabla_i^2 + \frac{1}{2}\sum_{i\neq j} w(\vec{r_i},\vec{r_j}) + \sum_i v(\vec{r_i};\{\vec{R_j}\}) \quad , \tag{3.3}$$

with the kinetic energy operator of the electron system

$$T = -\sum_i \nabla_i^2 \quad , \tag{3.4}$$

the electron-electron interaction described by a Coulomb term

$$W = \sum_{i\neq j} w(\vec{r_i},\vec{r_j}) = \sum_{i\neq j}\frac{1}{|\vec{r_i}-\vec{r_j}|} \quad , \tag{3.5}$$

and the potential containing the Coulomb interaction of the electrons with the nuclei

$$V = \sum_i v(\vec{r_i};\{\vec{R_j}\}) = \sum_i\sum_j \frac{-2Z_j}{|\vec{r_i}-\vec{R_j}|} = \sum_i v^{\text{ext}}(\vec{r_i}) \quad . \tag{3.6}$$

The electron density $n(\vec{r};t)$ can be written as

$$n(\vec{r};t) = \langle\psi(t)|\sum_{i=1}^{N}\delta(\vec{r}-\vec{r_i})|\psi(t)\rangle = \int \mathrm{d}\vec{r_2}...\mathrm{d}\vec{r_N}\ |\psi(\vec{r},\vec{r_2},\dots,\vec{r_N};t)|^2 \quad , \tag{3.7}$$

where $\vec{r_1},...,\vec{r_N}$ is the set of particle positions .
Even if we can easily write down the many-body Schrödinger equation it is not solvable analytically for more than two particles. Also numerically, solving the many-body Schrödinger equation is a computationally demanding task. Even for very simple systems with only a few electrons the storage of the wave function becomes nearly impossible on modern computers, since the wave function has to be calculated on a $3N$-dimensional grid. Assume for example a very coarse grid consisting of 10 points in every dimension. This yields an array of 10^{3N} numbers just to store the wavefunction, which becomes impossible for reasonable sized systems.
In the next section we introduce the density functional theory, which overcomes these computational problems.

3.2. Ground state density functional theory

3.2.1. Hohenberg-Kohn theorem

The basic theoretical foundation of DFT is the Hohenberg-Kohn theorem [23]. It consists of two parts, which state that

- for any system of interacting particles with a non-degenerated groundstate, the external potential $v^{\mathrm{ext}}(\vec{r})$ is, up to a constant, uniquely determined by the groundstate density $n_0(\vec{r})$

and

- the energy is a universal functional of the density, which is minimized for the groundstate density n_0.

The first part of the theorem can be shown by a contradiction. Starting from two different systems with non-degenerated groundstates under the influence of different external potentials

$$v^{(1),\mathrm{ext}} - v^{(2),\mathrm{ext}} \neq \mathrm{const.} \quad , \tag{3.8}$$

one can show that also the groundstate densities of the systems have to differ. Thus there is a one-to-one correspondence between the groundstate density and the external potential.

The second part of the Hohenberg-Kohn theorem states that the energy is a universal functional of the density. It can be shown that the kinetic energy $T[n]$ and the interaction energy of the electrons $W[n]$ are both functionals of the density being independent of the external potential.

$$\begin{align} E[n] &= T[n] + W[n] + V[n] \tag{3.9} \\ &= T[n] + W[n] + \int \mathrm{d}\vec{r}\, v^{\mathrm{ext}}(\vec{r})n(\vec{r}) \quad . \tag{3.10} \end{align}$$

Since the groundstate is defined by being the state of lowest energy, the energy functional is minimized for the groundstate density.

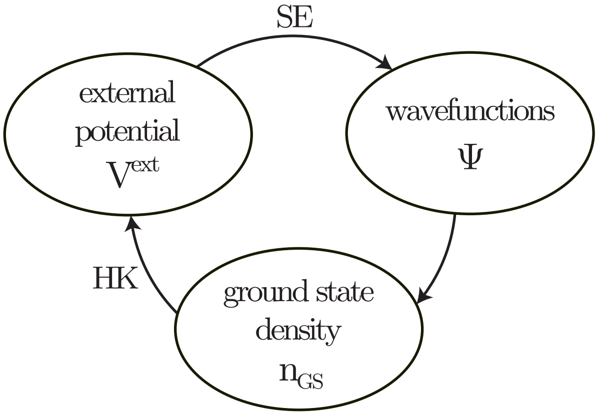

Figure 3.1.: The DFT principle in a simplified picture. The external potential determines all wavefunctions and especially the unique ground state wavefunction via the Schrödinger (SE) equation. The ground state wavefunction determines directly the ground state density. The Hohenberg-Kohn (HK) theorem closes the loop by stating that the external potential is uniquely determined by the ground state density.

In total, it follows that the groundstate density determines all properties of the system. In principle even excited states are determined by the groundstate density. This can be seen from the closed loop shown in figure 3.1. The groundstate density determines uniquely the external potential and via the Schrödinger equation this gives access to all properties and states of the system.

As the preceding example shows the Hohenberg-Kohn theorem might be of huge theoretical interest, but it does not state anything on how to solve the Schrödinger equation. For this purpose in the next section we discuss the Kohn-Sham equations which enable us to solve the Schrödinger equation for a many-particle system.

3.2.2. Kohn-Sham equations

The ansatz of Kohn and Sham [24] was the groundbreaking starting point of the nowadays widely and successfully used DFT scheme.
Instead of solving the Schrödinger equation for a many-body system Kohn and Sham showed that there is an equivalent auxiliary system of independent particles having the same ground state density as the initial many-body system. Via the Hohenberg-Kohn theorem we know that the many-body system is uniquely determined by its ground state density. Thus by using the idea of Kohn and Sham one can reduce the complexity of the problem dramatically by solving the equations for a system of independent particles with the same ground state density as the many-body system.
The Kohn-Sham (KS) N-particle system can be described by the KS Hamiltonian

$$\mathcal{H}^{\mathrm{KS}} = -\nabla^2 + v^{\mathrm{KS}}(\vec{r}) \quad , \tag{3.11}$$

and the Schrödinger equation

$$\mathcal{H}^{\mathrm{KS}}\phi_i(\vec{r}) = E_i\phi_i(\vec{r}) \quad , \tag{3.12}$$

with the KS orbitals $\phi_i(\vec{r})$ yielding the ground state density

$$n_0(\vec{r}) = \sum_{i=1}^{N} |\phi_i(\vec{r})|^2 \quad . \tag{3.13}$$

The KS potential v^{KS} is constructed such that the system yields the same ground state density as the initial many-body system. It is defined by

$$v^{\mathrm{KS}}(\vec{r}) = v^{\mathrm{ext}}(\vec{r}) + v^{\mathrm{Hartree}}(\vec{r}) + v^{\mathrm{xc}}(\vec{r}) \quad , \tag{3.14}$$

where v^{ext} is the external (ionic) potential, v^{Hartree} is the Hartree potential and v^{xc} is the exchange-correlation potential. The external potential is known from the many-body system. The Hartree potential is the functional derivative of the Hartree energy being a functional of the density

$$v^{\mathrm{Hartree}}(\vec{r}) = \frac{\delta E^{\mathrm{Hartree}}[n]}{\delta n(\vec{r})} = \frac{\delta}{\delta n(\vec{r})} \int \mathrm{d}\vec{r}\mathrm{d}\vec{r}' \, \frac{n(\vec{r})n(\vec{r}')}{|\vec{r} - \vec{r}'|} = 2 \int \mathrm{d}\vec{r}' \, \frac{n(\vec{r}')}{|\vec{r} - \vec{r}'|} \quad . \tag{3.15}$$

Thus the only unknown is the exchange correlation potential $v^{\mathrm{xc}}(\vec{r}) = \frac{\delta E^{\mathrm{xc}}[n]}{\delta n(\vec{r})}$. We can find an expression for the exchange correlation energy by comparing the energies of the many-body system with the KS system:

$$E^{\mathrm{xc}}[n] = T[n] + W[n] - \left(T^{\mathrm{KS}}[n] + E^{\mathrm{Hartree}}[n]\right) \quad . \tag{3.16}$$

However, at this point the solution of E^{xc} still requires the full solution of the many-body system.

3.2.3. Spin density functional theory

In the previous sections we discussed the basics of DFT for non-magnetic solids. Indeed, many areas of research and many technologies are based on magnetic materials demanding for a proper description of the spin, which is an intrinsic property of the electrons.

Starting from the Schrödinger equation, the many-body wavefunction depends on the particle positions and the spin of each particle. Furthermore, the spin of the electrons can couple to an external magnetic field which modifies the Hamiltonian:

$$\delta\mathcal{H} = -\mu_B \sum_i \vec{\boldsymbol{\sigma}} \cdot \vec{B}^{\mathrm{ext}}(\vec{r}_i) \quad , \tag{3.17}$$

where $\vec{\boldsymbol{\sigma}}$ is the vector of Pauli matrices. In addition to the electron density, for magnetic systems the spin density $\vec{m}(\vec{r};t)$ characterizes the ground state of the system:

$$\vec{m}(\vec{r};t) = \mu_B \langle\Psi(t)| \sum_{i=1}^{N} \delta(\vec{r} - \vec{r_i})\vec{\boldsymbol{\sigma}}|\Psi(t)\rangle \quad . \tag{3.18}$$

It is straightforward to generalize the DFT scheme to magnetic materials.
First of all, one can show that there is a one-to-one correspondence between the external potentials and the set of the four ground state density components $(n_0, \vec{m}_0)$. Furthermore, the energy is a functional of the charge density and the spin density,

$$\begin{aligned} E[n,\vec{m}] &= T[n,\vec{m}] + W[n,\vec{m}] + V[n,\vec{m}] && (3.19) \\ &= T[n,\vec{m}] + W[n,\vec{m}] + \int \mathrm{d}\vec{r} \left[v^{\mathrm{ext}}(\vec{r})n(\vec{r}) - \vec{B}^{\mathrm{ext}}(\vec{r}) \cdot \vec{m}(\vec{r})\right] \quad , && (3.20) \end{aligned}$$

which is minimized for the ground state densities. In total, this concludes the Hohenberg-Kohn theorem for magnetic systems.
Even more important than the Hohenberg-Kohn theorem are the spin-dependent Kohn-Sham equations. The existence of a system of non-interacting spin-dependent particles described by the Kohn-Sham Hamiltonian,

$$\mathcal{H}^{\mathrm{KS}} = -\nabla^2 + v^{\mathrm{KS}}(\vec{r}) - \vec{\boldsymbol{\sigma}} \cdot \vec{B}^{\mathrm{KS}}(\vec{r}) \quad , \tag{3.21}$$

with the same ground state density $n(\vec{r})$ and ground state magnetization density $\vec{m}(\vec{r})$ as the initial interacting spin dependent system can be shown. The energy of the Kohn-Sham system is given by

$$E[n,\vec{m}] = T^{\mathrm{KS}}[n,\vec{m}] + E^{\mathrm{Hartree}}[n] + \int \mathrm{d}\vec{r} \ \left[v^{\mathrm{ext}}(\vec{r})n(\vec{r}) - \vec{B}^{\mathrm{ext}}(\vec{r}) \cdot \vec{m}(\vec{r})\right] + E^{\mathrm{xc}}[n,\vec{m}] \quad . \tag{3.22}$$

The minimization of this energy yields an expression for the exchange-correlation magnetic field which is the only new quantity in comparison with the spin-independent case:

$$\vec{B}^{\mathrm{KS}}(\vec{r}) = \mu_B \vec{B}^{\mathrm{ext}}(\vec{r}) + \frac{\delta E^{\mathrm{xc}}[n,\vec{m}]}{\delta \vec{m}(\vec{r})} \quad . \tag{3.23}$$

These equations show the basic relation between the interacting and the KS system, but they do not help with simplifying the problem. In principle one still has to solve the many-body problem to get the functional form of the interaction $W[n,\vec{m}]$ and the kinetic energy $T[n,\vec{m}]$. To overcome this problem different approximations for the exchange-correlation energy are available. The simplest used is the so-called local (spin) density approximation (L(S)DA) which is discussed in the next section.

3.2.4. Local spin density approximation

The electronic structure of a few solids – e.g. alkali metals and the noble metals – can be approximated by the homogeneous electron gas. This led to the idea of approximating the exchange and correlation effects in a solid by using the exchange-correlation energy of the spin-polarized homogeneous electron gas.
The LSDA exchange-correlation functional is defined by the integral over all space of the density times the exchange-correlation energy density of the spin-polarized homogeneous electron gas depending locally on the density:

$$E_{\mathrm{xc}}^{\mathrm{LSDA}}[n,\vec{m}] = \int \mathrm{d}\vec{r} \ n(\vec{r})\epsilon_{\mathrm{xc}}^{\mathrm{HEG}}(n(\vec{r}),\vec{m}(\vec{r})) \quad . \tag{3.24}$$

Thus the only problem in this approximation is finding a proper function for $\epsilon_{\mathrm{xc}}^{\mathrm{HEG}}$. It turns out that even for this simple system it is not possible to calculate $\epsilon_{\mathrm{xc}}^{\mathrm{HEG}}$ analytically. Therefore one usually relies on analytic functions fitted to data from Monte Carlo simulations of the homogeneous electron gas. In this work we use the analytic form of Vosko-Wilk-Nusair (VWN) [25].

There are several other approximations of the exchange-correlation energy, for example the wide field of so-called generalized-gradient approximations, where the gradients of the density are also taken into account by the exchange-correlation functionals.

3.3. Time-dependent density functional theory

The time-dependent DFT (TDDFT) is the extension of ground state DFT to time-dependent external potentials. Instead of solving the time-independent Schrödinger equation the starting point is its time-dependent analogon.

In the following, we will first discuss the Runge-Gross theorem, which is the time-dependent extension of the Hohenberg-Kohn theorem. Then the Kohn-Sham equations for time-dependent potentials are presented. Afterwards, we discuss important approximations to the time-dependent DFT yielding the linear response and the adiabatic approximation.

For the reason of simplicity, we restrict ourselves on the discussion of the non-magnetic case. The extension to the magnetic case is done in a later chapter, when we combine the Green function formalism and the linear response theory.

The following sections are based on the book of Marques *et al.* [26].

3.3.1. Runge-Gross theorem

The Runge-Gross theorem [27] states that

- two densities $n^{(1)}(\vec{r},t)$ and $n^{(2)}(\vec{r},t)$ evolving from a common initial state $\Psi(\vec{r_1}...\vec{r_N},t_0)$ under the influence of two potentials $v^{(1)}(\vec{r},t)$ and $v^{(2)}(\vec{r},t)$, both Taylor-expandable about the initial time t_0, eventually differ if the potentials differ by more than a purely time-dependent function, i.e. $v^{(1)}(\vec{r},t) - v^{(2)}(\vec{r},t) \neq c(t)$.

As the Hohenberg-Kohn theorem, the Runge-Gross theorem predicts a one-to-one correspondence of the potential and the density. However, there are some crucial differences.

Mathematically for the time-dependent calculation one needs to solve the Schrödinger equation which is a first order differential equation in time yielding a dependence on the initial state of the system $\Psi(\vec{r_1}...\vec{r_N},t_0)$. This means, that also the time-dependent density depends on the initial state.

Furthermore, the energy $E[\Psi] = \langle\Psi|\mathcal{H}|\Psi\rangle$ is not conserved in the time-dependent case, such that a minimization of this quantity is useless.

3.3.2. Time-dependent Kohn-Sham equations

The Runge-Gross theorem states that every observable can be calculated with the knowledge of the density $n(\vec{r},t)$ and the initial state $\Psi(\vec{r_1}...\vec{r_N},t_0)$, but it does not say anything on how to calculate the density.

As for the time-independent case a fictitious system – the Kohn-Sham system – of non-interacting particles in an external time-dependent potential $v^{\mathrm{KS}}(\vec{r},t)$ having the same density as the interacting system can be used.

$$i\frac{\partial}{\partial t}\phi_j(\vec{r},t) = \left[-\nabla^2 + v_{KS}(\vec{r},t)\right]\phi_j(\vec{r},t) \quad , \tag{3.25}$$

$$n(\vec{r},t) = \sum_{j=1}^{N} |\phi_j(\vec{r},t)|^2 \quad . \tag{3.26}$$

The Kohn-Sham potential is given in terms of the exchange correlation functional

$$v^{\mathrm{KS}}(\vec{r},t) = v^{\mathrm{ext}}(\vec{r},t) + v^{\mathrm{Hartree}}(\vec{r},t) + v^{\mathrm{xc}}(\vec{r},t) \quad , \tag{3.27}$$

where $v^{\mathrm{xc}}(\vec{r},t)$ is defined such that the density of the Kohn-Sham system equals the density of the interacting system for every time. Compared to the time-independent case the exchange correlation potential in general depends on the entire history of the density $n(\vec{r},t)$, the initial interacting wave function $\Psi(\vec{r_1},...,\vec{r_N},t_0)$ and the initial Kohn-Sham wavefunctions $\phi_i(\vec{r})$. For the special case that the interacting and non-interacting wavefunctions are the non-degenerated ground states the exchange correlation potential depends only on the density but still on its entire history.

Thus solving the time-dependent Kohn-Sham equations is a challenging task. To overcome the complicated dependences of the exchange correlation potential different approximations can be done. In this work the so-called adiabatic approximation discussed in the next section is used.

3.3.3. Adiabatic approximation

In the adiabatic approximation the exchange correlation functional is approximated by its static analogue being evaluated at the time-dependent density:

$$v_{\mathrm{xc}}^{\mathrm{adiabatic}}(\vec{r},t) = v_{xc}^{\mathrm{static}}[n](\vec{r})\big|_{n=n(t)} \quad . \tag{3.28}$$

In this way, the entire history dependence is neglected.

Since the static exchange correlation potential is a ground state property, we expect this approximation to work for systems close to the equilibrium. The most commonly used adiabatic approximation is the so called adiabatic local density approximation (ALDA) which uses the exchange correlation potential of the homogeneous electron gas

$$v_{\mathrm{xc}}^{\mathrm{ALDA}}(\vec{r},t) = v_{\mathrm{xc}}^{\mathrm{HEG}}(n)\big|_{n=n(\vec{r},t)} \quad . \tag{3.29}$$

3.3.4. Linear response of the charge density

A different approximation to the time-dependent DFT can be done for small external time-dependent potentials. In this case, it is often not necessary to solve the full Kohn-Sham equations. Instead one can make use of the linear response theory.

Assume a system being in the ground state for $t < t_0$ with the ground state density $n_0(\vec{r})$. For small perturbations in the external potential, the density can be expanded up to first order in the potential:

$$v^{\mathrm{ext}}(\vec{r},t) = v_0(\vec{r}) + \delta v(\vec{r},t) \tag{3.30}$$

$$\Rightarrow \qquad n(\vec{r},t) = n_0(\vec{r}) + \delta n(\vec{r},t) + \mathcal{O}\left((\delta v)^2\right) \quad . \tag{3.31}$$

Using a Fourier transformation the change in the density can be written in terms of a susceptibility χ in the frequency space as

$$\delta n(\vec{r},\omega) = \int \mathrm{d}\vec{r}'\ \chi(\vec{r},\vec{r}',\omega)\delta v(\vec{r}',\omega) \quad . \tag{3.32}$$

The concept of susceptibilities or in more general response functions will be discussed in more detail in chapter 6. At the moment, we can view eq. (3.32) as the definition of χ.

The main property of the Kohn-Sham system is the equality of the Kohn-Sham density to the density of the interacting system, such that

$$\delta n(\vec{r},\omega) = \int \mathrm{d}\vec{r}'\ \chi_{\mathrm{KS}}(\vec{r},\vec{r}',\omega)\delta v_{\mathrm{KS}}(\vec{r}',\omega) \quad , \tag{3.33}$$

where χ_{KS} is the susceptibility of the Kohn-Sham system and δv_{KS} is the Kohn-Sham potential up to first order in the perturbing potential,

$$\delta v_{\mathrm{KS}}(\vec{r},\omega) = \delta v(\vec{r},\omega) + \delta v_{\mathrm{Hartree}}(\vec{r},\omega) + \delta v_{\mathrm{xc}}(\vec{r},\omega) \quad , \tag{3.34}$$

with the Hartree potential

$$\delta v_{\mathrm{Hartree}}(\vec{r},\omega) = \int \mathrm{d}\vec{r}'\ \underbrace{\frac{2}{|\vec{r}-\vec{r}'|}}_{f_{\mathrm{Hartree}}(\vec{r},\vec{r}')}\ \delta n(\vec{r}',\omega) \quad , \tag{3.35}$$

and the exchange correlation potential

$$\delta v_{\mathrm{xc}}(\vec{r},\omega) = \int \mathrm{d}\vec{r}'\ \underbrace{\frac{\delta v_{xc}(\vec{r},\omega)}{\delta n(\vec{r}',\omega)}}_{=f_{xc}(\vec{r},\vec{r}';\omega)}\ \delta n(\vec{r}',\omega) \quad . \tag{3.36}$$

where we have defined the so-called kernels f_{Hartree} and f_{xc} which are the functional derivatives of the potentials evaluated at the ground state density.
Plugging this expressions into eq. (3.33) yields

$$\begin{aligned}\delta n(\vec{r},\omega) =& \int \mathrm{d}\vec{r}'\chi_{KS}(\vec{r},\vec{r}',\omega)\delta v(\vec{r}',\omega)\\ &+ \int \mathrm{d}\vec{r}' \int \mathrm{d}\vec{r}''\chi_{KS}(\vec{r},\vec{r}'',\omega)\left[f_{\mathrm{Hartree}}(\vec{r}'',\vec{r}') + f_{\mathrm{xc}}(\vec{r}'',\vec{r}',\omega)\right]\delta n(\vec{r}',\omega) \quad ,\end{aligned} \tag{3.37}$$

which finally yields an expression for the susceptibility of the interacting system

$$\begin{aligned}\chi(\vec{r},\vec{r}',\omega) =&\chi_{KS}(\vec{r},\vec{r}',\omega)\\ &+ \int \mathrm{d}\vec{x} \int \mathrm{d}\vec{x}'\chi_{KS}(\vec{r},\vec{x},\omega)\left[f_{\mathrm{Hartree}}(\vec{x},\vec{x}') + f_{\mathrm{xc}}(\vec{x},\vec{x}',\omega)\right]\chi(\vec{x}',\vec{r}',\omega) \quad ,\end{aligned} \tag{3.38}$$

which is a Dyson-like equation and has to be solved self-consistently.
Since the unperturbed system is in the ground state, the Kohn-Sham susceptibility can be written in terms of the ground state Kohn-Sham orbitals. Furthermore, the Hartree kernel is universal, not depending on the density. The only time-dependent quantity is the exchange-correlation kernel. It depends crucially on the approximations made within the TDDFT scheme. In this work we always stick to the adiabatic local density approximation which simplifies the calculation of the exchange correlation kernel, since it neglects the time/frequency dependence of the kernel.

3.4. Currents within density functional theory

In this section currents within density functional theory are discussed. In the first part, the usage of charge currents to construct current-depended energy functionals, which leads to the so-called current density functional theory (CDFT), is shown. In the second part, the difference between spin currents in the Kohn-Sham system and spin currents in the interacting system is enlightened.

3.4.1. Current density functional theory

In most of the widely used density functional theory implementations the magnetic field is considered to only couple to the spin degree of freedom, which induces a spin moment. However, a magnetic field can also influence the orbital motion of the electrons, which induces currents. The vector potential $\vec{A}$, which is connected to the magnetic field via Maxwell's equations, couples to the motion of the electrons as can be seen in the kinetic energy part of the Hamiltonian:

$$\mathcal{H}_{\text{kin}} = \frac{1}{2m}\left(\vec{p} - e\vec{A}\right)^2 \quad . \tag{3.39}$$

Evaluating the kinetic energy yields

$$\begin{aligned} E_{\text{kin}} &= \left\langle \psi \middle| \frac{1}{2m}\left(\vec{p} - e\vec{A}\right)^2 \middle| \psi \right\rangle & (3.40) \\ &= T[n] + \int \mathrm{d}\vec{r}\ \vec{j}_{\text{para}}(\vec{r}) \cdot \vec{A}(\vec{r}) + \int \mathrm{d}\vec{r}\ \frac{e^2}{2m}\vec{A}(\vec{r})^2 n(\vec{r}) \quad , & (3.41) \end{aligned}$$

where $T[n]$ is the kinetic energy without external field and we restricted ourselves to the case of a spin-less particle. Equation (3.41) shows explicitly the coupling of the vector potential $\vec{A}$ to the paramagnetic charge current density $\vec{j}_{\text{para}}$.

Vignale and Rasolt [28**?**] developed an extension of the density functional theory using the vector potential as an additional potential, which couples to the charge current density. Thus, in addition to the charge density n, the energy functional used in the DFT scheme depends on the paramagnetic charge current density $\vec{j}_{\text{para}}$:

$$E = E[n, \vec{j}_{\text{para}}]. \tag{3.42}$$

It is possible to prove a Hohenberg-Kohn theorem, which consists of two parts: On the one hand it states that there is a one-to-one correspondence between the set of densities $\{n, \vec{j}_{\text{para}}\}$ and the set of the potentials $\{v, \vec{A}\}$. On the other hand it states that in the ground state the energy with respect to the four densities is minimized.

Furthermore, there is a Kohn-Sham system having the same densities as the interacting system, which is achieved by using the exchange-correlation energy

$$E_{\text{xc}}[n, \vec{j}_{\text{para}}], \tag{3.43}$$

which depends on all the densities. Therefore, in addition to the exchange-correlation scalar potential, the exchange-correlation vector potential, which is the functional derivative of the exchange-correlation energy with respect to the paramagnetic charge current density, has to be introduced. The described procedure is known as the current density functional theory (CDFT). The main strength of the scheme is its ability of describing arbitrary strong magnetic fields. In principle, for a precise description of any system with an applied (time-dependent) magnetic field CDFT has to be used, but even systems without external magnetic field can have finite paramagnetic currents so that CDFT could be useful. However, as always when it comes to DFT a lot of approximations are involved and one has to decide if it is worth the effort.

In the first part of this work, we deal with ground state phenomena without applied external magnetic fields. One of the main quantities discussed in our results is the orbital magnetic moment caused by the orbital motion of the electrons. Ebert *et al.* [29] analyzed the orbital magnetic moment within the CDFT scheme for different magnetic bulk systems. The main outcome is that the CDFT scheme improves the values of the orbital magnetic moment compared to the experimental values by a few percent. However, the effect of CDFT is small compared to other approximations. For example they showed that the so-called extended orbital-polarization formalism improves the orbital magnetic moments much more than the CDFT scheme does.

3.4.2. Kohn-Sham spin current

In the standard DFT scheme two fundamental quantities are used – namely the charge and the spin density – which are the same in the Kohn-Sham and the interacting system. However, the charge current and the spin current are not fundamental quantities, so that the Kohn-Sham currents can differ from their interacting counterpart, which was first shown by Capelle *et al.* [30].

As pointed out in section 2 the appropriate way of defining currents is via a continuity equation. The charge continuity equation of the Kohn-Sham system follows directly from the single particle description in section 2.3.1. For the interacting system in addition there is the electron-electron interaction, but it does not contribute to the continuity equation, so that in total the charge continuity equations in the non-relativistic limit are given by:

$$\frac{\partial \rho}{\partial t} + \vec{\nabla} \cdot \vec{j}_{\mathrm{KS}} = 0 \quad \text{and} \quad \frac{\partial \rho}{\partial t} + \vec{\nabla} \cdot \vec{j} = 0 \quad . \tag{3.44}$$

In total, the divergence of the charge currents must be the same in both systems:

$$\Rightarrow \qquad \vec{\nabla} \cdot \vec{j} = \vec{\nabla} \cdot \vec{j}_{\mathrm{KS}} \quad . \tag{3.45}$$

In case of the spin-current the situation is a bit different, since there is in addition the spin torque. The spin continuity equation of the Kohn-Sham system using the corresponding Kohn-Sham Hamiltonian gives access to the Kohn-Sham spin current:

$$\frac{\partial m^a}{\partial t} + \vec{\nabla} \cdot \vec{j}^{\,a}_{\mathrm{KS}} = 2\left(\vec{B}_{\mathrm{KS}} \times \vec{m}\right)^a \quad , \tag{3.46}$$

where $\vec{B}_{\mathrm{KS}} = \mu_B \vec{B}_{\mathrm{ext}} + \vec{B}_{\mathrm{xc}}$ is the Kohn-Sham magnetic field. For the interacting system the electron-electron interaction does not contribute, so that the continuity equation is given by

$$\frac{\partial m^a}{\partial t} + \vec{\nabla} \cdot \vec{j}^{\,a} = 2\mu_B \left(\vec{B}_{\mathrm{ext}} \times \vec{m}\right)^a \quad , \tag{3.47}$$

which yields an equation connecting the difference of the Kohn-Sham spin-current and the interacting spin-current to the exchange correlation magnetic field:

$$2\left(\vec{B}_{\mathrm{xc}} \times \vec{m}\right)^a = \vec{\nabla} \cdot \left[\vec{j}^{\,a}_{\mathrm{KS}} - \vec{j}^{\,a}\right] = \vec{\nabla} \cdot \vec{j}^{\,a}_{\mathrm{xc}} \quad , \tag{3.48}$$

where we defined the difference of the Kohn-Sham spin-current and the interacting spin-current as j^a_{xc}. By integrating over the whole space and using Gauss' theorem one arrives at

$$\int \mathrm{d}\vec{r}\; \vec{B}_{\mathrm{xc}} \times \vec{m} = 0 \quad , \tag{3.49}$$

the so-called zero-torque theorem, which can be interpreted as follows: The exchange-correlation magnetic field does not exert any torque on the Kohn-Sham system as a whole.

The zero-torque theorem is a very important theorem, which has to be fulfilled for any approximation of the exchange-correlation magnetic field. In this work, we are using the LSDA as an approximation of the exchange-correlation energy. In the (adiabatic) LSDA the exchange-correlation magnetic field is by definition parallel to the magnetization yielding

$$\vec{B}_{\mathrm{xc}}(\vec{r},t) \parallel \vec{m}(\vec{r},t) \quad \Rightarrow \quad \vec{B}_{\mathrm{xc}}(\vec{r},t) \times \vec{m}(\vec{r},t) \quad . \tag{3.50}$$

Thus the zero-torque theorem is trivially fulfilled by the LSDA. Furthermore, the spin-currents of the Kohn-Sham system should then equal the ones of the interacting system.

4. Korringa-Kohn-Rostoker Green function method

In the previous chapter we discussed the general DFT scheme. We saw that for the calculation of the electronic structure one has to solve the Kohn-Sham equations, but we have not shown how to solve these equations. There are several different approaches, which all have their own specific advantages, e.g. for periodic systems one often uses plane wave methods and works in the reciprocal space.
However, in this work we will mainly discuss small nanostructures deposited on surfaces. Usual plane wave methods need large supercells to minimize interaction effects between the periodic replicas of the nanostructure. Therefore, we use the Korringa-Kohn-Rostoker (KKR) Green function method, which was originally developed by Korringa [31], Kohn and Rostoker [32] for the calculation of periodic solids, but can be utilized within a real space approach being perfectly suited to describe nanostructures on surfaces.
In the following chapter, we discuss the different concepts used in the KKR method. The idea is to slowly build up the KKR formalism. We start with the description of the Green function formalism. Subsequent, the KKR formalism for collinear structures without spin-orbit coupling is discussed. Afterwards, we extend this scheme to non-collinear structures with spin-orbit coupling. We end this chapter with a discussion of currents within the KKR scheme.
The main ideas of this chapter are well described in the book of Zabloudil [33] and the review of Mavropoulos and Papanikolaou [34].

4.1. Green function formalism

The time-dependent Green function of a single particle Hamiltonian is defined via

$$(i\partial_t - \mathcal{H}(\vec{r}))\, G^{R/A}(\vec{r},\vec{r}\,';t,t') = \delta(t-t')\delta(\vec{r}-\vec{r}\,') \quad , \tag{4.1}$$

where $G^{R/A}$ are the retarted respectively advanced Green functions fulfilling the boundary conditions

$$G^{R}(\vec{r},\vec{r}\,';t,t') = 0 \qquad \text{for } t < t' \tag{4.2}$$

$$G^{A}(\vec{r},\vec{r}\,';t,t') = 0 \qquad \text{for } t > t' \quad . \tag{4.3}$$

For time-independent Hamiltonians, which we are considering here, one can show that the Green functions have only one time argument depending on the time difference $t-t'$.
Furthermore, in this case it is convenient to solve the static Schrödinger equation. The Fourier transform of eq. (4.1) is given by

$$(E \pm i\eta - \mathcal{H}(\vec{r}))\, G(\vec{r},\vec{r}\,';E \pm i\eta) = \delta(\vec{r}-\vec{r}\,') \quad , \tag{4.4}$$

where we defined the Fourier transform of the Green function as

$$G(E \pm i\eta) = \int \mathrm{d}t \; e^{i(E \pm i\eta)t} G^{R/A}(t) \quad , \tag{4.5}$$

and added a small parameter $\eta \to 0^+$ ensuring convergence of the integral at $t \to \pm\infty$. The formal solution of the Green function is given by

$$G(\vec{r}, \vec{r}\,'; E + i\eta) = (E + i\eta - \mathcal{H})^{-1} \, \delta(\vec{r} - \vec{r}\,') \quad . \tag{4.6}$$

Using the eigenfunctions of the Hamiltonian being two component spinors, which form a complete basis set the Green function can be written as

$$G(\vec{r}, \vec{r}\,'; E + i\eta) = \sum_n \frac{\Psi_n(\vec{r})\Psi_n^\dagger(\vec{r}\,')}{E - E_n + i\eta} = \begin{pmatrix} G^{\uparrow\uparrow} & G^{\uparrow\downarrow} \\ G^{\downarrow\uparrow} & G^{\downarrow\downarrow} \end{pmatrix} \quad , \tag{4.7}$$

or equivalently written in operator form

$$G(E + i\eta) = \sum_n \frac{|n\rangle\langle n|}{E - E_n + i\eta} \quad . \tag{4.8}$$

The Green functions are very useful to describe perturbed systems.
Consider an external perturbation ΔV. Let G_0 be the Green function of the unperturbed Hamiltonian $\mathcal{H}_0$ with the wavefunction Ψ_0. One can easily show that the perturbed wavefunction is given by [35]

$$\Psi(\vec{r}, E) = \Psi_0(\vec{r}, E) + \int \mathrm{d}\vec{r}\,' \; G_0(\vec{r}, \vec{r}\,'; E)\Delta V(\vec{r}\,')\Psi(\vec{r}\,', E) \quad , \tag{4.9}$$

which is the so called Lippmann-Schwinger equation.
From the definition of the Green function directly follows a Dyson integral equation for the perturbed Green function:

$$G(\vec{r}, \vec{r}\,'; E) = G_0(\vec{r}, \vec{r}\,'; E) + \int \mathrm{d}\vec{r}\,'' \; G_0(\vec{r}, \vec{r}\,''; E)\Delta V(\vec{r}\,'')G(\vec{r}\,'', \vec{r}\,'; E) \quad . \tag{4.10}$$

To simplify the notation we will often skip the integrals and arguments in those expressions yielding

$$G = G_0 + G_0 \Delta V G \tag{4.11}$$

$$= G_0 + G_0 \Delta V G_0 + G_0 \Delta V G_0 \Delta V G_0 + \ldots \tag{4.12}$$

There are two ways of solving the Dyson equation. Either one inverts eq. (4.11) yielding

$$G = (1 - G_0 \Delta V)^{-1} G_0 \quad , \tag{4.13}$$

or one calculates the Green function iteratively cutting eq. (4.12) after a finite summation.
The simplest non-trivial approximation is given by the so called first-order Born approximation

$$G = G_0 + G_0 \Delta V G_0. \tag{4.14}$$

Often the so-called transition matrix ($\mathcal{T}$-matrix) which relates the perturbed to the unperturbed Green function is used:

$$G = G_0 + G_0 \mathcal{T} G_0 \tag{4.15}$$

$$\text{with} \qquad \mathcal{T} = \Delta V + \Delta V G_0 \Delta V + \ldots \tag{4.16}$$

Thus instead of solving the Dyson equation for the Green function one has to solve a Dyson equation for the $\mathcal{T}$-matrix.

The most important use of the Green function is its connection to the statistical average of an observable $\hat{A}$ in a fermionic system,

$$\langle \hat{A} \rangle = \sum_n f(E_n)\ \langle n|\hat{A}|n\rangle \quad , \tag{4.17}$$

where $f(E)$ is the Fermi-Dirac distribution,

$$f(E) = \frac{1}{e^{\beta(E-\mu)}+1} \quad , \tag{4.18}$$

with $\beta = 1/k_BT$, k_B the Boltzmann constant, T the temperature of the system and μ the chemical potential, which equals the Fermi energy at zero temperature.
Applying the Dirac identity to eq.(4.8) and multiplying with the Fermi-Dirac distribution $f(E)$, the energy-integrated Green function can be written as

$$\int \mathrm{d}E\ f(E)\ G(E \pm i\eta) = \mathcal{P}\left[\int \mathrm{d}E\ f(E) \sum_n \frac{|n\rangle\langle n|}{E-E_n}\right] \mp i\pi \sum_n f(E_n)\ |n\rangle\langle n| \quad , \tag{4.19}$$

where $\mathcal{P}$ means Cauchy principal value.
Comparing to the statistical average of the observable A yields

$$\langle \hat{A} \rangle = -\frac{1}{\pi}\mathrm{Im}\int \mathrm{d}E\ f(E)\ \mathrm{Tr}\ \left[\hat{A}\ G(E+i\eta)\right] \quad , \tag{4.20}$$

with the imaginary part of the Green function being defined via

$$\mathrm{Im}\ G(E+i\eta) = \frac{1}{2i}\left[G(E+i\eta) - G(E-i\eta)\right] \quad . \tag{4.21}$$

Therefore, the Green function contains the same physical information as the wavefunction. Knowing the Green function is sufficient to calculate any physical property of a system.

Having the DFT scheme in mind, we need two very important quantities – the density and the magnetization density – which can be calculated using Green functions. In the zero temperature limit where $f(E) = \Theta(T - E_F)$ they are given by

$$n(\vec{r}) = -\frac{1}{\pi}\int^{E_F} \mathrm{d}E\ \mathrm{Im}\ \mathrm{Tr}\ G(\vec{r},\vec{r};E+i\eta) \quad , \quad \text{and} \tag{4.22}$$

$$\vec{m}(\vec{r}) = -\frac{\mu_B}{\pi}\int^{E_F} \mathrm{d}E\ \mathrm{Im}\ \mathrm{Tr}\ \vec{\boldsymbol{\sigma}} G(\vec{r},\vec{r};E+i\eta) \quad . \tag{4.23}$$

Furthermore, the energy-resolved density of states is an important quantity

$$n(E) = -\frac{1}{\pi}\int_{\mathcal{V}} \mathrm{d}\vec{r}\ \mathrm{Im}\ \mathrm{Tr}\ G(\vec{r},\vec{r};E+i\eta) \tag{4.24}$$

$$= -\frac{1}{\pi}\int_{\mathcal{V}} \mathrm{d}\vec{r}\ \mathrm{Im}\left[G^{\uparrow\uparrow}(\vec{r},\vec{r};E+i\eta) + G^{\downarrow\downarrow}(\vec{r},\vec{r};E+i\eta)\right] \quad , \tag{4.25}$$

where $\mathcal{V}$ is the unit cell volume.

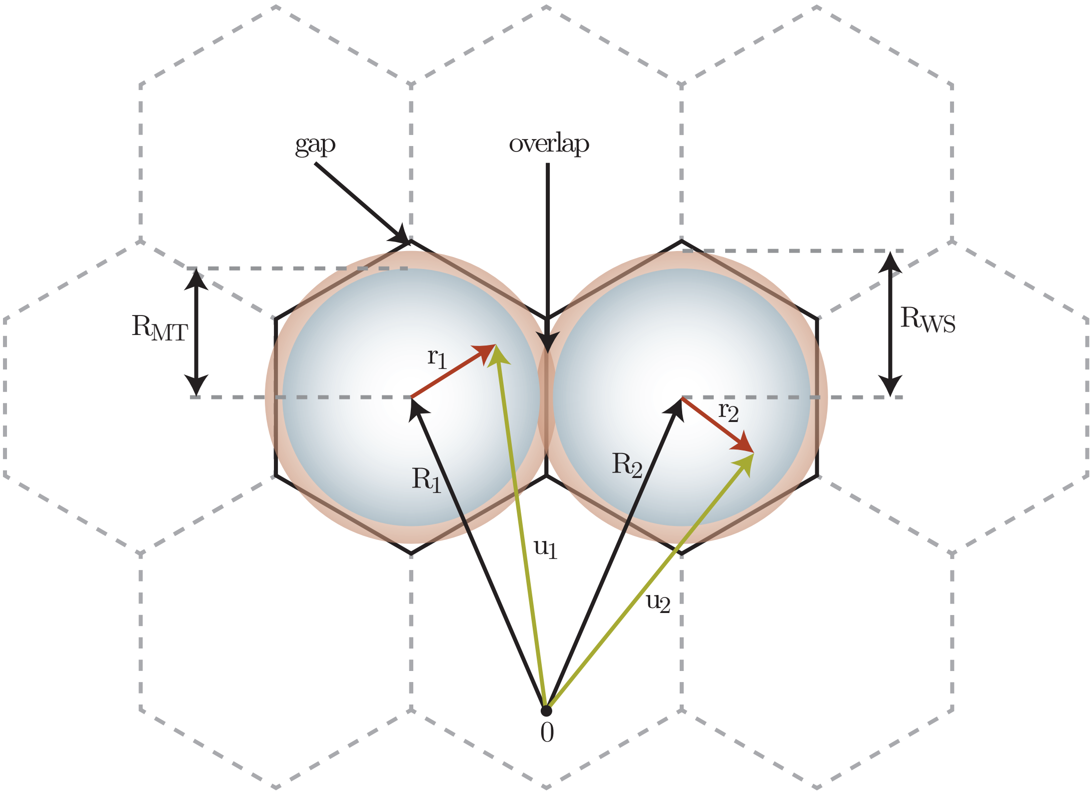

Figure 4.1.: Voronoi construction: The Voronoi cells contain all points being closest to the corresponding lattice point. In the ASA the Voronoi cells are replaced by Wigner-Seitz spheres, which have the same volume as the Voronoi cells yielding gaps and overlaps.

4.2. KKR Green function in the atomic sphere approximation

The KKR method is a real space method using Green functions to solve the Schrödinger equation. The space consisting of atoms is divided by a so called Voronoi construction into cells containing all points being closest to the center which is usually the atom site (see fig. 4.1).
At each site relative coordinates are used, such that a point $\vec{u}$ at cell i is described by the position relative to the center of the cell $\vec{r}$ and the position of the center $\vec{R}_i$:

$$\vec{u} = \vec{r} + \vec{R}_i \quad , \tag{4.26}$$

Often, the atomic potential can be sufficiently approximated by a spherically symmetric potential given by

$$V(\vec{r}) = V(r) = \begin{cases} V(r) & \text{for } r < R_{\mathrm{MT}} \\ 0 & \text{else.} \end{cases} , \quad \text{with} \quad V(r) = \begin{pmatrix} V^{\uparrow\uparrow} & V^{\uparrow\downarrow} \\ V^{\downarrow\uparrow} & V^{\downarrow\downarrow} \end{pmatrix} \quad , \tag{4.27}$$

where R_{MT} is the muffin-tin radius shown in fig. 4.1.
However, the volume of the spheres with radius R_{MT} does not match the volume of the Voronoi cells. Therefore, in the atomic sphere approximation (ASA) spherical symmetric cells with the Wigner-Seitz radius R_{WS} are constructed having the same volume as the Voronoi cell. One drawback of

this approximation is that the constructed spheres overlap, which will become obvious when we discuss the results of this work.
To summarize, the problem which should be solved by the KKR formalism is the single particle Schrödinger equation with a periodic spherical symmetric potential using a Green function:

$$(E + \vec{\nabla}^2 - V^n(r))G(\vec{r} + \vec{R}_n, \vec{r}' + \vec{R}_{n'}; E) = \delta_{nn'}\delta(\vec{r} - \vec{r}') \quad , \tag{4.28}$$

where V^n is the potential at site n.
For this, the KKR formalism makes use of scattering theory, which yields a Green function of the form

$$G(\vec{r} + \vec{R}_n, \vec{r}' + \vec{R}_{n'}; E) = G_n^{\text{on-site}}(\vec{r}, \vec{r}'; E)\delta_{nn'} + G_{nn'}^{\text{str}}(\vec{r}, \vec{r}'; E) \quad , \tag{4.29}$$

where $G_n^{\text{on-site}}$ is the on-site solution and $G_{nn'}^{\text{str}}$ is the so called structural Green function accounting for multiple scattering and the geometrical details of the system.
We start our discussion within the framework of collinear magnetism, such that the potential can be considered as diagonal in spin space

$$V(r) = \begin{pmatrix} V^{\uparrow\uparrow} & V^{\uparrow\downarrow} \\ V^{\downarrow\uparrow} & V^{\downarrow\downarrow} \end{pmatrix} = \begin{pmatrix} V^{\uparrow} & 0 \\ 0 & V^{\downarrow} \end{pmatrix} \tag{4.30}$$

yielding two decoupled equations for the Green function of the two different spin configurations.
In the next section we introduce single-site scattering.

4.2.1. Single-site scattering

To describe single-site scattering we consider a scattering center at $\vec{0}$ given by a finite spherically symmetric potential

$$V(r) = \begin{cases} V(r) & \text{for } r < R_{\text{WS}} \\ 0 & \text{otherwise.} \end{cases} \tag{4.31}$$

For the reason of simplicity, we drop the spin index, since all spin dependent equations are decoupled.
The spherical symmetry of the problem is an excellent condition for an expansions of all space dependent quantities in terms of spherical harmonics. Every function $A(\vec{r})$ can be written as

$$A(\vec{r}) = \sum_L A_L(r)Y_L(\hat{r}) \quad , \tag{4.32}$$

where $L = (l, m)$ is a combined index of the angular momentum indices and Y_L are real spherical harmonics. In this way the time-independent Schrödinger equation for a single particle in an external radial non-magnetic potential can be simplified to a radial differential equation,

$$\left(-\frac{1}{r^2}\partial_r\left(r^2\partial_r\right) + \frac{l(l+1)}{r^2} + V(r) - E\right)R_l(r; E) = 0 \quad , \tag{4.33}$$

where $R_l(r; E)$ is the radial part of the wavefunction.
To solve the radial Schrödinger equation we can make use of the Lippmann-Schwinger equation (eq. (4.9)). Therefore, we need an unperturbed reference system which is the free electron gas. The solutions of the Schrödinger equation are plane waves with $|\vec{k}| = \sqrt{E}$

$$\psi_{\vec{k}}(\vec{r}) = e^{i\vec{k}\cdot\vec{r}} = \sum_L 4\pi i^l j_l(\sqrt{E}r)Y_L(\hat{r})Y_L(\hat{k}) \quad , \tag{4.34}$$

where j_l is the spherical Bessel function. From the wavefunctions one can construct the Green function of the free electron gas

$$g(\vec{r}, \vec{r}'; E) = -\frac{1}{4\pi} \frac{e^{i\sqrt{E}|\vec{r}-\vec{r}'|}}{|\vec{r} - \vec{r}'|} \quad , \tag{4.35}$$

which can be rewritten in terms of real spherical harmonics

$$g(\vec{r}, \vec{r}'; E) = \sum_L Y_L(\hat{r}) g_l(r, r'; E) Y_L(\hat{r}') \quad , \tag{4.36}$$

with

$$g_l(r, r'; E) = -i\sqrt{E} j_l(\sqrt{E} r_<) h_l(\sqrt{E} r_>) \quad , \tag{4.37}$$

where we used the spherical Hankel functions $h_l = j_l + i n_l$ with the spherical Neumann functions n_l and $r_{>/<}$ is the bigger/smaller of the radii r and r'. The Bessel function is well behaving at $r \to 0$, whereas the Neumann and Hankel functions are diverging at $r \to 0$. Both, the Bessel and the Hankel function, are solutions of the free Schrödinger equation.

The Lippmann-Schwinger equation (4.9) combined with the expanded form of the free Green function eq. (4.36) yields a regular solution converging at $r \to 0$ constructed from the Bessel function

$$R_l(r; E) = j_l(\sqrt{E} r) + \int_0^{R_{\mathrm{WS}}} \mathrm{d}r'\ r'^2 g_l(r, r'; E) V(r') R_l(r'; E) \quad , \tag{4.38}$$

and an irregular solution diverging at $r \to 0$ constructed from the Hankel functions

$$H_l(r; E) = h_l(\sqrt{E} r) \beta_l + \int_0^{R_{\mathrm{WS}}} \mathrm{d}r'\ r'^2 g_l(r, r'; E) V(r') H_l(r'; E) \quad , \tag{4.39}$$

where β_l is a factor fulfilling boundary conditions [36].

For $r > R_{\mathrm{MT}}$ these expressions can be further simplified

$$R_l(r; E) = j_l(\sqrt{E} r) - i h_l(\sqrt{E} r) \sqrt{E} \underbrace{\int_0^{R_{\mathrm{WS}}} \mathrm{d}r'\ r'^2 j_l(\sqrt{E} r') V(r') R_l(r'; E)}_{= t_l(E)} \tag{4.40}$$

$$\text{and} \qquad H_l(r; E) = h_l(\sqrt{E} r) \quad , \tag{4.41}$$

where we defined the t-matrix in the angular momentum representation $t_l(E)$. At this point we can give an interpretation of the regular and irregular solutions. The regular solution R_l can be viewed as a wave described by the potential-free solution j_l being scattered at the scattering center, which is described the the t-matrix. However, the irregular solution H_l is a wave, which is not scattered outside the potential region, but is affected inside the scattering potential.

It can be shown that the Green function of the scattering problem can be written in terms of the regular and the irregular solutions [34]:

$$G(\vec{r}, \vec{r}'; E) = - i\sqrt{E} \sum_L R_l(r_<; E) H_l(r_>; E) Y_L(\hat{r}) Y_L(\hat{r}') \tag{4.42}$$

$$= \sum_L Y_L(\hat{r}) G_l(r, r'; E) Y_L(\hat{r}') \quad , \tag{4.43}$$

Thus we solved the scattering problem for a single spherical symmetric potential. In the KKR formalism we deal with multiple sites indeed. In the next section we show how to extend the theory to arrive at the full KKR representation of the Green function.

4.2.2. Structural Green function

For the full Green function in the KKR formalism we need to add all the different scattering centres in the Voronoi cells to our theory. Starting from the reference system of free electrons the Green function for different sites n and n' is given by

$$g(\vec{r}+\vec{R}_n,\vec{r}'+\vec{R}_{n'};E) = -\frac{1}{4\pi}\frac{e^{i\sqrt{E}\,|\vec{r}+\vec{R}_n-\vec{r}'-\vec{R}_{n'}|}}{|\vec{r}+\vec{R}_n-\vec{r}'-\vec{R}_{n'}|} \quad , \tag{4.44}$$

which can be written in terms of Hankel and Bessel function as shown in eq. (4.36). Furthermore, we can make use of a theorem for the transformation of Hankel functions:

$$h_L(\vec{r}'+\vec{R}_{n'}-\vec{R}_n;E) = \frac{i}{\sqrt{E}}\sum_{L'} g_{LL'}^{nn'}(E) j_{L'}(\vec{r}';E) \quad \text{for} \quad |\vec{r}-\vec{r}'| < |\vec{R}_n-\vec{R}_{n'}| \quad , \tag{4.45}$$

where we defined $j_L(\vec{r};E) = j_l(\sqrt{E}r)Y_L(\hat{r})$ and $h_L(\vec{r};E) = h_l(\sqrt{E}r)Y_L(\hat{r})$. The expansion coefficient $g_{LL'}^{nn'}(E)$, which are called structure constants being connected to the structural Green function $G_{nn'}^{\mathrm{str}}$, are given by

$$g_{LL'}^{nn'}(E) = -(1-\delta_{nn'})4\pi i\sqrt{E}\sum_{L''} i^{l-l'+l''} C_{LL'}^{L''} h_{L''}(\vec{R}_n-\vec{R}_{n'};E) \quad , \tag{4.46}$$

with the Gaunt coefficient

$$C_{LL'}^{L''} = \int \mathrm{d}\Omega\ Y_L(\hat{r})Y_{L'}(\hat{r})Y_{L''}(\hat{r}) \quad . \tag{4.47}$$

Applying the theorem to the free electron Green function yields

$$g(\vec{r}+\vec{R}_n,\vec{r}'+\vec{R}_{n'};E) = -i\sqrt{E}\sum_L j_L(\vec{r}_<;E)h_L(\vec{r}_>;E)\delta_{nn'} + \sum_{LL'} j_L(\vec{r};E)g_{LL'}^{nn'}(E)j_{L'}(\vec{r}';E) \quad . \tag{4.48}$$

Thus, knowing the Green function of the free electron reference system we can use the Dyson equation (4.10) to calculate the Green function of the perturbed system:

$$\begin{aligned} G(\vec{r}+\vec{R}_n,\vec{r}'+\vec{R}_{n'};E) &= g(\vec{r}+\vec{R}_n,\vec{r}'+\vec{R}_{n'};E) \\ &+ \sum_{n''}\int_{\mathcal{V}_{n''}} \mathrm{d}\vec{r}''\ g(\vec{r}+\vec{R}_n,\vec{r}''+\vec{R}_{n''};E)V^{n''}(r'')G(\vec{r}''+\vec{R}_{n''},\vec{r}'+\vec{R}_{n'};E) \quad . \end{aligned} \tag{4.49}$$

A proper ansatz for the full Green function which describes the single-site scattering as well as the structural scattering is given by

$$\begin{aligned} &G(\vec{r}+\vec{R}_n,\vec{r}'+\vec{R}_{n'};E) = \\ &-i\sqrt{E}\sum_L R_L^n(\vec{r}_<;E)H_L^n(\vec{r}_>;E)\delta_{nn'} + \sum_{LL'} R_L^n(\vec{r};E)G_{LL'}^{nn'}(E)R_{L'}^{n'}(\vec{r}';E) \quad . \end{aligned} \tag{4.50}$$

where $R_L^n(\vec{r}_<;E) = R_l^n(r_<;E)Y_L(\hat{r})$ and $H_L^n(\vec{r}_<;E) = H_l^n(r_<;E)Y_L(\hat{r})$ are the regular, respectively irregular solutions of the Schrödinger equation for the single site problem at site n.
Plugging eqs. (4.48) and (4.50) into eq. (4.49) yields a Dyson equation for the structural Green function coefficients

$$G_{LL'}^{nn'}(E) = g_{LL'}^{nn'}(E) + \sum_{n'',L''} g_{LL''}^{nn''}(E)t_{l''}^{n''}(E)G_{L''L'}^{n''n'}(E) \quad , \tag{4.51}$$

with the t-matrix defined in eq. (4.40). The structural Green function coefficients contain informations about the geometrical arrangement of the atoms and the multiple scattering.

4.3. Projection scheme of the KKR Green function

In the previous section we showed that the standard KKR representation of the Green function in the ASA is given by

$$G(\vec{r}+\vec{R}_n,\vec{r}\,'+\vec{R}_{n'};E)=\sum_{LL'}Y_L(\hat{r})G^{nn'}_{LL'}(r,r';E)Y_{L'}(\hat{r}') \quad , \tag{4.52}$$

with

$$\begin{aligned} G^{nn'}_{LL'}(r,r';E)=&-i\sqrt{E}R^n_l(r_<;E)H^n_l(r_>;E)\delta_{nn'}\delta_{LL'} \\ &+R^n_l(r;E)G^{nn'}_{LL'}(E)R^{n'}_{l'}(r';E) \quad . \end{aligned} \tag{4.53}$$

The matrix element $G^{nn'}_{LL'}(r,r';E)$ is constructed from several energy-dependent functions: the regular and irregular radial basis functions, R^n_l and H^n_L, and the structural Green function $G^{nn'}_{LL'}$. In this work we use an projection scheme described in the appendix of the paper of dos Santos Dias et al.[37], which maps the large set of matrix elements $G^{nn'}_{LL'}(r,r';E)$ on a smaller set of energy independent radial basis functions $\phi_{nlb}(r)$ with $b=\{1,2,\ldots\}$ and an energy dependent Green function matrix element such that

$$G(\vec{r}+\vec{R}_n,\vec{r}\,'+\vec{R}_{n'};E)=\sum_{\substack{LL'\\bb'}}Y_L(\hat{r})\phi_{nlb}(r)G_{nLb;n'L'b'}(E)\phi_{n'l'b'}(r')Y_{L'}(\hat{r}') \quad . \tag{4.54}$$

The projection of course decreases the accuracy, but it also yields a large speed-up of the calculations, especially for the computationally demanding linear response calculations in the second part of this work. A detailed comparison of the density of states for the projected Green function and the standard representation, showing the capability of this projection scheme, can be found in the work of Schweflinghaus [38].

To construct the new basis, we start with radial basis functions which are given by the normalized regular solutions of the radial Schrödinger equation evaluated at a set of energies $\{E_b\}$ within the range of valence states

$$\tilde{\phi}_{nlb}(r)=\frac{R^n_l(r;E_b)}{\sqrt{\int \mathrm{d}r\ r^2(R^n_l(r;E_b))^2}} \quad . \tag{4.55}$$

Usually four different energy points are sufficient for a proper basis construction. The use of the regular radial basis functions has two advantages: On the one hand they are numerically easy accessible and on the other hand they are well-suited to the problem.
In a next step, the overlap matrix

$$\mathcal{O}^{nl}_{bb'}=\int_0^{R_{\mathrm{WS}}}\mathrm{d}r\ r^2\tilde{\phi}_{nlb}(r)\tilde{\phi}_{nlb'}(r) \quad , \tag{4.56}$$

with fixed n and l is diagonalized, such that the eigenvalues and eigenvectors are available. Usually, it is sufficient to consider only the two largest eigenvalues and construct the normalized basis from the two associated eigenfunctions ϕ_{nlb}, which are linear combinations of $\tilde{\phi}_{nlb}$.

4.4. Non-collinear magnetism and spin-orbit coupling corrections

In the previous sections we discussed the KKR scheme for collinear magnetic structures without spin-orbit coupling. In this sections, we show how non-collinear structures can be treated and how

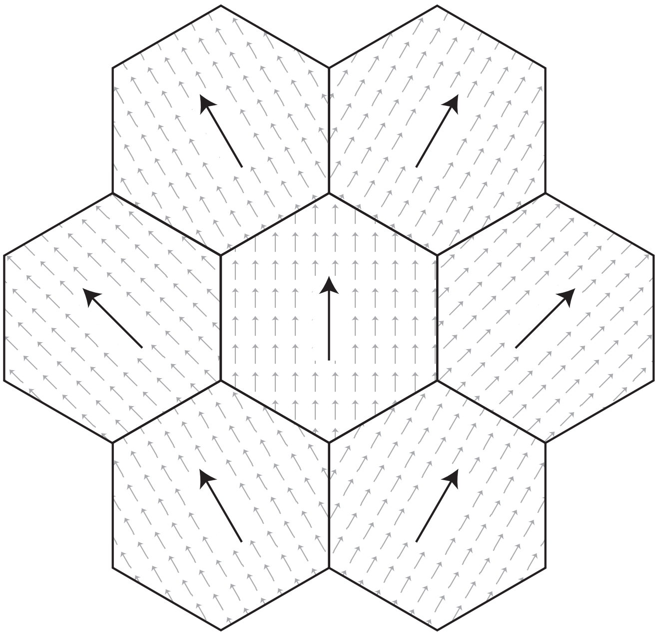

Figure 4.2.: Non-collinear magnetism in the rigid spin approximation. The spins are treated as collinear in each Voronoi cell.

to include spin-orbit coupling in the KKR formalism.

Figure 4.2 visualizes the treatment of non-collinear structures in the rigid-spin approximation, which is used in the KKR codes within self-consistency. Instead of considering the whole spatial dependence of the direction of the electrons magnetization, the magnetization direction is assumed to be constant in each Voronoi cell, respectively each WS sphere in the ASA. The non-collinear magnetization can be accessed at the end of the self-consistency cycle. Thus, if we consider a potential in cell n given in the global spin frame of reference by

$$\boldsymbol{V}^n(r) = V^n(r)\mathbb{1} - \mu_B \vec{\boldsymbol{\sigma}} \cdot B^n(r)\hat{u}^n \quad , \tag{4.57}$$

where $\hat{u}^n$ is pointing along the local direction of the magnetization given by (θ, ϕ), we can apply a local rotation in spin-space described by the rotation matrix $U^n(\theta, \phi)$ yielding

$$\boldsymbol{V}^n_{\mathrm{loc}} = U^n \boldsymbol{V}^n_{\mathrm{glob}} U^{n\dagger} = \begin{pmatrix} V^{n\uparrow}_{\mathrm{loc}} & 0 \\ 0 & V^{n\downarrow}_{\mathrm{loc}} \end{pmatrix} \quad , \tag{4.58}$$

which is diagonal in spin-space. Therefore, the discussion of the previous sections still holds, but the rotations have to be included carefully.

However, if we include spin-orbit coupling the theory has to be extended. The SOC term discussed in section 2.2 can be written as

$$\boldsymbol{V}^n_{\mathrm{SOC}} = \frac{1}{M(r)^2 c^2} \frac{1}{r} \frac{\partial V^n(r)}{\partial r} \vec{L} \cdot \vec{\boldsymbol{\sigma}} \tag{4.59}$$

where we choose $V^n(r) = \frac{1}{2}(V^{n\uparrow} + V^{n\downarrow})$ to be the average of spin up and spin down potential and $M(r)$ is the relativistic mass (see Appendix C). The total potential is given by

$$\boldsymbol{V}^n(r) = V^n(r)\mathbb{1} - \vec{\boldsymbol{\sigma}} \cdot B^n(r)\hat{u}^n + \boldsymbol{V}^n_{\mathrm{SOC}} \quad . \tag{4.60}$$

A rotation to the local frame yields

$$\boldsymbol{V}^n_{\text{loc}} = \begin{pmatrix} V^{n\uparrow}_{\text{loc}} & 0 \\ 0 & V^{n\downarrow}_{\text{loc}} \end{pmatrix} + U^n \boldsymbol{V}^n_{\text{SOC}} U^{n\dagger} \quad , \tag{4.61}$$

which is not diagonal anymore.
Thus we need to extend our theory to non-diagonal potentials, which is described in the work of Bauer [36]. The starting point is the Dyson equation (4.10). The Dyson equation can be written in two ways

$$G = G_0 + G_0 \Delta V G \tag{4.62}$$

$$G = G_0 + G \Delta V G_0 \quad , \tag{4.63}$$

which can be shown by plugging in the Green function iteratively. For diagonal potentials the order of multiplication does not matter, since the Green function is also diagonal. However, for non-diagonal potential it does matter. In the work of Bauer a proper ansatz for the Green function is discussed:

$$\boldsymbol{G}(\vec{r},\vec{r}\,') = \sum_L \left[\Theta(r'-r) R_L(\vec{r}) \bar{H}_L(\vec{r}\,') + \Theta(r-r') H_L(\vec{r}) \bar{R}_L(\vec{r}\,') \right] \quad , \tag{4.64}$$

with the Heaviside step function $\Theta(r-r')$, the right-hand side solutions R_L and H_L being column vectors and the left-hand side solutions $\bar{R}_L$ and $\bar{H}_L$ being row vectors.
At this point, we only discuss the regular solutions and refer to the work of Bauer for a more detailed discussion.
The left and right hand solutions are solutions of Lippmann-Schwinger equations, which can be seen as follows: Assume a single scattering potential of finite range R_{MT} and $r < R_{\text{MT}} < r'$. Plugging the ansatz eq. (4.64) into the Dyson equation (4.62) yields

$$\sum_L R_L(\vec{r}) \bar{H}_L(\vec{r}\,') = -\, i\sqrt{E} \sum_L Y_L(\hat{r}) j_l(\sqrt{E}r) \bar{h}_l(\sqrt{E}r') Y_L(\hat{r}') \tag{4.65}$$

$$+ \sum_L \int \mathrm{d}\vec{r}\,''\, \boldsymbol{G}_0(\vec{r},\vec{r}\,'';E) \Delta \boldsymbol{V}(r'') R_L(r'') \bar{H}_L(r') \quad . \tag{4.66}$$

With the boundary condition $\bar{H}_L(r) = H_L(r) = h_l(\sqrt{E}r)$ for $r > R_{\text{MT}}$ the equation can be simplified to

$$R_L(r) = -i\sqrt{E} j_l(\sqrt{E}r) Y_L(\hat{r}) + \int \mathrm{d}\vec{r}\,''\, \boldsymbol{G}_0(\vec{r},\vec{r}\,'';E) \Delta \boldsymbol{V}(r'') R_L(r'') \quad . \tag{4.67}$$

A similar approach, but assuming $r' < R_{\text{MT}} < r$ and using the Dyson equation (4.63) yields for the left-hand side regular solution

$$\bar{R}_L(r') = -i\sqrt{E} \bar{j}_l(\sqrt{E}r') Y_L(\hat{r}') + \int \mathrm{d}\vec{r}\,''\, \bar{R}_L(r'') \Delta \boldsymbol{V}(r'') \boldsymbol{G}_0(\vec{r}\,'',\vec{r}\,';E) \quad . \tag{4.68}$$

Comparing both equations shows, that the left- and the right-hand side solutions are different for potentials, which are not diagonal, since the order of multiplication matters as can be seen as follows: Assume a purely off-diagonal potential with different elements $V^{\uparrow\downarrow} \neq V^{\downarrow\uparrow}$. Due to the different order of multiplication the left-hand solution and the right-hand solution differ:

$$\begin{pmatrix} 0 & V^{\uparrow\downarrow} \\ V^{\downarrow\uparrow} & 0 \end{pmatrix} \begin{pmatrix} R^{\uparrow}_L \\ R^{\downarrow}_L \end{pmatrix} = \begin{pmatrix} V^{\uparrow\downarrow} R^{\downarrow}_L \\ V^{\downarrow\uparrow} R^{\uparrow}_L \end{pmatrix} \quad , \tag{4.69}$$

and

$$\left(\begin{array}{cc} \bar{R}_L^{\uparrow} & \bar{R}_L^{\downarrow} \end{array} \right) \left(\begin{array}{cc} 0 & V^{\uparrow\downarrow} \\ V^{\downarrow\uparrow} & 0 \end{array} \right) = \left(\begin{array}{cc} \bar{R}_L^{\downarrow} V^{\downarrow\uparrow} & \bar{R}_L^{\uparrow} V^{\uparrow\downarrow} \end{array} \right) \quad . \tag{4.70}$$

The full Green function containing the on-site scattering and the multiple scattering contributions is given by

$$\boldsymbol{G}(\vec{r} + \vec{R}_n, \vec{r}' + \vec{R}_{n'}) = \delta_{nn'} \boldsymbol{G}^n_{\text{on-site}}(\vec{r}, \vec{r}') + \sum_{LL'} R^n_L(\vec{r}) G^{nn'}_{LL'} \bar{R}^{n'}_{L'}(\vec{r}') \quad , \tag{4.71}$$

where the structural Green function are defined via a Dyson equation

$$G^{nn'}_{LL'}(E) = g^{nn'}_{LL'} + \sum_{n'',L''} g^{nn''}_{LL''} t^{n''}_{L''} G^{n''n'}_{L''L'} \quad , \tag{4.72}$$

with the t-matrix

$$t^n_L = \int \mathrm{d}\vec{r}\ \bar{j}_L(\vec{r}) \boldsymbol{V}^n(r) R_L(\vec{r}) \quad . \tag{4.73}$$

The projection scheme discussed in the previous section applies in the same manner by using the right-hand side solutions for the basis set construction. In addition it is assumed that the constructed basis $\phi_{nlb}(r)$ does not depend on the spin anymore, which simplifies spin rotations, since the spin dependence is only included in the Green function matrix element.

4.5. KKR programs

In this section a short overview of the used KKR programs and their purpose is given. We are using three different KKR programs– the Jülich-München (JM) program [39] and the KKRflex program with the extension KKRsusc.

The starting point is an accurate description of the host system, which is an infinite slab. The JM program simulates the host system by using the KKR Green function method in the ASA approximation. After a self-consistency cycle it gives access to the host Green function. In the JM program a cluster in real space is cut, which is used in the impurity program KKRflex. In the KKRflex program some of the vacuum sites in the cluster are replaced by impurities, e.g. one vacuum is replaced to simulate an adatom on top of the surface. Using a KKR Green function method in real space in the ASA approximation the KKRflex code is capable to describe the electronic structure of the cluster. Finally, the last used program is the KKRsusc program, which is an extension to the KKRflex program. Its main feature is the calculation of the magnetic susceptibility, which is achieved by the usage of the projection scheme discussed before. All implementation done in this work are embedded in the KKRsusc program.

4.6. Ground state currents within the KKR formalism

Up to now, we discussed the theory which is used to solve the Schrödinger equation in the KKR formalism. Using this approach we directly have access to the ground state Green function, which can be used to calculate the expectation value of any observable as shown in eq. (4.20).

In this section we show how to calculate ground state paramagnetic charge and spin currents within the KKR formalism. As shown in chapter 2 the paramagnetic charge and spin currents are given by

$$\vec{\boldsymbol{j}}^{\,a}_{\mathrm{para}}(\vec{r},\vec{r}\,') = -\,i\mu_B\left(\vec{\nabla}-\vec{\nabla}'\right)\boldsymbol{\sigma}^a \quad , \quad \text{with} \quad a=\{0,1,2,3\} \quad , \tag{4.74}$$

where we used $\boldsymbol{\sigma}^0 = \mathbb{1}$ to describe charge currents and $\boldsymbol{\sigma}^a$ to describe a-polarized spin currents. Using the Green function yields

$$\begin{aligned}
\vec{j}^{\,a}_{\mathrm{para}}(\vec{r}) &= -\frac{1}{\pi}\mathrm{Im}\int \mathrm{d}E\ f(E)\ \lim_{\vec{r}\,'\to\vec{r}}\mathrm{Tr}\ \left[\vec{\boldsymbol{j}}^{\,a}_{\mathrm{para}}(\vec{r},\vec{r}\,')\ \boldsymbol{G}(\vec{r},\vec{r}\,';E+i\eta)\right] && (4.75)\\
&= \lim_{\vec{r}\,'\to\vec{r}}\mathrm{Tr}\ \left[\vec{\boldsymbol{j}}^{\,a}_{\mathrm{para}}(\vec{r},\vec{r}\,')\boldsymbol{\rho}(\vec{r},\vec{r}\,')\right] \quad , && (4.76)
\end{aligned}$$

with the density matrix $\boldsymbol{\rho}$ defined via

$$\boldsymbol{\rho}(\vec{r},\vec{r}\,') = -\frac{1}{\pi}\mathrm{Im}\int \mathrm{d}E\ f(E)\ \boldsymbol{G}(\vec{r},\vec{r}\,';E+i\eta) \quad . \tag{4.77}$$

The density matrix is given in the projected Green function basis as

$$\boldsymbol{\rho}(\vec{r}+\vec{R}_n,\vec{r}\,'+\vec{R}_{n'}) = \sum_{\substack{LL'\\bb'}} Y_L(\hat{r})\phi_{nlb}(r)\boldsymbol{\rho}_{nLb;n'L'b'}\phi_{n'l'b'}(r')Y_{L'}(\hat{r}') \quad , \tag{4.78}$$

with

$$\boldsymbol{\rho}_{nLb;n'L'b'} = -\frac{1}{\pi}\mathrm{Im}\int \mathrm{d}E\ f(E)\ \boldsymbol{G}_{nLb;n'L'b'}(E) \quad . \tag{4.79}$$

Thus, the paramagnetic currents are given by

$$\begin{aligned}
\vec{j}^{\,a}_{\mathrm{para}}(\vec{r}) &= -\,i\mu_B \lim_{\vec{r}\,'\to\vec{r}}\left(\vec{\nabla}-\vec{\nabla}'\right)\mathrm{Tr}\ \left[\boldsymbol{\sigma}^a\boldsymbol{\rho}(\vec{r},\vec{r}\,')\right] && (4.80)\\
&= -\,i\mu_B\sum_{\substack{LL'\\bb'}}\Big[\left(\vec{\nabla}Y_L(\hat{r})\phi_{nlb}(r)\right)\mathrm{Tr}\ \left[\boldsymbol{\sigma}^a\boldsymbol{\rho}_{nLb;nL'b'}\right]\phi_{nl'b'}(r)Y_{L'}(\hat{r}) && \\
&\qquad - Y_L(\hat{r})\phi_{nlb}(r)\mathrm{Tr}\ \left[\boldsymbol{\sigma}^a\boldsymbol{\rho}_{nLb;nL'b'}\right]\left(\vec{\nabla}\phi_{nl'b'}(r)Y_{L'}(\hat{r})\right)\Big] \quad . && (4.81)
\end{aligned}$$

Due to the summation we can relabel $L \leftrightarrow L'$ and $b \leftrightarrow b'$ in the second summand which yields

$$\vec{j}^{\,a}_{\mathrm{para}}(\vec{r}) = -\,i\mu_B\sum_{\substack{LL'\\bb'}}\left(\vec{\nabla}Y_L(\hat{r})\phi_{nlb}(r)\right)\mathrm{Tr}\ \underbrace{\left[\boldsymbol{\sigma}^a\boldsymbol{\rho}_{nLb;nL'b'}-\boldsymbol{\sigma}^a\boldsymbol{\rho}_{nL'b';nLb}\right]}_{=\boldsymbol{\sigma}^a\Delta\boldsymbol{\rho}_{nLb;nL'b'}}\phi_{nl'b'}(r)Y_{L'}(\hat{r}) \quad , \tag{4.82}$$

where we defined $\Delta\boldsymbol{\rho}_{nLb;nL'b'} = \boldsymbol{\rho}_{nLb;nL'b'} - \boldsymbol{\rho}_{nL'b';nLb}$.
At this point we can discuss the basic requirements for finite paramagnetic ground state currents. From Eq. (4.82) one can see that at least $\Delta\boldsymbol{\rho}_{nLb;nL'b'}$ has to be finite. This means that the Green function can not be symmetric in the spatial arguments $\boldsymbol{G}(\vec{r},\vec{r}\,') \neq \boldsymbol{G}(\vec{r}\,',\vec{r})$. To see under which circumstances the Green function is not symmetric we use the spectral representation

$$\boldsymbol{G}(\vec{r},\vec{r}\,';E) = \sum_n \frac{\Psi_n(\vec{r})\Psi_n^\dagger(\vec{r}\,')}{E-E_n+i\eta} \quad . \tag{4.83}$$

It is obvious, that the Green function can only be non-symmetric if the eigenfunctions of the Hamiltonian can not be chosen real and therefore the Hamiltonian is not real. In the case of collinear magnetism without spin-orbit coupling the Hamiltonian can always be chosen real by rotating to

the local frame, such that the Green function is symmetric in the spatial arguments and there are no finite ground state currents.
In this work we consider two different effects yielding symmetry breaking of the Green function. Namely, we include spin-orbit coupling or we look at complex non-collinear magnetic structures.

In addition to the paramagnetic contribution, the ground state currents have different other terms which were discussed in chapter 2. All of them can be calculated straightforwardly by using the density matrix.

Implementation of the gradients

Computationally the main task in eq. (4.82) is to calculate the gradient of the spherical harmonic times the radial basis function. Of course, it would be possible to do this pointwise by using finite-differences, but without going into computational details it should be clear that this is not an efficient way.
Furthermore, we want to expand the currents in terms of spherical harmonics such that

$$\vec{j}^{\,a}(\vec{r}) = \sum_{L} \vec{j}^{\,a}_{L}(r) Y_L(\hat{r}) \quad . \tag{4.84}$$

Thus we need an efficient way, to calculate $j^{a}_{L}(r)$ starting from eq. (4.82).
By using the identity

$$\vec{a} \times \left(\vec{b} \times \vec{c}\right) = \vec{b}\left(\vec{a} \cdot \vec{c}\right) - \vec{c}\left(\vec{a} \cdot \vec{b}\right) \quad , \tag{4.85}$$

we can connect the momentum operator, which is basically the gradient, to the angular momentum operator $\vec{L} = \vec{r} \times \vec{p}$

$$\vec{r} \times \vec{L} = \vec{r} \times \left(\vec{r} \times \vec{p}\right) = \vec{r}\left(\vec{r} \cdot \vec{p}\right) - \vec{p} r^2 \tag{4.86}$$

$$\Rightarrow \vec{\nabla} = i\vec{p} = \hat{r}\frac{\partial}{\partial r} - i\frac{1}{r}\hat{r} \times \vec{L} \quad . \tag{4.87}$$

In this way, we have decomposed the gradient in a radial part and a spherical part, since the angular momentum operator only acts on the spherical components (θ, ϕ). Furthermore, the action of the angular momentum operator on spherical harmonics is given by

$$\vec{\nabla} Y_{lm}(\hat{r}) = -i\frac{1}{r}\sum_{m''} \hat{r} \times \vec{L}_{l,mm''} Y_{lm''}(\hat{r}) \quad , \tag{4.88}$$

where we defined the angular momentum matrix elements $\vec{L}_{l,mm''}$.
Thus we can write the gradient acting on the basis functions as

$$\vec{\nabla}\phi_{nlb}(r) Y_{lm}(\hat{r}) = \hat{r}\frac{\partial \phi_{nlb}(r)}{\partial r} Y_{lm}(\hat{r}) - i\frac{\phi_{nlb}(r)}{r}\sum_{m''} \hat{r} \times \vec{L}_{l,mm''} Y_{lm''}(\hat{r}) \quad . \tag{4.89}$$

Writing $\hat{r}$ in terms of real spherical harmonics and using Gaunt coefficients yields

$$\partial_\alpha \phi_{nlb}(r) Y_{lm}(\hat{r}) = \sum_{l'm'} \sqrt{\frac{4\pi}{3}} \left[C^{l'm'}_{lm;(lm)_\alpha} \frac{\partial \phi_{nlb}(r)}{\partial r} - i\frac{\phi_{nlb}(r)}{r} \sum_{m''} \epsilon_{\alpha\beta\gamma} C^{l'm'}_{lm'';(lm)_\beta} L^{\gamma}_{l,mm''} \right] Y_{l'm'}(\hat{r}) \tag{4.90}$$

$$= \sum_{l'm'} P^{\alpha}_{nlmb;l'm'}(r) Y_{l'm'}(\hat{r}) \quad , \tag{4.91}$$

where we used $(lm)_\alpha$ to indicate the spherical indices corresponding to the $\hat{r}_\alpha$ component and defined the matrix $P^\alpha_{nlmb;l'm'}(r)$ to shorten the following equations.
Combining eqs. (4.91) and (4.82) yields the paramagnetic ground state currents in the KKR basis

$$j^a_{\text{para};\alpha}(\vec{r}) = -\,i\mu_B \sum_{\substack{LL'L''\\bb'}} P^\alpha_{nLb;L''}(r) Y_{L''}(\hat{r}) \text{Tr}\ \left[\boldsymbol{\sigma}^a \Delta\boldsymbol{\rho}_{nLb;nL'b'}\right] \phi_{nl'b'}(r) Y_{L'}(\hat{r}) \quad , \tag{4.92}$$

with the polarization a and the direction α. Combining the two spherical harmonics by the use of an additional Gaunt coefficient yields the desired form given in eq. (4.84).

Orbital magnetic moment

As pointed out in section 2.4, the ground state charge current can be used to calculate the orbital magnetic moment

$$\vec{m}_\text{o} = \frac{1}{2} \int \text{d}\vec{u}\ \vec{u} \times \vec{j}_\text{para}(\vec{u}) \quad . \tag{4.93}$$

where we have to integrate over the whole space and $\vec{u}$ is the position in the global frame with a well defined origin. However, in the ASA approximation we have to split the integral into the used Wigner-Seitz spheres:

$$\vec{m}_\text{o} = \frac{1}{2} \sum_n \int_{\mathcal{V}_n} \text{d}\vec{u}\ \vec{u} \times \vec{j}_\text{para}(\vec{u}) \tag{4.94}$$

$$\overset{\vec{u}=\vec{r}+\vec{R}_n}{=} \frac{1}{2} \sum_n \int_{\mathcal{V}_n} \text{d}\vec{r}\ \left(\vec{r} + \vec{R}_n\right) \times \vec{j}^{\,n}_\text{para}(\vec{r}) \tag{4.95}$$

$$= \underbrace{\frac{1}{2} \sum_n \int_{\mathcal{V}_n} \text{d}\vec{r}\ \vec{r} \times \vec{j}^{\,n}_\text{para}(\vec{r})}_{\text{on-site contribution}} + \underbrace{\frac{1}{2} \sum_n \vec{R}_n \times \int_{\mathcal{V}_n} \text{d}\vec{r}\ \vec{j}^{\,n}_\text{para}(\vec{r})}_{\text{net current contribution}} \quad . \tag{4.96}$$

Thus, the orbital magnetization has two contributions: an on-site term, which is calculated in the cell-centered local frame of each Wigner-Seitz cell, and a contribution, which depends on the net currents flowing through the spheres. The usual way of calculating the orbital magnetic moment within the KKR codes is the direct evaluation of the angular momentum operator in every Wigner-Seitz sphere. This is done locally in each sphere corresponding to the on-site term in our approach. Thus our approach enables a more detailed calculation of the orbital magnetic moment including effects of the net currents. For all systems discussed in this work the net currents decay fast enough, so that eq. (4.96) is well-defined.

5. Ground state currents in magnetic clusters

In this chapter we present and discuss the results of ground state charge and spin currents in magnetic nanostructures. We show calculations of currents in magnetic adatoms, dimers and trimers on different surfaces. Mostly, we discuss iron atoms deposited on a platinum substrate.
For the charge currents we take two symmetry-breaking effects into account. Single adatoms and chains are calculated in a ferromagnetic state, using spin-orbit coupling to couple the spin and orbital degrees of freedom. Furthermore, we show a simulation of a compact trimer without spin-orbit coupling but with a complex non-collinear and non-coplanar structure ,where the coupling between the spin and orbital degrees of freedom arises from the emergent magnetic field created by the non-coplanar magnetic structure resulting in finite ground state charge currents [40].
In addition, for spin-currents we show a simulation without spin-orbit coupling, but including a magnetic field which is not aligned with the magnetization. Even if this is not the ground state of the system, we will discuss interesting effects in this system.
We start this chapter with the description of the systems under consideration.

5.1. Description of the systems

Figure 5.1 shows different systems which are used to discuss ground state currents. The top three structures show iron adatoms deposited on different platinum surfaces – namely on Pt(100), Pt(110) and Pt(111), which differ in terms of point group symmetry. The structures are treated ferromagnetic with an out-of-plane magnetization of the iron adatoms. The Pt(111) surface has a 3-fold symmetry, whereas the other surfaces have a rectangular arrangement of the atoms with a 2-fold symmetry in the case of Pt(110) and a 4-fold symmetry in the case of Pt(100).
The central structures show an iron dimer and an iron trimer chain deposited on Pt(111). The chains break the 3-fold symmetry of the lattice, such that only a mirror symmetry is left, which is in turn broken by the magnetized adatoms. In total, this yields interesting currents which will be discussed in a later section.
The last structure shown in figure 5.1 shows an iron trimer ring deposited on Pt(111) with a non-collinear alignment of the magnetic moments. This structure is used to generate ground state charge currents without spin-orbit coupling.

Computational details

To build all these structures, we take a relaxation of the adatoms towards the surfaces into account. Since the KKR codes are not appropriate for geometry optimization, these relaxations are calculated using the plane wave code Quantum Espresso [41]. Therefore we have to consider large supercells to minimize interactions between the periodic replica. A supercell with a total thickness of 10 layers of which 5 layers are platinum is considered. In-plane the supercell consists of 4 × 4 platinum atoms with one adatom on top of the surface. For the plane-wave calculation a cutoff

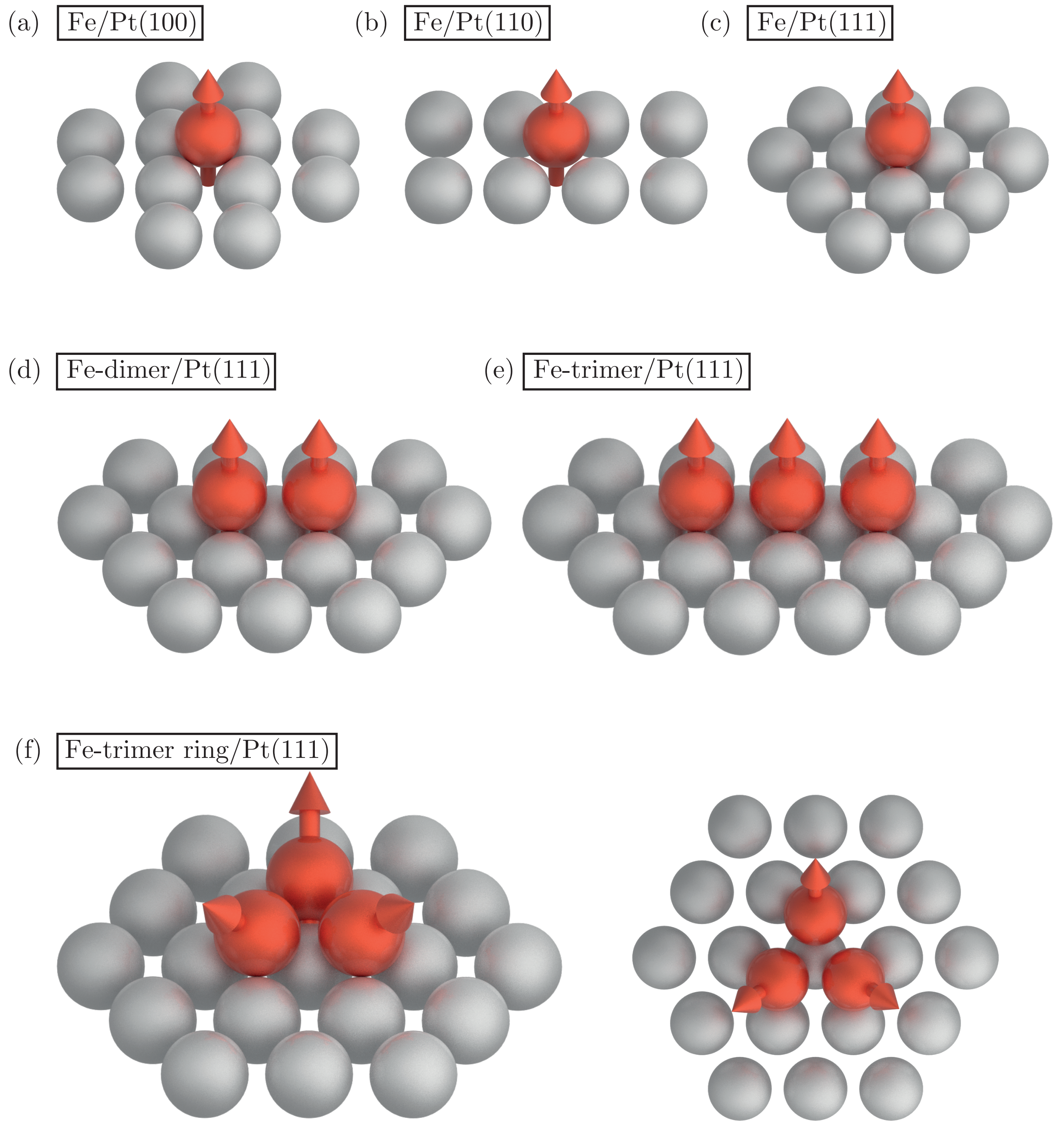

Figure 5.1.: Different structures, which are used for the calculation of ground state charge and spin currents. The three figures at the top show out-of-plane magnetized iron adatoms (red) on three different platinum surfaces (grey) – namely Pt(100) (a), Pt(110) (b) and Pt(111) (c). In the middle an iron dimer (d) and an iron trimer (e) with collinear, out-of-plane magnetization on top of Pt(111) is shown. The bottom figures (f) show a non-collinear iron compact trimer on top of Pt(111) in a side view and a top view.

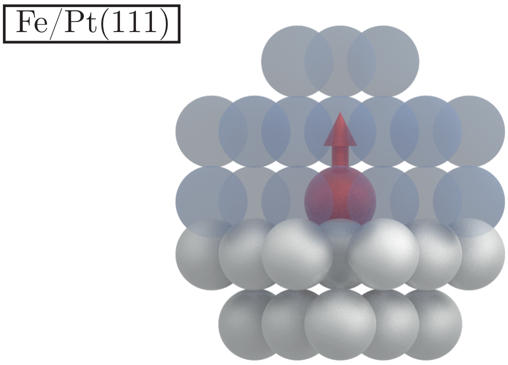

Figure 5.2.: Side view of the full cluster, which is considered for the iron adatom on Pt(111). The light blue transparent spheres indicate the vacuum spheres.

of 50 Ry and only one k-point – the Γ-point – is used. The calculations show a relaxation of the single adatoms of approximately 20% towards the surface, which differ only slightly for the three surfaces. For the dimers and trimers we approximate the relaxation by the one of the single adatom.

To setup the KKR simulation we start from the Jülich-Munich code [39] calculating the reference host system. The host is constructed by using 12 layers of platinum and 3 layers of vacuum on both sides of the slab, which are periodically repeated in two dimensions. In the next step, a cluster from the host is cut, which is usually a sphere around a vacuum site on top of the platinum surface including several shells of neighboring atoms. In the real-space code KKRflex with the KKRsusc add-on, this cluster is used to simulate the adatom on the surface. Therefore one vacuum site is replaced by an iron atom. The used cluster of an iron adatom on Pt(111) is shown in figure 5.2, where the blue transparent spheres indicate the vacuum sites.

Ground state properties of single iron adatoms on platinum surfaces

In the following the ground state properties of the single adatoms deposited on the different platinum surfaces are discussed. Table 5.1 shows the cluster size, the spin moment of the adatom, the summed spin moments of the cluster and the orbital moment of the adatom. The spin moments are all around the same value of $m_s \approx 3.4\mu_B$, whereas the orbital magnetic moments can vary by a factor of 2. Since the orbital magnetic moments are connected to ground state charge currents, we expect also the currents to vary a lot for the different surfaces, which will be shown later.

	Pt(100)	Pt(110)	Pt(111)
cluster size [#sites]	47	44	46
$m_s^{\text{adatom}}[\mu_B]$	3.38	3.35	3.46
$m_s^{\text{total}}[\mu_B]$	4.29	4.02	4.16
$m_o^{\text{adatom}}[\mu_B]$	0.07	0.17	0.14
$m_o^{\text{total}}[\mu_B]$	0.22	0.28	0.17

Table 5.1.: Ground state properties of single iron adatoms deposited on the three platinum surfaces.

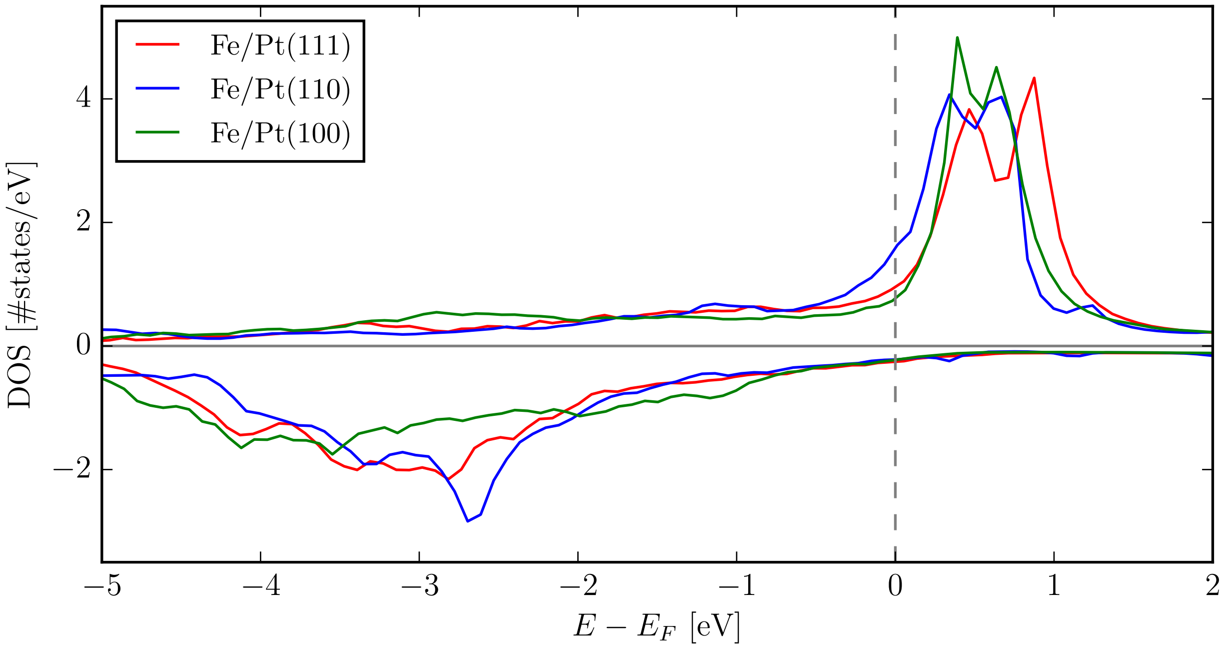

Figure 5.3.: Local density of states of the iron adatom on the three different surfaces. Positive and negative values are used to distinguish the two spin channels.

We can get more insight from the local density of states (DOS) of the adatom, which is shown in figure 5.3 for the three different surfaces. Positive and negative values in the DOS are used to distinguish majority and minority spin channels. The majority spin channel has a broad peak below the Fermi level, whereas the minority spin channel has a peak above the Fermi level. The integrated difference of these channels yields the spin moment discussed in the previous paragraph. The peak above the Fermi level is splitted, because of the crystal field. A more detailed analysis is shown in figure 5.4, which shows the local angular resolved density of states of the iron adatom on Pt(111). Shown are the $l = 2$ components which are described by real spherical harmonics. The C_{3v} symmetry of the Pt(111) surface yields three independent components of the DOS, such that the DOS for $\pm m$ is equivalent. Furthermore, one can see that the $m = \pm 2$ components, namely the xy and $x^2 - y^2$ components, have the largest density of states around the Fermi level.
Having this in mind, we discuss in the next section a simple model, which approximates the adatom on the Pt(111) surface.

5.2. Ground state charge currents and orbital magnetic moments

In this section, the resulting charge currents and the orbital magnetic moments for the different systems shown in figure 5.1 are discussed. In the first part, we discuss a model, which approximates a relevant portion of the electronic structure of an adatom on a hexagonal surface, e.g. an iron adatom on Pt(111). Afterwards, we show the results of the KKR simulations of the paramagnetic currents and the orbital magnetic moments. In addition, we discuss the corrections to the paramagnetic current arising from spin-orbit coupling and the Zeeman term. Finally, we discuss the non-collinear compact trimer, which shows finite orbital magnetic moments without spin-orbit coupling.

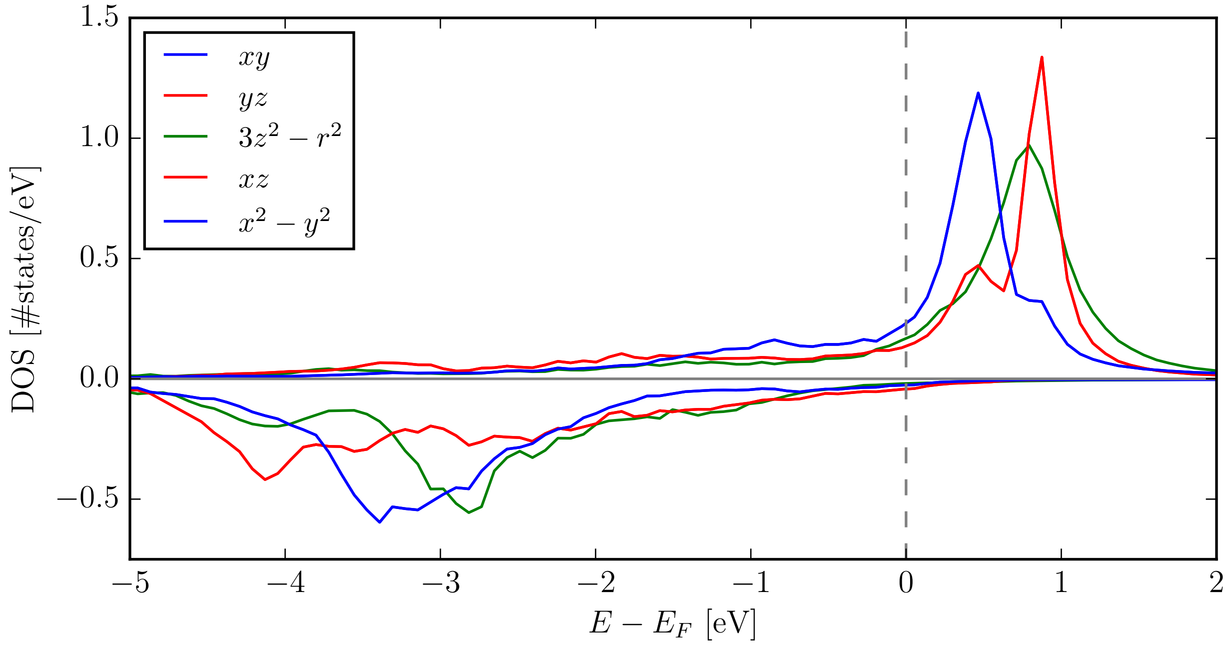

Figure 5.4.: Angular resolved local density of states of the iron adatom on Pt(111). Shown are the $l = 2$ components, which are described by five real spherical harmonics. Due to the symmetry of the lattice the DOS has in total three independent components.

5.2.1. Simple model calculation

A simple model Hamiltonian which is often used for impurities is given by the multi-orbital version of the Anderson impurity model [42].

The aim of the model calculation is the calculation of the ground state charge current. The contributions from the different orbitals shown in the DOS in figure 5.4 add up to the total ground state current. To simplify the model, we concentrate on the subset of the $(l, m) = (2, \pm 2)$ orbitals, which has two reasons: On the one hand the orbitals seem to be slightly more important in the DOS. On the other hand the orbitals have a stronger spin-orbit coupling than the other orbitals since the spin-orbit coupling strength is linear in m and it will turn out that spin-orbit coupling is responsible for the emergence of ground state charge currents. Furthermore, the DOS shows that only one spin-channel is reasonable occupied, which motivates the following structure of our model:

$$\mathcal{H}^{\text{eff}}_{mm'} = E_d \delta_{mm'} - \xi L^z_{mm'} - i\Gamma \delta_{mm'} \quad , \tag{5.1}$$

where m refers to the orbitals $(2, 2)$ and $(2, -2)$, E_d is the energy of the d-orbitals ($l = 2$), L^z is the angular momentum matrix element, ξ is the spin-orbit coupling coefficient and Γ describes a broadening.

Furthermore, the radial dependence of the orbitals is approximated by the so-called Slater-type orbitals yielding

$$\phi_m(\vec{r}) = R(r) Y_2^m(\hat{r}) \quad , \tag{5.2}$$

with $R(r) = Ar^2 e^{-\alpha r}$, where A is a normalization constant and α characterizes the length scale. Since the angular momentum matrix is not diagonal for real spherical harmonics we use complex spherical harmonics, for which it is diagonal

$$L^z_{mm'}\phi_m(\vec{r}) = m\delta_{mm'}\ \phi_m(\vec{r}) \quad , \tag{5.3}$$

such that the effective Hamiltonian in the $m = \{-2, 2\}$ basis is given by

$$\mathcal{H}^{eff} = (E_d - i\Gamma)\boldsymbol{\sigma}_0 - 2\xi\boldsymbol{\sigma}_z \quad . \tag{5.4}$$

By defining $\langle\vec{r}|\pm\rangle = \phi_{\pm2}(\vec{r})$ with the energies $E_\pm = E_d \mp 2\xi$ the Green function of the system can be written as

$$G(E) = (E - \mathcal{H}^{eff})^{-1} = \frac{|+\rangle\langle+|}{E - E_+ + i\Gamma} + \frac{|-\rangle\langle-|}{E - E_- + i\Gamma} \quad . \tag{5.5}$$

The density matrix can be calculated using the Green function

$$\begin{aligned}
\rho =& -\frac{1}{\pi}\int^{E_F} \mathrm{d}E \frac{G(E) - G^\dagger(E)}{2i} && (5.6)\\
=& -\frac{1}{2\pi i}\int^{E_F} \mathrm{d}E \left[\frac{|+\rangle\langle+|}{E - E_+ + i\Gamma} + \frac{|-\rangle\langle-|}{E - E_- + i\Gamma} - \text{h.c.}\right] && (5.7)\\
=& \int^{E_F} \mathrm{d}E \left[\frac{\Gamma/\pi}{(E - E_+)^2 + \Gamma^2}|+\rangle\langle+| + \frac{\Gamma/\pi}{(E - E_-)^2 + \Gamma^2}|-\rangle\langle-|\right] && (5.8)\\
=& \underbrace{\left[\frac{1}{\pi}\arctan\left(\frac{2\xi}{\Gamma}\right) + \frac{1}{2}\right]}_{=\rho_+}|+\rangle\langle+| + \underbrace{\left[-\frac{1}{\pi}\arctan\left(\frac{2\xi}{\Gamma}\right) + \frac{1}{2}\right]}_{=\rho_-}|-\rangle\langle-| \quad . && (5.9)
\end{aligned}$$

Using the density matrix the paramagnetic charge current is given by

$$\begin{aligned}
\vec{j}(\vec{r}) &= \lim_{r\to r'} -i\mu_B(\vec{\nabla}_r - \vec{\nabla}_{r'})\rho(\vec{r}, \vec{r}') && (5.10)\\
&= \lim_{r\to r'} -i\mu_B(\vec{\nabla}_r - \vec{\nabla}_{r'}) \sum_{m=\{\pm2\}} R(r)Y_2^m(\hat{r})\rho_m Y_2^{-m}(\hat{r}')R(r') \quad , && (5.11)
\end{aligned}$$

where we used $(Y_l^m)^* = (-1)^m Y_l^{-m} = Y_l^{-m}$ in the second step. Evaluating the gradient and taking the limits yields

$$\vec{j}(\vec{r}) = -i\mu_B \sum_m \left[\left(\vec{\nabla}R(r)Y_2^m(\hat{r})\right)\rho_m Y_2^{-m}(\hat{r})R(r) - R(r)Y_2^m(\hat{r})\rho_m\left(\vec{\nabla}R(r)Y_2^{-m}(\hat{r})\right)\right] \quad . \tag{5.12}$$

One can directly see, that the derivatives of the radial basis functions do not contribute, since the basis functions do not depend on m. Thus one finds

$$\begin{aligned}
\vec{j}(\vec{r}) &= -i\mu_B \sum_m R^2(r)\left[\left(\vec{\nabla}Y_2^m(\hat{r})\right)\rho_m Y_2^{-m}(\hat{r}) - Y_2^m(\hat{r})\rho_m\left(\vec{\nabla}Y_2^{-m}(\hat{r})\right)\right] && (5.13)\\
&= -i\mu_B \sum_m R^2(r)\left(\vec{\nabla}Y_2^m(\hat{r})\right)Y_2^{-m}(\hat{r})\left[\rho_m - \rho_{-m}\right] \quad . && (5.14)
\end{aligned}$$

where we swapped the indices $m \leftrightarrow -m$ in the second part, which is possible due to the symmetric summation interval.
Evaluating the gradients and plugging in the spectral density coefficients yields the final result for the current:

$$\vec{j}(\vec{r}) = \mu_B A^2 \frac{15}{8\pi^2}\arctan\left(\frac{2\xi}{\Gamma}\right)e^{-2\alpha r}\begin{pmatrix} -y\frac{x^2+y^2}{2} \\ x\frac{x^2+y^2}{2} \end{pmatrix} \quad . \tag{5.15}$$

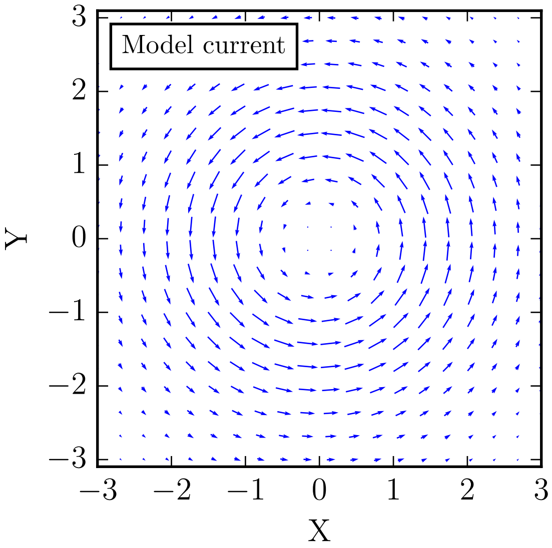

Figure 5.5.: Paramagnetic charge current of the model as given in eq. (5.15). X and Y are given in units of α. Shown is the $z = 0$ plane.

This current is a purely swirling vector field, which has zero divergence and satisfies the continuity equation. The current field is shown in figure 5.5.

In addition, the model can be used to examine the calculation of the orbital magnetic moment via the paramagnetic charge current. On one hand, the orbital magnetic moment can be calculated by using the expectation value of the angular momentum operator

$$m_{\mathrm{o}}^{z} = \mu_B \langle \hat{L}_z \rangle = \mu_B \mathrm{Tr}\ \hat{L}_z \rho \tag{5.16}$$

$$= \mu_B \left[\rho_+ \langle + | \hat{L}_z | + \rangle + \rho_- \langle - | \hat{L}_z | - \rangle \right] \tag{5.17}$$

$$= 2\mu_B \left(\rho_+ - \rho_- \right) = \frac{4}{\pi} \mu_B \arctan\left(\frac{2\xi}{\Gamma} \right) \quad . \tag{5.18}$$

On the other hand, we can use the paramagnetic current and calculate the orbital moment via eq. (2.41), which yields

$$\vec{m}_{\mathrm{o}} = \frac{1}{2} \int \mathrm{d}\vec{r}\ \vec{r} \times \vec{j}_{\,\mathrm{para}} \tag{5.19}$$

$$= \mu_B A^2 \frac{15}{16\pi^2} \arctan\left(\frac{2\xi}{\Gamma} \right) \int \mathrm{d}\vec{r}\ e^{-2\alpha r} \begin{pmatrix} -xz\frac{x^2+y^2}{2} \\ -yz\frac{x^2+y^2}{2} \\ \frac{(x^2+y^2)^2}{2} \end{pmatrix} \tag{5.20}$$

$$= \frac{4}{\pi} \mu_B \arctan\left(\frac{2\xi}{\Gamma} \right) \hat{e}_z \quad . \tag{5.21}$$

Thus both methods yield the same result.

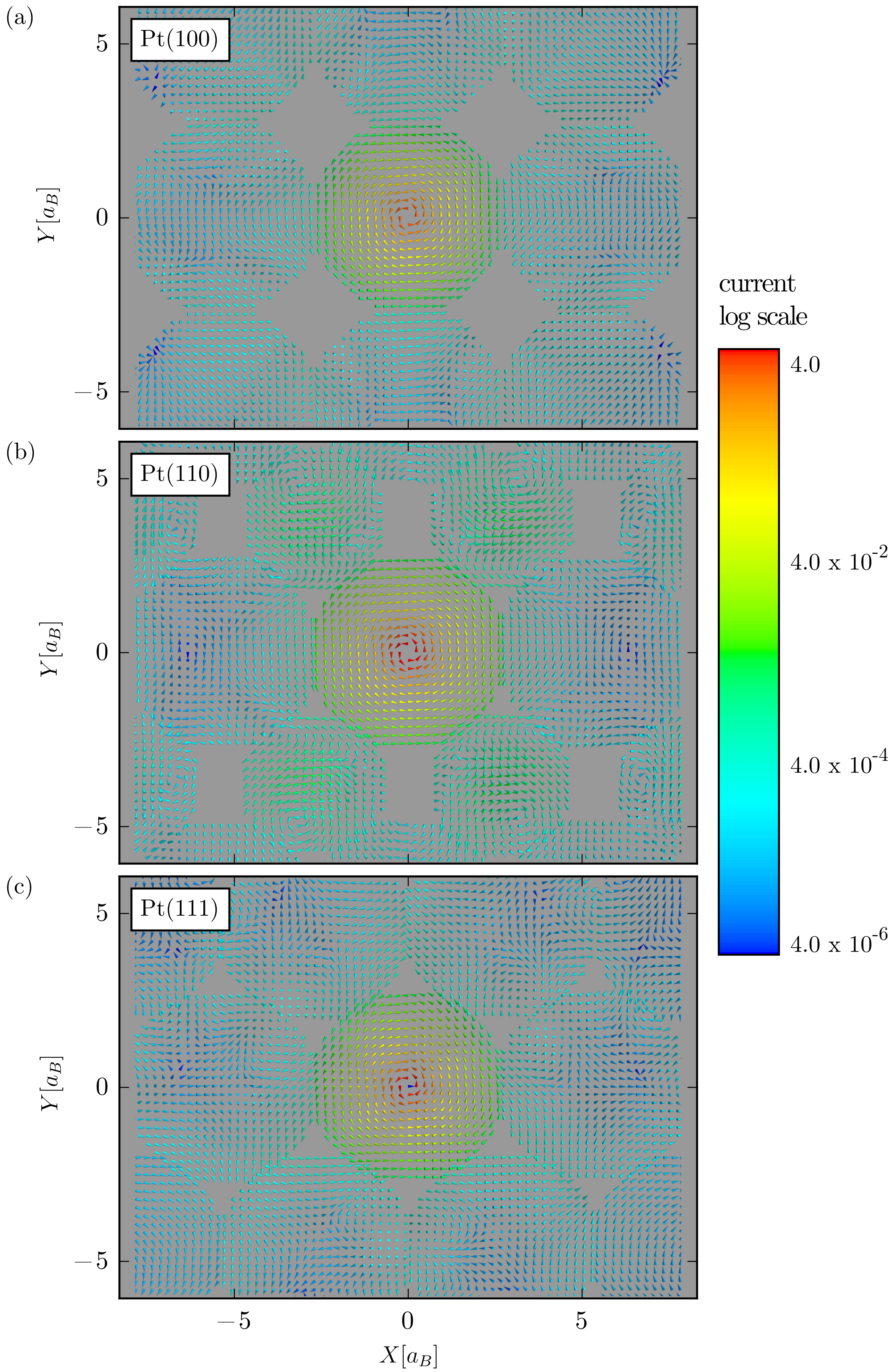

Figure 5.6.: Paramagnetic charge current computed according to eq. (4.82) for the adatom on the three different platinum surfaces. Shown is the $z = 0$ plane. The central sphere is the magnetic iron, whereas the surrounding spheres are vacuum sites.

5.2.2. Paramagnetic charge current and orbital magnetic moments

Single adatoms on platinum

Figure 5.6 shows the paramagnetic currents of the adatom on three different platinum surfaces calculated using the KKR approach. Shown are constant z cuts at the level of the adatom, such that the central spheres correspond to the adatoms, whereas the surrounding spheres are vacuum sites. The cones are pointing in the direction of the current and the color shows the absolute value of the current in a logarithmic scale.

Let us first concentrate on the adatom sphere. In all three cases the paramagnetic current is swirling in the x-y–plane. Furthermore, the currents are concentrated at the center of the sites decreasing exponentially with the distance. The interested reader might ask for the behavior of the currents at the center of the spheres: At a higher cone density it would become visible in the figure that the currents are not diverging at the center of the sphere. In total, the results match quite well the model calculation discussed in the previous section.

We also calculate the divergence of the current distribution. The divergence is up to a certain numerical precision zero. Thus the continuity equation is fulfilled. Unfortunately, the numerical precision for the calculation of the divergence is not very high. The problem is the way we calculate the derivatives, which is described in section 4.6. The derivatives are split into a radial and a spherical part. The radial part is a numerical derivative, whereas the spherical part is analytically given by the angular momentum matrix elements. In the case of the divergence these parts are both finite, but differ by a minus sign, which ends in a numerical error due to imperfect cancellation of the two contributions. Another problem is, that we work with spherical harmonics, such that the numerical error yields a divergence which has some spherical structure instead of being random noise. In total, one has to be very careful while interpreting the divergence in the present implementation.

Taking all sites into account, a drawback of the atomic sphere approximation becomes noticeable. The currents are only calculated inside the Wigner-Seitz spheres, which results in gaps and overlaps. On one hand there are regions without any information on the current and on the other hand there are regions with two different values for the current. For example in the case of Pt(110), see fig. 5.6(b), there are huge gaps in the y direction, which are filled with atoms from the vacuum layer above and the platinum layer below the adatom (small circles in the figure). At $z = 0$ the spheres have a finite overlap, which can be seen by the multiple arrows in that regions, and the currents do not perfectly coincide with each other in those regions. Disregarding this very special case, the overlap regions in figure 5.6 are mostly coinciding quite well.

In addition to the drawbacks discussed above, the current given on a fine grid as shown in figure 5.6 contains a lot of information, which is difficult to interpret in that form. Figure 5.7 shows the paramagnetic net currents of each sphere. The net currents are the averaged currents over the volume of the corresponding sphere. Shown are the x-y–projections of the currents in the adatom layer and the first platinum layer. The arrows corresponding to the three surfaces have the same scaling, but the currents in the adatom plane are scaled by a factor of 5 compared to the platinum plane.

For all surfaces, the net currents are swirling. Thus we can reproduce the swirling behaviour of the current inside the adatom sphere also on a larger length scale.

An interesting effect is related to the direction of the swirling. E.g. for the platinum layer at the

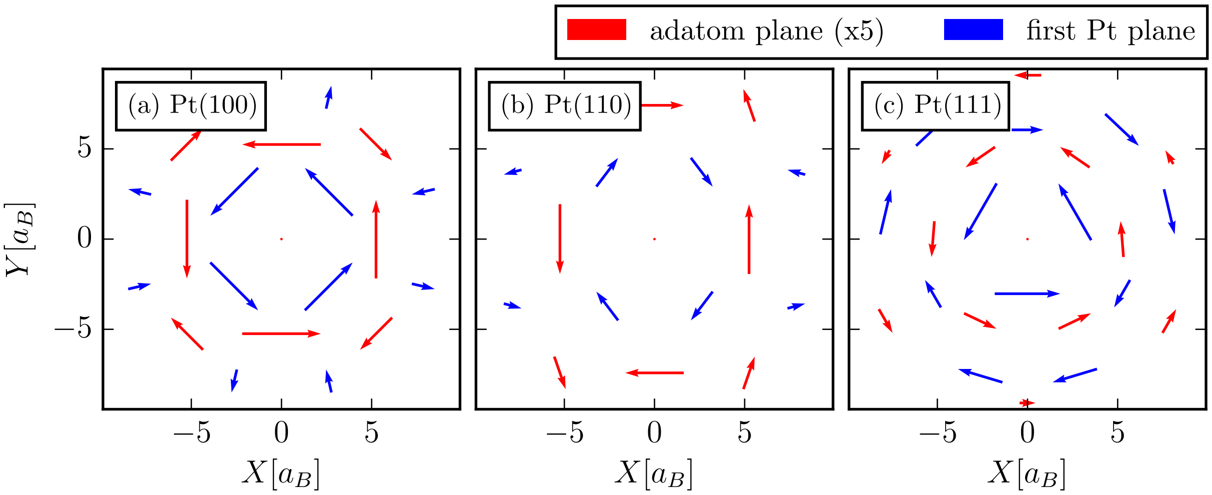

Figure 5.7.: Net paramagnetic currents in the three different surfaces. Shown are the adatom plane (red) and the platinum surface plane (blue). The arrows for the adatom plane are scaled by a factor of 5 compared to the platinum plane.

Pt(111) surface the direction is changing for larger distances to the adatom, see fig. 5.7(c). This is related to the so-called magnetic Friedel oscillations [43]. The swirling direction depends on the direction of the magnetic moment. In the case of collinear magnetism there are two possibilities – up and down. Due to the Friedel oscillations the magnetic moment oscillates as function of distance, which results in an oscillation of the swirling direction.

The paramagnetic charge current inside each sphere and the net currents can be used to calculate the orbital moment as shown in eq. (4.96). Figure 5.8 shows the orbital magnetic moments of the three different surfaces. The plots in the upper row show the adatom planes, whereas the plots in the lower row show the first platinum layer. For each atom there are two values – the on-site contribution and the net-current contribution (bold values). Shown are always the absolute values of the orbital magnetic moment. The on-site contributions match perfectly previous results, which were obtained by the evaluation of the angular momentum operator. This contribution depends on the local swirling of the paramagnetic current, which is related to the magnetic spin moment. Therefore, the values for the adatom are the largest and in the platinum plane the orbital moment is decreasing with distance to the adatom. The further away the platinum atoms are, the less is the magnetization and the swirling currents, which results in a lower orbital moment.
However, the net-current contribution is linear in the distance and the net-current. Therefore, the net-current contribution can be larger than the on-site term. E.g. for the platinum plane in Pt(111), see fig. 5.8(f), the net-current contribution of the outermost atoms is $5.6\mu_B$, whereas the on-site contribution is $3.5\mu_B$.
Table 5.2 shows the z-component of the on-site contribution and the net-current contribution summed over the whole cluster. The x and y-components vanish due to the symmetry of the cluster. The first column shows the orbital magnetic moment of the adatom, the second column shows the on-site contribution summed over the whole cluster and the last column is the net-current contribution summed over the whole cluster. For Pt(100) and Pt(110) the total on-site orbital moment is 3 times, respectively 1.7 times larger than that of the adatom, whereas the total on-site orbital moment of the Pt(111) cluster is just 16% larger. This difference is related to the magnetic Friedel oscillation. For Pt(111) the orbital moments cancel each other due to the oscillations. This effect

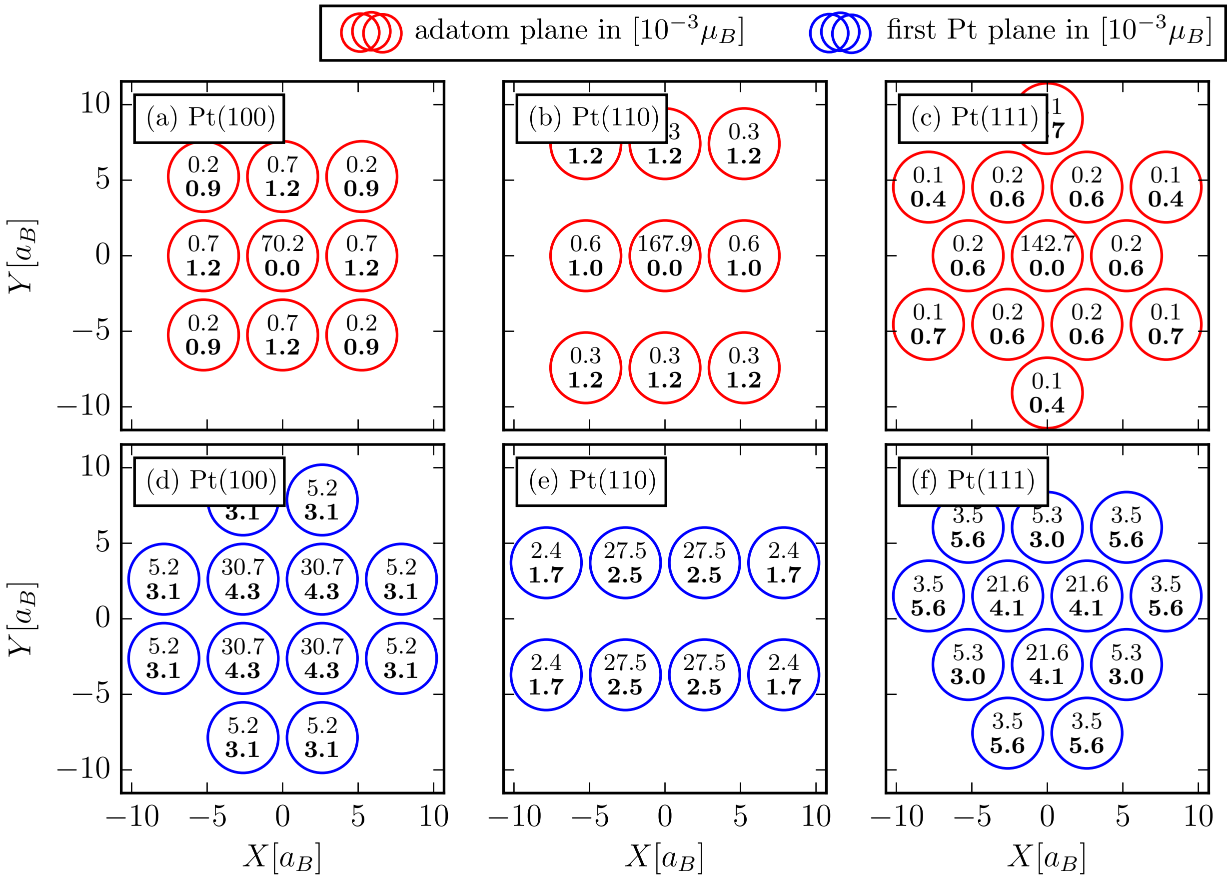

Figure 5.8.: Orbital moments in different structures. Upper value is the on-site contribution, whereas the lower bold value is the net current contribution. Shown are always absolute values. The circles represent the atomic spheres in each plane.

is weaker for the other surfaces, which can also be seen in the net-current in figure 5.7.
The summed net-current contribution is around ≈ 10% of the summed on-site contribution for

System	z-component of m^{orb}		
	m^{adatom}	$m^{\text{total}}_{\text{on-site}}$	$m^{\text{total}}_{\text{net-curr}}$
Pt(100)	70.2	215.3	19.9
Pt(110)	167.9	283.3	19.7
Pt(111)	142.7	165.6	-18.9

Table 5.2.: The z-component of the orbital magnetic moment for iron adatoms placed on three different surfaces as obtained from the ground state current calculation. The rows describe the Pt(100), Pt(110) and Pt(111) surface, whereas the columns show the orbital moment of the adatom m^{adatom}, the on-site orbital moment summed over the whole cluster $m^{\text{total}}_{\text{on-site}}$ and the net-current contribution summed over the whole cluster $m^{\text{total}}_{\text{net-curr}}$. The values match the ones in table 5.1. Values are given in units of $[10^{-3}\mu_B]$.

all three surfaces. Also here, the Pt(111) surface shows a different behaviour. The net-current contribution gives a negative correction to the on-site one, which can be understood by looking at the net-currents shown in figure 5.7. In the platinum plane the net-currents change the direction for the outermost atoms compared to the swirling direction of the adatom, which is anti-clockwise. The same happens for the other surfaces, but there are less atoms affected. In total this yields the negative correction.

If we were to increase the cluster size, the current would change the swirling direction once again. Thus, we expect the summed net-current contribution to be sensitive to the cluster size. For a proper calculation, one would need to increase the cluster sizes and try to converge the values, which was not attempted for this work.

Iron dimer and trimer on top of Pt(111)

The next systems we discuss are an iron dimer and trimer on Pt(111), see fig. 5.1(d)/(e). The resulting currents in the adatom plane are shown in figure 5.9. The large magnetic spin moments in the two, respectively three adatoms yield a strong swirling in each iron sphere, which is similar to the swirling in the adatoms.

Figure 5.10 shows the net-currents for the two systems. Shown are the adatom plane (red) and the first platinum plane (blue). The currents within the platinum plane behave similarly to the currents of the single adatom structures discussed above. The inner ring of platinum atoms has the same swirling direction as the local adatoms, whereas the swirling direction changes for the outer ring of platinum atoms. The reason for this are once again the Friedel oscillations.

Looking at the adatom planes an interesting effect occurs. The current flowing through the dimer, respectively the trimer chain is finite. Using symmetry relations we can explain this result: For the single adatom on Pt(111) the system has a 3-fold rotational symmetry, which results in a vanishing net-current in the adatom. For the chains, the rotational symmetry is broken. Left is a mirror symmetry along $y = 0$. Naively, one would expect this yielding also zero net-current. However, we are dealing with a magnetic system. Thus a parity operation (mirroring) has to be combined with a time-reversal operation, which is effectively a flip of the spin-moment. Under this circumstances, there is no symmetry left in the system, which results in the possibility of finite net-currents flowing in the chain.

Figure 5.11 shows the orbital moments for the dimer and the trimer. The upper values are the on-site orbital moment, whereas the lower bold values are the net-current contribution. One can see that especially for the outermost atoms in the platinum layer the net-current contribution is larger than the on-site contribution.

The summed orbital moments are shown in table 5.3. Due to the broken rotational symmetry the y-component can be finite, whereas the x-component is still vanishing due to the spatial mirror symmetry. The summed net-current contributions are finite and negative. The reason for this are the Friedel oscillations. Once again, these values depend heavily on the cluster size.

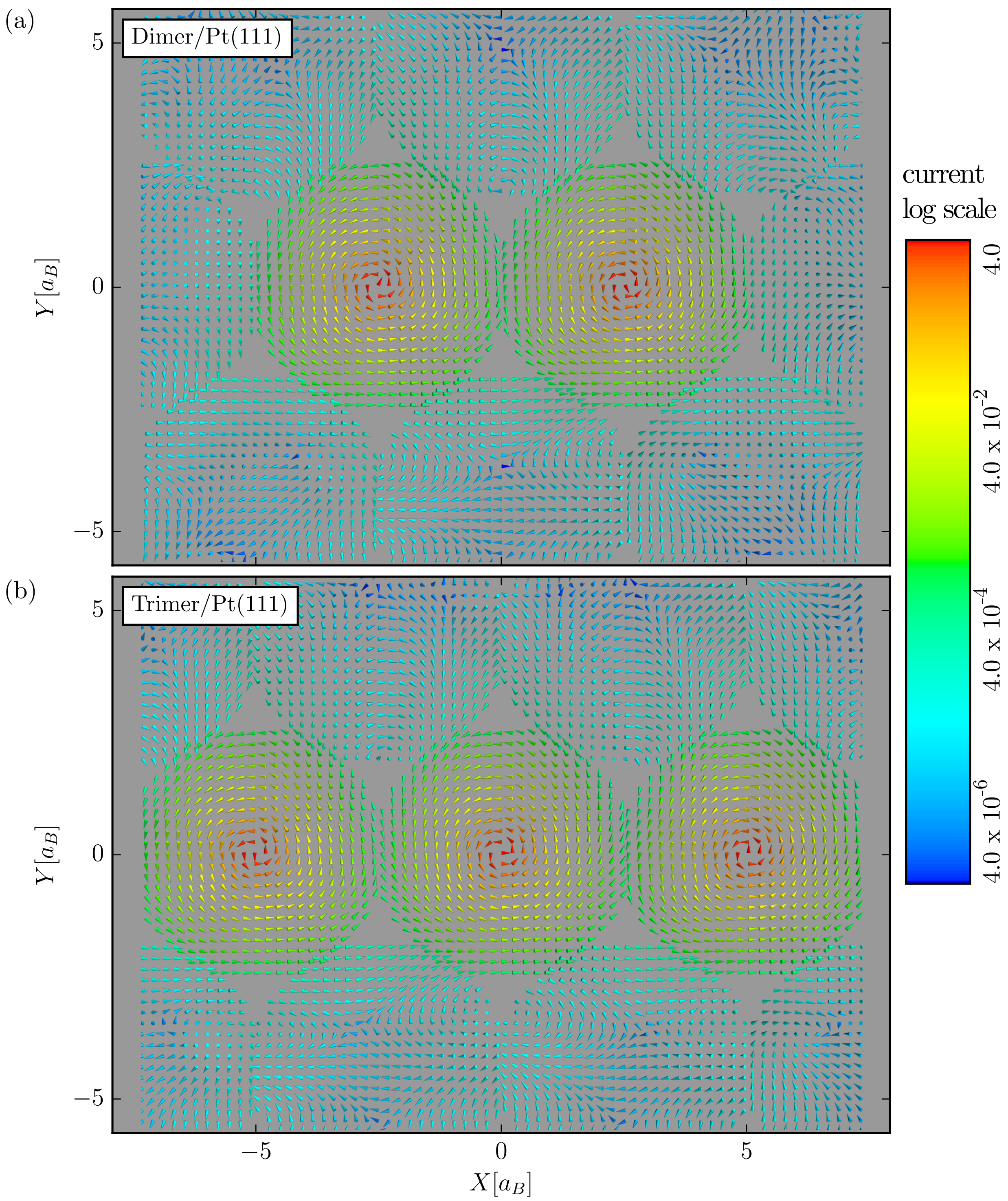

Figure 5.9.: Paramagnetic charge current for the iron dimer (a) and trimer (b) on top of Pt(111). Shown is the $z = 0$ plane.

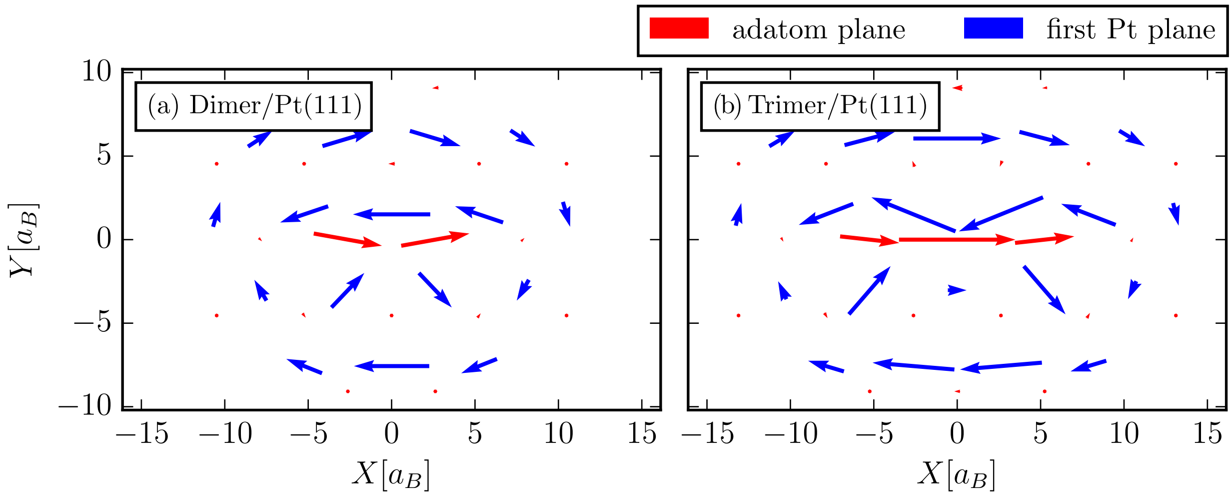

Figure 5.10.: Net currents in the iron dimer and trimer structure. Shown are the adatom plane (red) and the first platinum planes (blue).

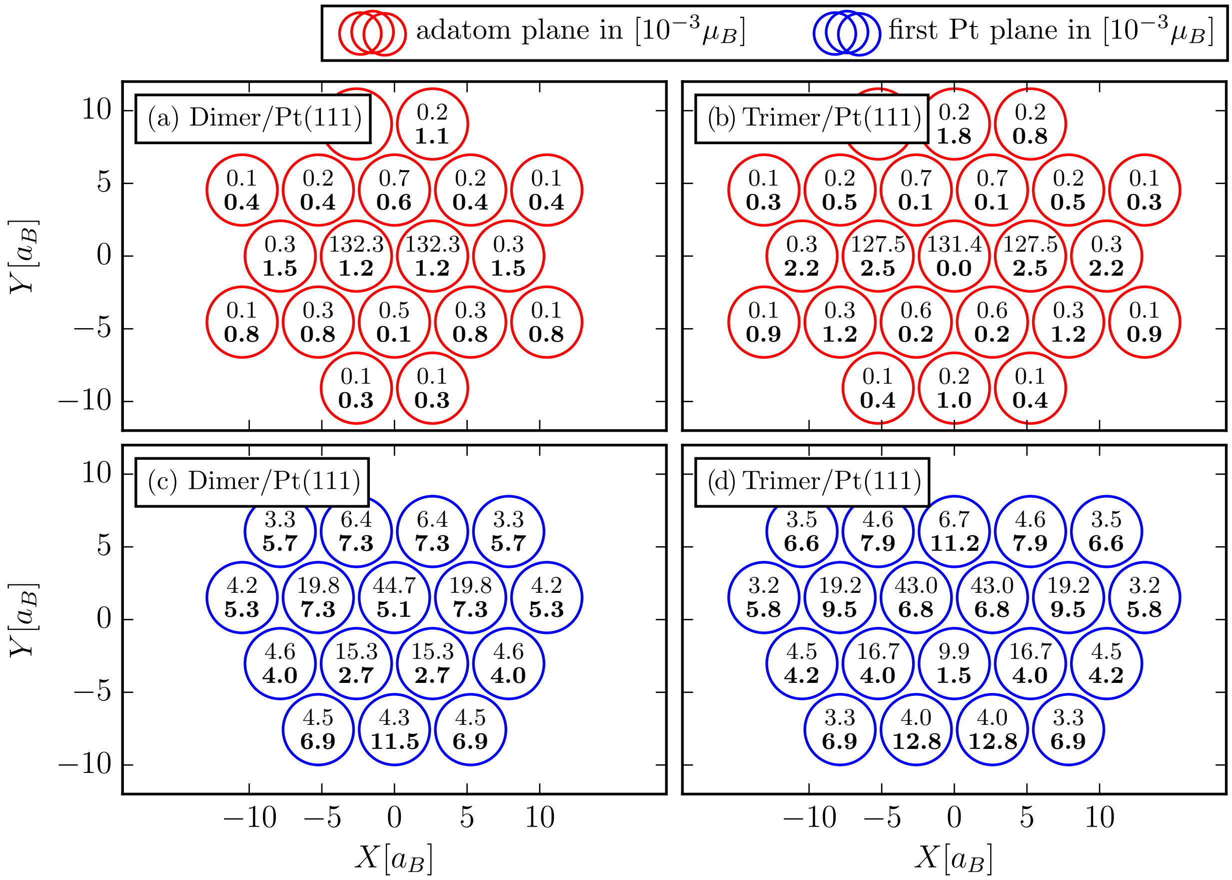

Figure 5.11.: Orbital moments in the iron dimer and trimer structure. Upper value is the on-site contribution, whereas the lower bold value is the net current contribution. Shown are always absolute values.

System	z-component		y-component	
	$m^{z,\text{total}}_{\text{on-site}}$	$m^{z,\text{total}}_{\text{net-curr}}$	$m^{y,\text{total}}_{\text{on-site}}$	$m^{y,\text{total}}_{\text{net-curr}}$
Dimer/Pt(111)	316.1	-39.7	45.9	-16.6
Trimer/Pt(111)	477.4	-66.0	84.6	-36.1

Table 5.3.: The z and y-component of the orbital magnetic moment for the iron dimer and trimer on Pt(111) given in $[10^{-3}\mu_B]$ as obtained from the ground state current calculation. The rows describe the dimer and trimer, whereas columns show the z and y-component of the on-site orbital moment summed over the whole cluster $m^{\text{total}}_{\text{on-site}}$ and the net-current contribution summed over the whole cluster $m^{\text{total}}_{\text{net-curr}}$.

5.2.3. Spin-orbit coupling contribution

In addition to the paramagnetic currents, in section 2.3.1 the spin-orbit coupling contribution to the charge current was discussed. It is a correction to the current in the continuity equation, which comes from the spin-orbit coupling part of the Hamiltonian. It is given by the cross product of the

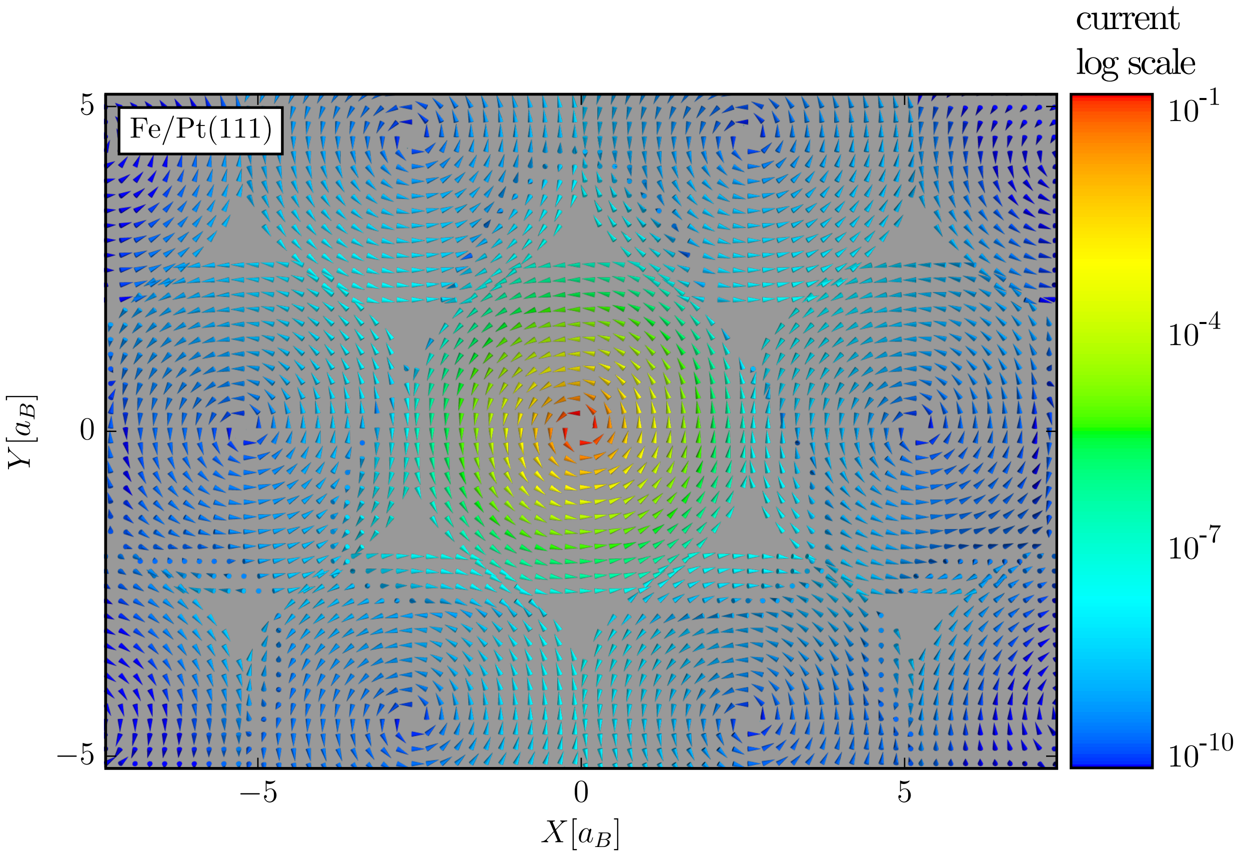

Figure 5.12.: Spin-orbit coupling charge current for the iron adatom on top of Pt(111). Shown is the constant $z = 0$–plane.

spin density and the electric field,

$$\vec{j}_{\mathrm{SOC}} = \frac{1}{c^2} \vec{m} \times \vec{E} \quad , \tag{5.22}$$

where the electric field is assumed to be radial. It is defined using the ionic potential $V(r)$ and the relativistic mass $M(r) = m + \frac{1}{2c^2}\left(E - V(r)\right)$:

$$\vec{E} = E_r \hat{e}_r \quad \text{with} \quad E_r = \frac{1}{(2Mc)^2} \frac{1}{r} \frac{\mathrm{d}V}{\mathrm{d}r} \quad . \tag{5.23}$$

Figure 5.12 shows the resulting SOC contribution to the charge current for an iron adatom on top of Pt(111). Shown is the $z = 0$ plane. The resulting currents are purely swirling. This is expected for any collinear structure, which can be seen as follows: The magnetization is pointing along the z-axis and the electric field is considered to be purely radial inside each sphere. Using eq. (5.22) this results in a purely swirling current for any collinear structure.

Regarding the amplitude of the currents, the SOC contribution inside the adatom sphere is around two orders of magnitude smaller than the paramagnetic contribution. In the vacuum spheres the SOC contribution even nearly vanishes with an amplitude smaller than $10^{-7}\mu_B$ as the SOC potential is negligible, due to the lack of the nuclear Coulomb potential.

In total, the SOC contribution is a very small correction to the paramagnetic current. Furthermore, it does not yield any new effects since its spatial structure is similar to the paramagnetic current, which is also swirling.

5.2.4. Zeeman contribution

In section 2.3.1 a third contribution to the charge current was introduced. It is the so-called Zeeman contribution to the charge current, which is given by the curl of the magnetization:

$$\vec{j}_{\mathrm{Zeeman}} = \vec{\nabla} \times \vec{m} \quad . \tag{5.24}$$

Figure 5.13 shows the Zeeman contribution for an iron adatom on top of Pt(111). Shown is the $z = 0$ plane. Inside the adatom sphere the Zeeman current is purely swirling. The amplitude is approximately one order of magnitude larger than the paramagnetic current.

However, the Zeeman current does not contribute to the divergence of the current even for systems which are not in the ground state. Therefore, in most literature it is neglected.

5.2.5. Charge currents without spin-orbit coupling

In this section the emergence of ground state charge currents without spin-orbit coupling is discussed. Complex non-collinear structures can yield the symmetry breaking, which is needed for the emergence finite ground state currents. We focus on the simplest structure with finite ground state currents, which is a trimer. It was predicted by Tatara *et al.* [44], that in magnetic structures with finite spin chirality

$$C_{123} = \vec{S}_1 \cdot \left(\vec{S}_2 \times \vec{S}_3\right) \neq 0 \quad , \tag{5.25}$$

ground state currents can emerge, which yield in turn finite orbital magnetic moments.

We focus on an iron trimer ring on top of Pt(111), which was presented in the beginning of this

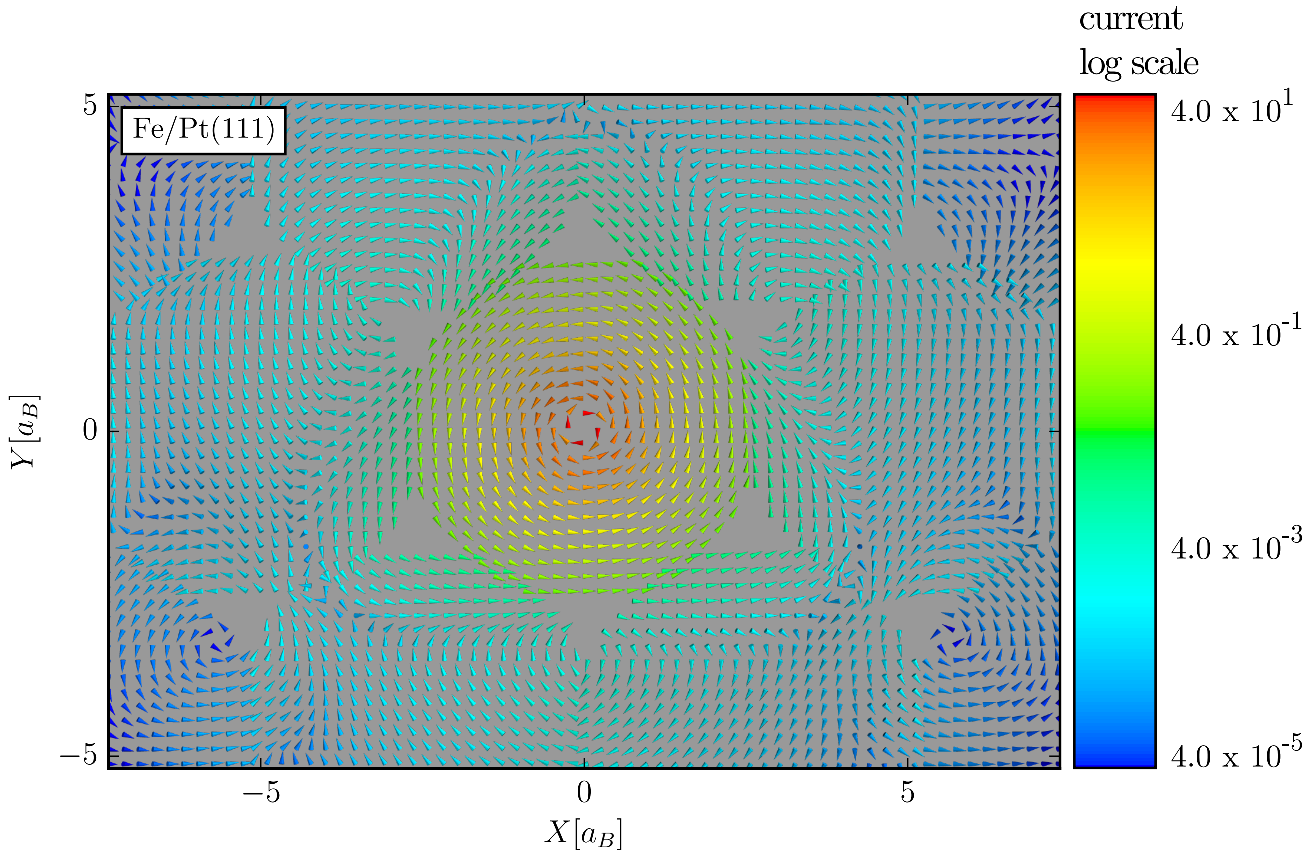

Figure 5.13.: Zeeman charge current for the iron adatom on top of Pt(111). Shown is the constant $z = 0$–plane.

chapter. The magnetic moments of iron are constrained to point outwards with a polar angle of $\theta = 45°$, see fig. 5.1(f), so that the chirality is positive and finite, which is called chiral right-handed. The true ground state is the ferromagnetic spin configuration. However, there are trimer systems having a ground state with finite chirality, e.g. a manganese trimer ring on top of Ni(111) as shown by Lounis [45].

Due to the complexity of the magnetic structure, the flow of the charge current is also more complex than in all cases shown before. However, the main characteristics are still the same: Close to the center of the Wigner-Seitz spheres the charge currents are swirling in the plane perpendicular to the magnetic moments. The visualization of all the details is difficult. Therefore, we restrict ourselves to the net currents and the orbital magnetic moment.

Figure 5.14 shows the net charge currents. Compared to the cases with spin-orbit coupling the net currents are decaying much faster with distance and there is no obvious influence of Friedel oscillations.

Figure 5.15 shows the orbital magnetic moments of the trimer ring structure decomposed in the on-site contribution and the net current contribution. The induced on-site orbital magnetic moment is approximately one order of magnitude smaller than the orbital magnetic moments induced by spin-orbit coupling. Furthermore, they are very localized so that reasonable values are only induced up to the nearest neighbour sites. However, the induced orbital magnetic moments depend crucially on the polar angle and the chirality, which was shown by dos Santos Dias [40]. Therefore, general comparison with the orbital moments induced by SOC is complicated.

System	z-component	
	$m^{z,\mathrm{total}}_{\text{on-site}}$	$m^{z,\mathrm{total}}_{\text{net-curr}}$
Trimer-ring/Pt(111)	26.1	10.9

Table 5.4.: The z-component of the orbital magnetic moment for the iron trimer ring deposited on Pt(111) with a non-collinear magnetic structure given in $[10^{-3}\mu_B]$. The columns show the on-site orbital moment summed over the whole cluster $m^{\mathrm{total}}_{\text{on-site}}$ and the net-current contribution summed over the whole cluster $m^{\mathrm{total}}_{\text{net-curr}}$.

The orbital moment contributions summed over the whole cluster are shown in table 5.4. Due to symmetry only the z-component remains finite after the summation. The net-current contribution is 10.9mμ_B, whereas the on-site contribution is 26.1mμ_B. Thus the net-current contribution is nearly 50% of the on-site contribution and therefore much more relevant compared to the cases discussed in the previous sections. The reason for this is the ring structure. There is a finite current flowing through the ring, which generates a large net-current contribution to the orbital magnetic moment. Increasing the size of the ring would probably increase the relevance of the net-current contribution.

5.3. Ground state spin currents

In this section we discuss the resulting spin-currents in magnetic nanostructures. In the first part we discuss spin-currents in adatoms, which are induced by spin-orbit coupling. Instead of looking at different structures, we focus on one certain structure – namely the iron adatom on Pt(111) –

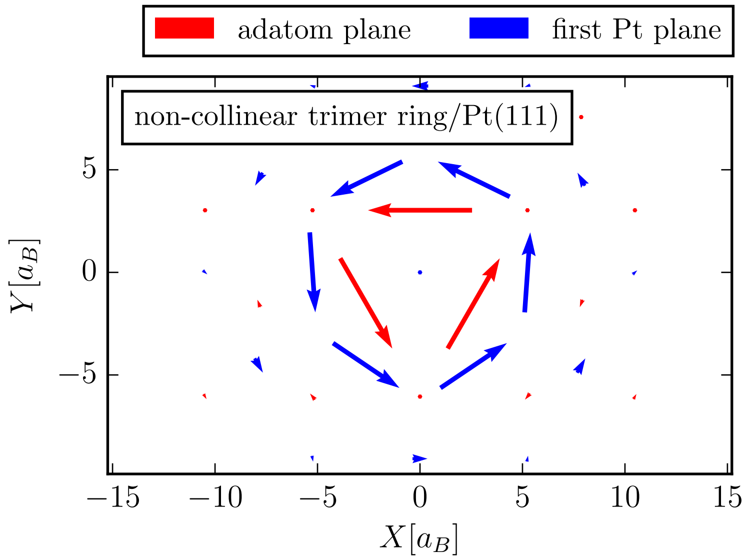

Figure 5.14.: Net currents in the iron trimer ring structure with non-collinear magnetization. Shown are the adatom plane (red) and the first platinum planes (blue).

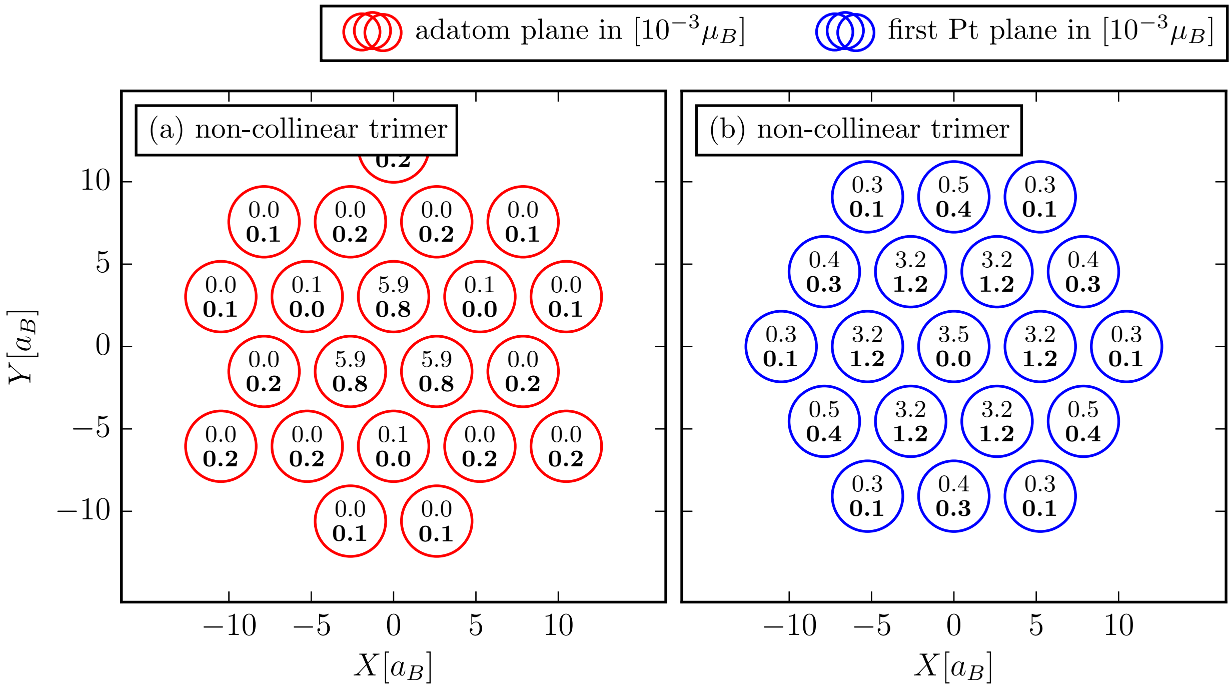

Figure 5.15.: Orbital moments in the iron trimer ring structure with non-collinear magnetization. Upper value is the on-site contribution, whereas the lower bold value is the net current contribution. Shown are the absolute values.

and show the spatial distributions of all three polarizations of the spin-current.
In the second part instead of spin-orbit coupling a magnetic field, which is not aligned with the magnetization, is used to break the symmetry, which is the main condition for finite currents. Of course, this is not the ground state of the system, but it gives first insights to dynamical effects, which are discussed in the next chapters.

5.3.1. Paramagnetic contribution

Let us first discuss the paramagnetic spin-current with z-polarization. In this case the diagonal Green function elements are used, which were also used for charge currents. Thus, we expect no fundamental new results or shapes of the current. Figure 5.16 shows the resulting paramagnetic spin-current with z-polarization inside the iron adatom on top of Pt(111). Shown is the constant $z = 0$-plane. The z-polarized current is swirling in the x-y-plane, which is similar to the calculations of the charge current shown in figure 5.6. The amplitude is a bit smaller, but of similar order. Overall, the results look reasonable.

Next, we discuss the x and y-polarized paramagnetic spin-currents. For the calculation of these currents, the off-diagonal Green function elements are relevant, which were not used before and therefore we have no expectations at this point.
Figure 5.17 shows the resulting spin-currents inside the iron sphere on top of Pt(111). Instead of looking at the surface-plane (x-y), which was used for all currents shown by now, the x-z-plane respectively the y-z-plane is used. The reason is that the spin-currents show a completely different

behaviour.

Let us look at the x-polarized spin-current. Shown is the y-z-plane with constant $x = 0$. One can see even in the figure that there is no large component in the x-direction, which would be needed for a swirling in the surface-plane. There are some large bound currents at the center of the sphere. However, the main effect is a finite current in the y-direction. Close to the platinum plane, which is at $z < 0$, the current is nearly constant into the y-direction, whereas at the top of the sphere there is no current compensating this. A similar result holds for the y-polarized spin-current. There are some bound currents at the center, but the main effect is a finite current in the negative x-direction.

Figure 5.18 shows the net-spin-currents for all three polarizations that is, the integral of the spin currents over the volume of the respective atomic spheres. Shown are the adatom plane and the first platinum plane. For the z-polarized currents the results look similar to the net charge currents. The currents are swirling in the platinum plane. However, for the x and y-polarized currents there is a constant flow at the surface. The x-polarized spin current flows in the positive y-direction, whereas the x-polarized spin current flows in the negative x-direction.

The spin current summed over the whole cluster, which includes a second layer of platinum and the vacuum sites on top, is shown in table 5.5. The z-polarized spin current is well behaving with a vanishing sum. The x and y-polarized spin currents show a finite total current in the y, respectively x-direction.

At first sight it seems to be a strange result, which might be wrong. However, the divergence of the currents (not shown) is still zero within the precision of the implementation. Therefore, the

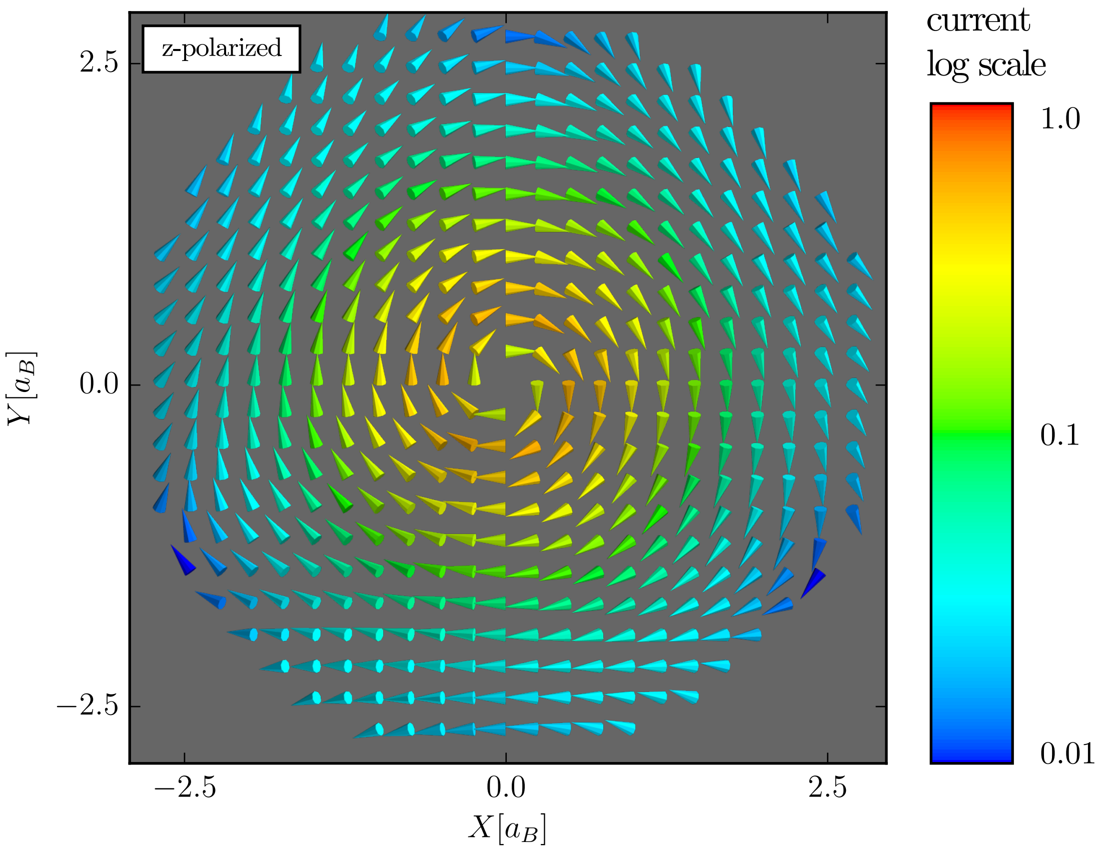

Figure 5.16.: Paramagnetic z-polarized spin-current inside an iron adatom on top of Pt(111). Shown is the $z = 0$ plane with the platinum surface below the adatom at $z < 0$.

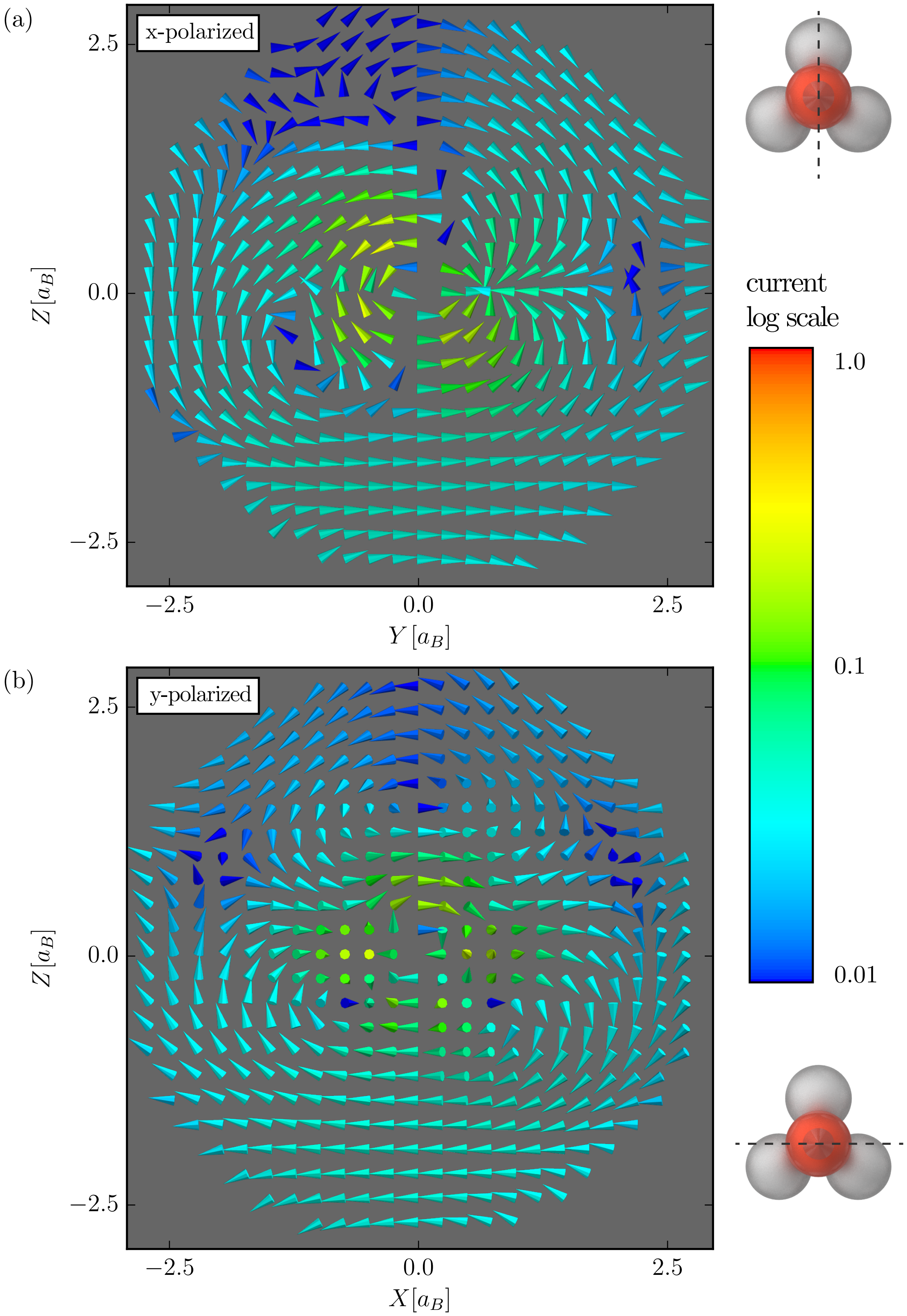

Figure 5.17.: Paramagnetic spin-currents inside an iron adatom on top of Pt(111). (a) shows the x-polarized spin-current. (b) shows the y-polarized spin-current. The platinum surface is below the adatom at $z < 0$. The structural models indicate the adatom in red, the three nearest-neighboring platinum atoms in grey, and the dashed line shows the cut planes for the corresponding spin current calculations.

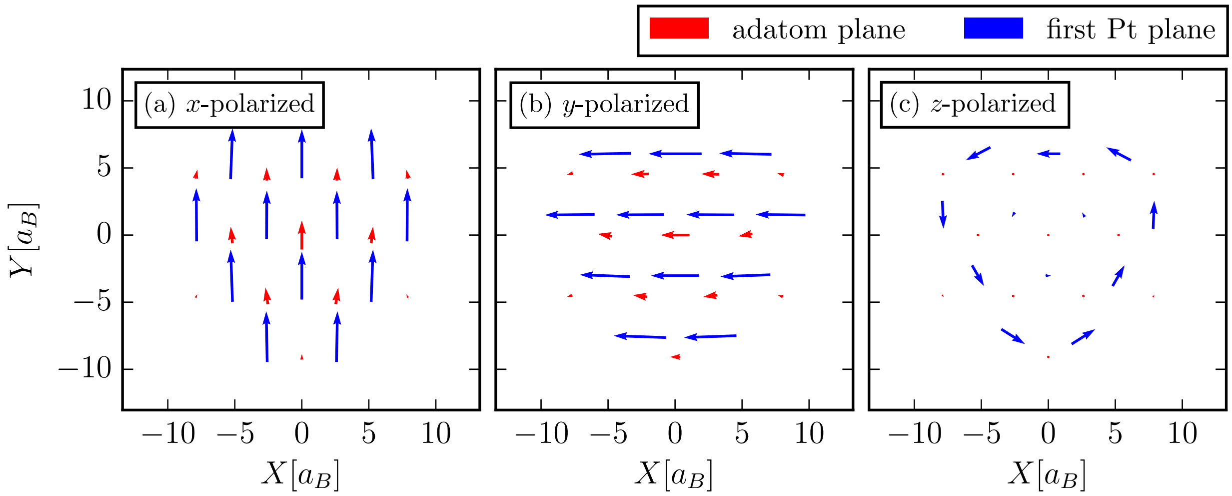

Figure 5.18.: Paramagnetic net-spin-currents for an iron adatom on top of Pt(111). Shown are the three different spin polarizations.

Polarization	spatial directions		
	x-direction	y-direction	z-direction
x	0.0	0.32	0.0
y	-0.32	0.0	0.0
z	0.0	0.0	0.0

Table 5.5.: The summed spin current over the whole cluster. Values are given in units of $[\mu_B]$.

continuity equation is fulfilled and there is no physical law, which forbids the finite currents at the surface.

It is also known that the so-called Rashba effect, which is a spin-orbit coupling effect splitting the momentum-dependent spin bands, can yield finite currents at the surfaces even in the absence of spontaneous magnetism [46].

Another possible origin for the finite currents is the way spin-orbit coupling is treated in the code. Presently, spin-orbit coupling effects are included only in the cluster and not in the host, which is used to construct the cluster. In the host an infinite two dimensional system is considered, which makes all atoms in one specific layer equal, whereas the atoms in the cluster have a much less symmetric environment. In total, this might be an important difference, which has to be analysed further.

5.3.2. Spin-orbit coupling contribution

Figure 5.19 shows the spin-orbit coupling contribution to the spin-currents. Shown is the iron adatom on top of Pt(111). The currents are swirling for all three polarizations. However, the swirling plane depends on the polarization. For x and y-polarized spin currents the planes are y-z, respectively x-z, whereas z-polarized spin-currents are swirling in the x-y-plane.

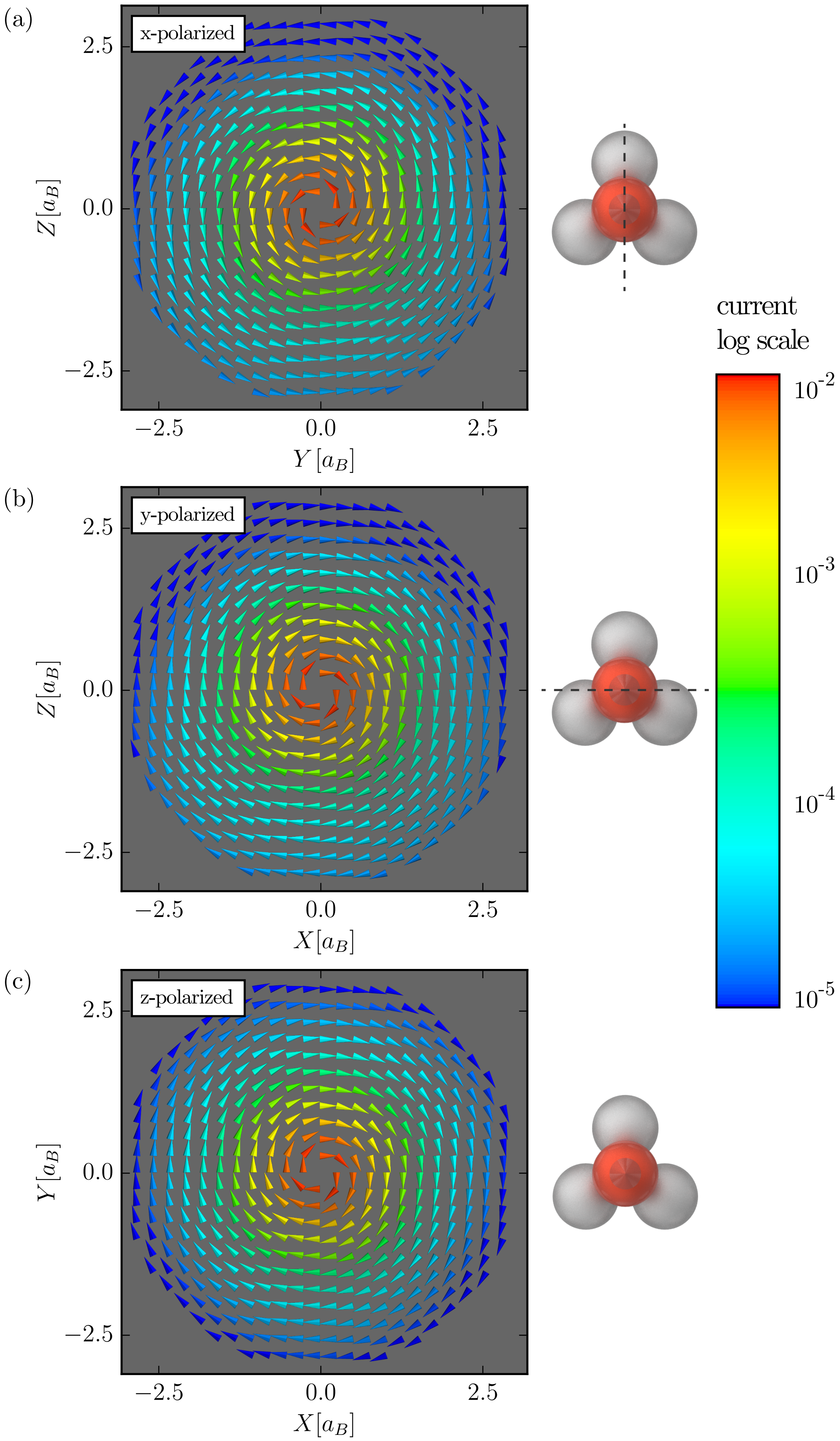

Figure 5.19.: Spin-orbit coupling contribution to the spin-current of the iron adatom sphere. Shown are the three different polarizations, which are all swirling, but in different planes.

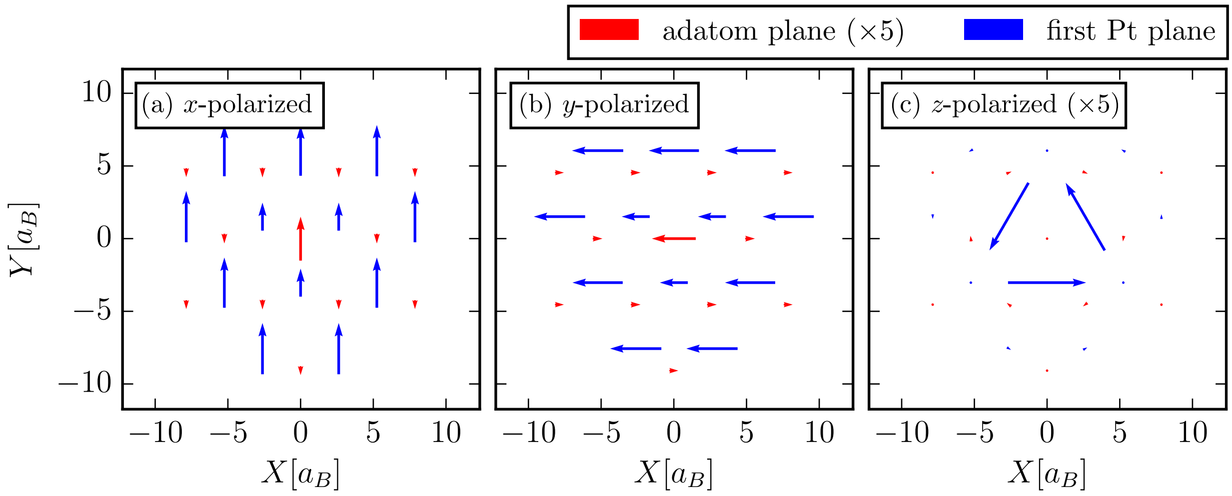

Figure 5.20.: SOC net-spin-currents for an iron adatom on top of Pt(111). Shown are the three different spin polarizations. The arrows of the adatom plane are scaled by a factor of 5 and the z-polarized currents are scaled by an additional overall factor of 5.

Polarization	spatial directions		
	x-direction	y-direction	z-direction
x	0.0	0.37	0.0
y	-0.37	0.0	0.0
z	0.0	0.0	0.0

Table 5.6.: The SOC contribution to the spin-current summed over the whole cluster. Values are given in units of $[10^{-3}\mu_B]$.

Given the definition of the SOC contribution to the a-polarized spin-current

$$\vec{j}^{\,a}_{\mathrm{SOC}} = \frac{\mu_B}{c^2} n \epsilon_{abc} E_b \hat{e}_c \quad , \tag{5.26}$$

which was discussed in section 2.3.2, the structure of the spin-currents is obvious since the electric field is considered to be radial, due to the spherical potential approximation.
Also in the SOC contribution we can see finite net currents emerging. The x and y-polarized currents show a distortion towards the surface. The amplitude of the currents at $-z$ is larger than the amplitude at $+z$. Therefore the currents do not compensate each other, which yields a finite net current pointing in the same direction as the paramagnetic currents.

Figure 5.20 shows the net-currents for the adatom plane and the first platinum plane. As already supposed from the currents inside the iron adatom, there are finite currents flowing through the structure, which are similar to the paramagnetic spin-currents.

Table 5.6 shows the SOC contribution to the spin-current summed over the whole cluster. In total this contribution is three orders of magnitude smaller than the paramagnetic term, but it has a similar structure.

To summarize, the paramagnetic and the SOC contribution show exactly the same behaviour. There are finite spin-currents flowing at the platinum surface. Since both methods are computationally completely different, we can conclude that either we found a Rashba behaviour at the surface [46], or the treatment of SOC is inappropriate and has to be extended to the host code, which could be done in the future.

5.3.3. Spin currents without spin-orbit coupling

In this section a magnetic field is used to generate spin-currents without spin-orbit coupling in a sort of gedankenexperiment. We revisit the Fe adatom on Pt(111). For the self-consistent calculation the system is converged with a magnetic field of 10 Tesla along the z-axis. For the calculation of the currents the potentials of the self-consistent calculation are used, but the magnetic field is tilted by 45° towards the x-direction. Therefore, we introduce a finite angle between the magnetic moment and the magnetic field, even if in the ground state both quantities would be fully aligned. Via the continuity equation this means that the divergence of the current should not be zero, since the time derivative of the magnetization can be finite because we are not in the ground state.

From the macroscopic point of view, the dynamics of a magnetic moment under the influence of a magnetic field can be described by the Landau-Lifshitz-Gilbert (LLG) equation:

$$\frac{\mathrm{d}\vec{m}}{\mathrm{d}t} = -\gamma\vec{m}\times\vec{B} + \alpha\vec{m}\times\frac{\mathrm{d}\vec{m}}{\mathrm{d}t}, \tag{5.27}$$

with the gyromagnetic ratio γ and the Gilbert damping constant α. The LLG equation is discussed in more detail in section 6.5.

The solution of the LLG equation describes a precession of the magnetic moment around the magnetic field, which is damped by the the Gilbert damping constant. The motion is shown in figure 5.21a. For the moment we can neglect damping effects, which is depicted in figure 5.21b.

In a conventional DFT calculation we do not have access to the dynamical motion of the magnetic moment. However, the simulation should inform us about the behaviour of the magnetic moments. The LLG equation predicts that initially only the y-component of the magnetic moment is changed. Via the continuity equation we can connect this change to the divergence of the y-polarized spin current. Therefore, we expect a finite y-polarized spin-current.

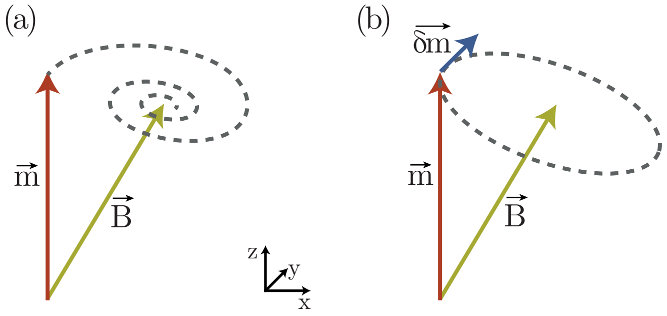

Figure 5.21.: Precession of a magnetic moment around a magnetic field, which is tilted into the x-direction. The dashed lines show the time evolution of the magnetic moment with finite damping in (a) and without damping in (b). The initial change of the magnetic moment δm is purely in the y-direction.

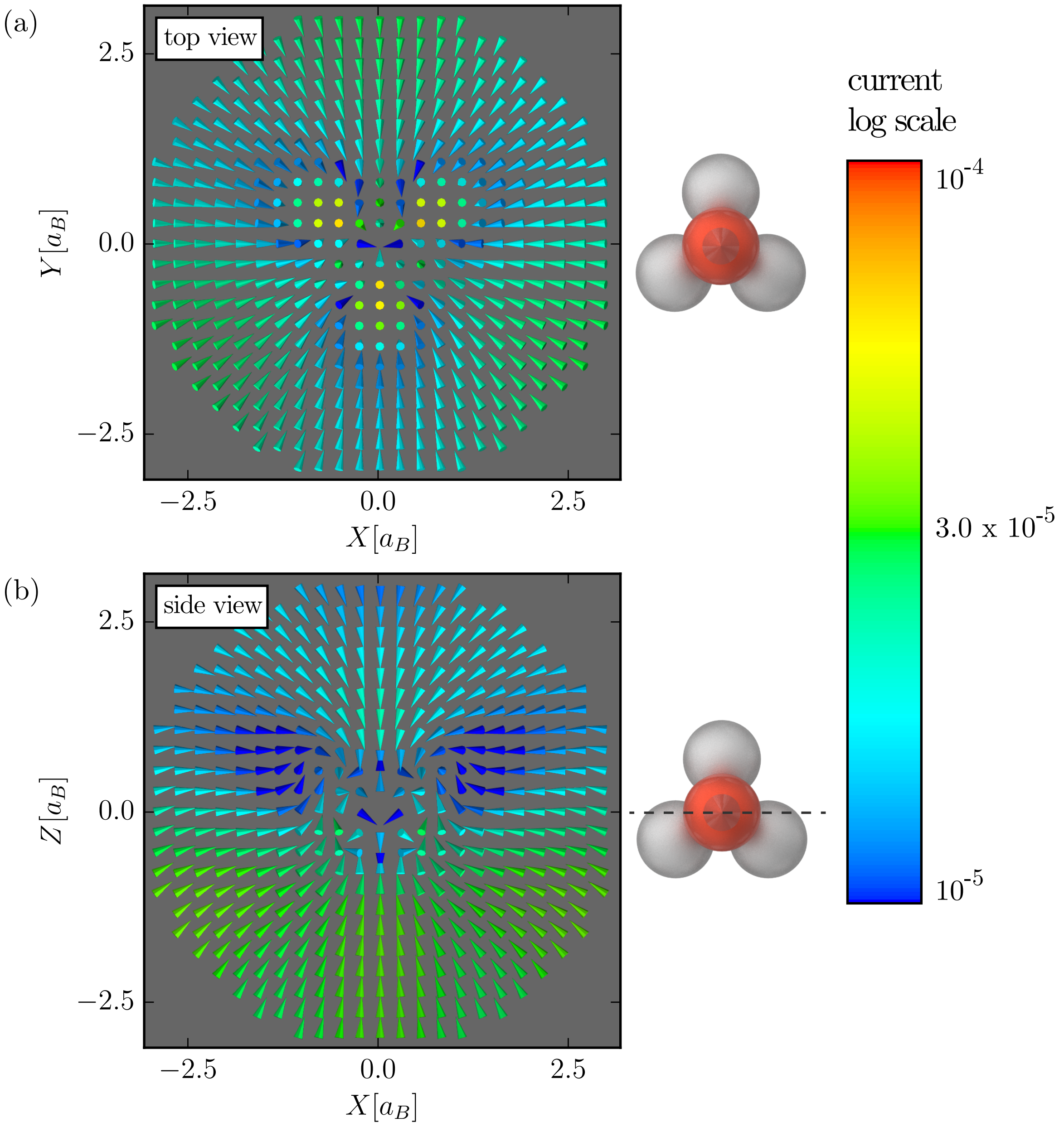

Figure 5.22.: Paramagnetic y-polarized spin-currents inside an iron adatom on top of Pt(111) induced by an external magnetic field, which is tilted by 45° towards the x-direction. Shown is the $z = 0$-plane, respectively the $y = 0$-plane.

Exactly this behaviour is found in the KKR simulation. Only the y-polarized spin currents are finite, which is shown in figure 5.22 for the iron adatom. The currents flow towards the center of the adatom from all directions. Therefore, the divergence is surely non-zero.

In the top view one can see the symmetry of the underlying lattice. The flow is larger in the directions of the nearest-neighbour platinum atoms.

The side view shows that there is a large current flowing from the platinum atoms ($z < 0$) towards the center, whereas the flow from the vacuum sites is much smaller, resulting in a finite net spin current perpendicular to the surface.

The net spin-currents are shown in figure 5.23. Shown are all atoms, but only the iron adatom and the three nearest-neighbour platinum atoms have visible contributions. One can see that there is

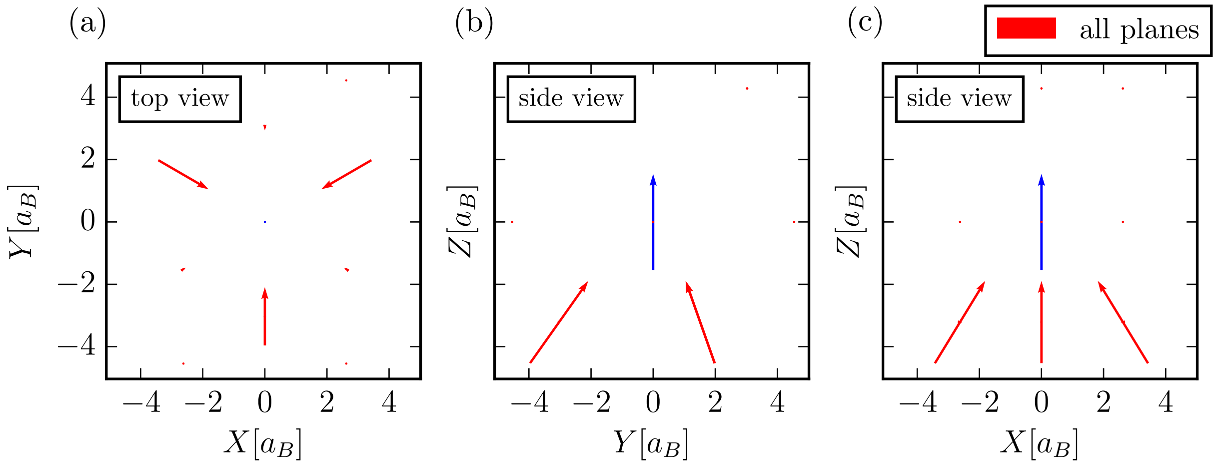

Figure 5.23.: Net y-polarized spin-currents for all atoms inside the cluster. Only the iron adatom (blue arrow) and the three nearest-neighbour platinum atoms have reasonable contributions.

a finite spin-current flowing towards the adatom.

However, this this should correspond to the short-time behavior. From the LLG equation we know that the magnetic moments precess, which means that there is a dynamical process inducing y- and x-polarized spin-currents. Furthermore, during one precession there are two opposite contributions. For example, after the magnetic moment has precessed by 180° there is a finite y-polarized spin-current, which is without damping the same as the initial one with a different sign. Therefore, after one precession there should not be any transferred current. However, one could imagine a very short magnetic field pulse, which yields an effective spin-pumping perpendicular to the surface.
In the next chapters we discuss the dynamical effects in more detail. On the way, we will see that there is always finite damping, which is induced by the spin-currents, and we will discuss the theory of spin-pumping. We start by introducing linear response theory within the KKR framework and discuss how to calculate spin-currents induced by static and dynamic magnetic fields.

5.4. Summary

In the following the most important results of this chapter are summarized. We presented KKR simulations of the ground state charge and spin currents in different nanostructures. We discussed the paramagnetic charge currents in an iron adatom deposited on Pt(100), Pt(110) and Pt(111) and in an iron dimer and trimer deposited on Pt(111). Concerning the orbital magnetic moment and its connection to ground state charge currents, we found two contributions – the on-site contribution and the net current contribution resulting from the net charge currents flowing through the Wigner-Seitz spheres. It turned out, that the net current contribution can either lower or higher the total orbital magnetic moment depending on the geometry. Usually we found contribution, which were around 10% of the on-site contribution.
In addition to the adatom systems, we discussed a compact iron trimer deposited on Pt(111), in which finite ground state currents evolve even without spin-orbit coupling. In this system, the net current contribution to the orbital magnetic moment was around 50% of the on-site contribution, which resulted from the finite charge flow through the compact trimer.

In addition to charge currents, we discussed ground state spin currents in an iron adatom deposited on Pt(111). The most important result was the emergence of finite net spin currents through the whole cluster, which can also be found in Rashba systems [46]. Furthermore, we showed the emergence of spin currents without spin-orbit coupling if the magnetic field and the magnetic moment are not aligned, which is not the ground state of the system.

In the next chapter, the basics of linear response are introduced. The aim is the description of dynamical induced spin-currents.

6. Spin currents within linear response

In this chapter we present a methodology for calculating spin-currents induced by dynamical magnetic fields. Assuming small magnetic fields as perturbation, the linear response theory can be utilized to describe the induced spin currents. Spin-currents and magnetization dynamics are closely connected, in the sense that magnetization dynamics can induce spin-currents. However, these two quantities are also mathematically closely connected. Therefore, it will be useful to start with a discussion of magnetization dynamics induced by magnetic fields.
The chapter is structured as follows: First, the basics of linear response theory are discussed with the main aim of defining the correlation function, which is used to describe the induced spin-current as well as the magnetization dynamics. Then, we present how to calculate magnetization dynamics within the linear response and how to include additional effects resulting from the TDDFT formalism, which yields a renormalization of the correlation function. Having the calculation scheme for the magnetization dynamics at hand, we discuss how to use these quantities to describe the dynamical induced spin-currents. After developing the whole method, it is applied to an Anderson model to earn first insights. Furthermore, we discuss the phenomenological Landau-Lifshitz-Gilbert model, which describes magnetization dynamics and can be extended by the spin-pumping theory [5].

6.1. Linear response theory

The linear response theory is a widely used formalism, which describes the response of any observable A to a weak perturbation. The main aim is to find the proportionality constant between the observable and the external perturbation in linear order. The procedure is well discussed in many excellent textbooks [35, 47]. The reader, who is familiar with Kubo's formula and the calculation of correlations functions using Green functions, can skip this section and continue with section 6.2.
Assume an external (time-dependent) perturbation described by $\mathcal{H}'(t)$, which is turned on at $t = t_0$, such that the total Hamiltonian is given by

$$\mathcal{H}(t) = \mathcal{H}_0 + \Theta(t - t_0)\mathcal{H}'(t) \quad . \tag{6.1}$$

The thermodynamic expectation value of the observable A can be calculated by using the eigenstates $|n(t)\rangle$ of the Hamiltonian via

$$\langle \hat{A} \rangle = \sum_n f_n(t) \langle n(t)|A|n(t)\rangle \quad , \tag{6.2}$$

with the occupation number $f_n(t)$. The time-dependence of the eigenstates can be calculated via the time-dependent Schrödinger equation

$$i\partial_t |n(t)\rangle = \mathcal{H}(t)|n(t)\rangle \quad . \tag{6.3}$$

It is convenient to use the so-called interaction picture, which is an intermediate representation between the Schrödinger and the Heisenberg picture. The trivial time evolution due to $\mathcal{H}_0$ is decoupled from the time evolution due to the external perturbation $\mathcal{H}'(t)$. Both, the eigenstates and the operator are time dependent in the interaction picture:

$$|n(t)\rangle = e^{i\mathcal{H}_0 t}|n(t)\rangle \tag{6.4}$$

$$A_\mathrm{I}(t) = e^{i\mathcal{H}_0 t}A_\mathrm{S}(t)e^{-i\mathcal{H}_0 t} \quad . \tag{6.5}$$

Using these definitions the Schrödinger equation becomes

$$i\partial_t|n(t)\rangle = \mathcal{H}'(t)|n(t)\rangle \quad , \tag{6.6}$$

such that the time evolution of the eigenstates in the interaction picture $|n(t)\rangle$ does only depend on the perturbation $\mathcal{H}'(t)$. The eigenstates in the interaction picture are given by

$$|n(t)\rangle = U(t,t_0)|n(t_0)\rangle \quad , \tag{6.7}$$

with the time evolution operator $U(t,t_0)$, which fulfills the differential equation

$$i\partial_t U(t,t_0) = \mathcal{H}'(t)U(t,t_0) \quad , \tag{6.8}$$

with the boundary condition $U(t_0,t_0) = 1$. The solution is given by an integral equation,

$$U(t,t_0) = 1 - i\int_{t_0}^{t} \mathrm{d}t'\ \mathcal{H}'(t')U(t',t_0) = 1 - i\int_{t_0}^{t} \mathrm{d}t'\ \mathcal{H}'(t') + \dots \quad . \tag{6.9}$$

In the linear response theory, the time evolution in eq. (6.2) is calculated up to first order in the perturbation $\mathcal{H}'(t)$, which yields the famous Kubo formula:

$$\langle A(t)\rangle = \langle A\rangle_0 - i\int_{t_0}^{t} \mathrm{d}t'\ \sum_n f_n(t)\langle n(t_0)|A(t)\mathcal{H}'(t') - \mathcal{H}'(t')A(t)|n(t_0)\rangle \tag{6.10}$$

$$= \langle A\rangle_0 - i\int_{t_0}^{t} \mathrm{d}t'\ \big\langle\big[A(t),\mathcal{H}'(t')\big]\big\rangle_0 \quad , \tag{6.11}$$

where $\langle\rangle_0$ indicates that the expectation value is evaluated with respect to the unperturbed Hamiltonian. This is a remarkable result, since it means that properties of the perturbed system can be calculated via expectation values evaluated in the unperturbed system.
The quantity appearing in the integral is the so-called retarted correlation function

$$C_{A,\mathcal{H}'}(t-t') = -i\Theta(t-t')\big\langle\big[A(t),\mathcal{H}'(t')\big]\big\rangle_0 \quad , \tag{6.12}$$

such that the Kubo formula can be written as

$$\delta\langle A(t)\rangle = \langle A(t)\rangle - \langle A\rangle_0 = \int_{t_0}^{\infty} \mathrm{d}t' C_{A,\mathcal{H}'}(t-t')e^{-\eta(t-t')} \quad , \tag{6.13}$$

where $\eta \to 0^+$ is added to ensure convergence.
For periodic perturbations, which are considered mainly in this work, it is convenient to work in the frequency space. Furthermore, one often deals with perturbations of the form $\mathcal{H}'(t) = B(t)\delta f(t)$. Thus, applying a Fourier transform to eq. (6.13) yields

$$\delta\langle A(\omega)\rangle = C_{A,B}(\omega)\delta f(\omega) \quad , \tag{6.14}$$

with the Fourier transform of the correlation function defined as

$$C_{A,B}(\omega + i\eta) = \int \mathrm{d}t\ e^{i(\omega+i\eta)t}C_{A,B}(t), \qquad (\eta \to 0^+) \quad . \tag{6.15}$$

The evaluation of the expectation values yields the so-called Lehman representation of the correlation function:

$$\begin{aligned} C_{A,B}(\omega+i\eta) =& \sum_{nm} f_n \left[\frac{\langle n|A|m\rangle\langle m|B|n\rangle}{\omega-(E_m-E_n)+i\eta} - \frac{\langle n|B|m\rangle\langle m|A|n\rangle}{\omega+(E_m-E_n)+i\eta} \right] \qquad (6.16) \\ =& \mathrm{Tr} \sum_{nm} f_n \left[B|n\rangle\langle n|A \frac{|m\rangle\langle m|}{\omega+E_n-E_m+i\eta} + A|n\rangle\langle n|B \frac{|m\rangle\langle m|}{-\omega+E_n-E_m-i\eta} \right] \quad , \qquad (6.17) \end{aligned}$$

where the cyclic invariance of the trace was used in the second step. Using the spectral representation of the Green function, see section 4.1, yields

$$C_{A,B}(\omega+i\eta) = \mathrm{Tr} \sum_n f_n \left[B|n\rangle\langle n|AG(\omega+E_n+i\eta) + A|n\rangle\langle n|BG(-\omega+E_n-i\eta) \right] \quad . \qquad (6.18)$$

In a next step, the Dirac identity can be used to rewrite the remaining sum over the basis functions $|n\rangle$ in terms of the Green function:

$$\int \mathrm{d}E\ M(E)\ G(E+i0^+) = \mathcal{P}\left[\int \mathrm{d}E\ M(E) \sum_n \frac{|n\rangle\langle n|}{E-E_n} \right] - i\pi \sum_n M(E_n)\ |n\rangle\langle n| \qquad (6.19)$$

$$\Rightarrow \qquad \sum_n M(E_n)\ |n\rangle\langle n| = -\frac{1}{\pi} \int \mathrm{d}E\ M(E)\ \mathrm{Im}\ G(E+i0^+) \quad , \qquad (6.20)$$

where $M(E)$ is an arbitrary function, which is in our case $M(E) = f(E)G(E \pm \omega \pm i\eta)$. Plugging this result into the expression for the correlation function yields:

$$\begin{aligned} C_{A,B}(\omega+i\eta) =& -\frac{1}{\pi} \int \mathrm{d}E\ f(E)\ \mathrm{Tr}\ \left[AG(\omega+E+i\eta)B\ \mathrm{Im}\ G(E+i0^+) \right] \\ & -\frac{1}{\pi} \int \mathrm{d}E\ f(E)\ \mathrm{Tr}\ \left[A\ \mathrm{Im}\ G(E+i0^+)BG(-\omega+E-i\eta) \right] \quad . \end{aligned} \qquad (6.21)$$

Thus knowing the Green function, any correlation function can be calculated.
The following important symmetry relations can be proven via the Lehman representation for hermitian operators [48]:

$$\begin{aligned} C_{A,B}(0) &= C_{B,A}(0) \\ \mathrm{Re}\ C_{A,B}(\omega) &= \mathrm{Re}\ C_{A,B}(-\omega) \\ \mathrm{Im}\ C_{A,B}(\omega) &= -\ \mathrm{Im}\ C_{A,B}(-\omega) \quad . \end{aligned} \qquad (6.22)$$

Thus it is sufficient to calculate the correlation function for $\omega \geq 0$.

Low frequency expansion

If the correlation function has no singular behavior for $\omega \to 0$, a Taylor expansion can be used for small frequencies:

$$C_{A,B}(\omega+i\eta) = C^{(0)}_{A,B}(0+i0^+) + \omega\ C^{(1)}_{A,B}(0+i0^+) + \frac{1}{2}\omega^2\ C^{(2)}_{A,B}(0+i0^+) + \dots \quad . \qquad (6.23)$$

The expansion coefficients can be calculated from eq. (6.21). For example the static correlation function is given by

$$\begin{aligned} C^{(0)}_{A,B}(0+i0^+) =& -\frac{1}{2\pi i} \int \mathrm{d}E\ f(E)\ \mathrm{Tr}\ \left[AG(E+i0^+)BG(E+i0^+) \right] \\ & +\frac{1}{2\pi i} \int \mathrm{d}E\ f(E)\ \mathrm{Tr}\ \left[AG(E-i0^+)BG(E-i0^+) \right] \quad . \end{aligned} \qquad (6.24)$$

6.2. Magnetic excitations within linear response

In this section we apply the linear response theory to magnetic excitations. Due to the close connection of magnetic excitations to spin-currents it is useful to first look at magnetic excitations. Furthermore, the developed calculation scheme applies in a similar way with only slight modifications to the calculation of spin-currents.

The convenient starting point is the response of the magnetization density and the charge density to an potential perturbation, which is either a magnetic field or an electrostatic potential. To simplify the notation we use 4-component vectors combining the magnetization density and the charge density:

$$\delta\underline{n}(\vec{r},t) = \begin{pmatrix} \delta\vec{m}(\vec{r},t) \\ \delta n(\vec{r},t) \end{pmatrix} \quad . \tag{6.25}$$

The perturbation can be written as

$$\delta\underline{\mathcal{H}}(\vec{r},t) = \begin{pmatrix} \vec{\boldsymbol{\sigma}}\ \delta\vec{B}(\vec{r},t) \\ \boldsymbol{\sigma}^0\ \delta V(\vec{r},t) \end{pmatrix} \quad \text{and} \quad \delta\underline{V}(\vec{r},t) = \begin{pmatrix} \delta\vec{B}(\vec{r},t) \\ \delta V(\vec{r},t) \end{pmatrix} \quad , \tag{6.26}$$

such that the response of the 4-component density is given by

$$\delta\underline{n}(\vec{r},t) = \int \mathrm{d}\vec{r}\,' \int \mathrm{d}t'\ \underline{\underline{\chi}}(\vec{r},\vec{r}\,';t-t')\delta\underline{V}(\vec{r}\,',t) \quad , \tag{6.27}$$

where $\underline{\underline{\chi}}$ is the susceptibility being a 4×4-matrix with the structure

$$\underline{\underline{\chi}} = \begin{pmatrix} \chi_{xx} & \chi_{xy} & \chi_{xz} & \chi_{xn} \\ \chi_{yx} & \chi_{yy} & \chi_{yz} & \chi_{yn} \\ \chi_{zx} & \chi_{zy} & \chi_{zz} & \chi_{zn} \\ \chi_{nx} & \chi_{ny} & \chi_{nz} & \chi_{nn} \end{pmatrix} \quad . \tag{6.28}$$

The susceptibility elements χ_{ab} with $a,b=\{x,y,z,n\}$ are defined as the retarted correlation function of $\boldsymbol{\sigma}^a$ and $\boldsymbol{\sigma}^b$:

$$\chi_{ab}(\vec{r},\vec{r}\,';t-t') = C^R_{\boldsymbol{\sigma}^a\boldsymbol{\sigma}^b}(\vec{r},\vec{r}\,';t-t') \quad . \tag{6.29}$$

Applying a Fourier transform yields

$$\delta\underline{n}(\vec{r},\omega) = \int \mathrm{d}\vec{r}\,'\ \underline{\underline{\chi}}(\vec{r},\vec{r}\,';\omega+i\eta)\delta\underline{V}(\vec{r}\,',\omega) \quad , \tag{6.30}$$

where $\chi_{ab}(\vec{r},\vec{r}\,';\omega+i\eta)$ can be written in terms of Green function as shown in eq. (6.21).

In general, all elements of χ_{ab} are finite. However, without spin-orbit coupling and without non-collinear magnetism the Green function is purely diagonal and the structure of χ_{ab} simplifies to

$$\underline{\underline{\chi}} = \begin{pmatrix} \chi_{xx} & \chi_{xy} & 0 & 0 \\ \chi_{yx} & \chi_{yy} & 0 & 0 \\ 0 & 0 & \chi_{zz} & \chi_{zn} \\ 0 & 0 & \chi_{nz} & \chi_{nn} \end{pmatrix} \quad , \tag{6.31}$$

such that longitudinal ($\{z,n\}$) and transversal ($\{x,y\}$) components are fully decoupled. Further simplifications can be made taking into account the symmetry of the system.

6.2.1. Susceptibilities within TDDFT

Within the TDDFT scheme we are working with the single-particle Kohn-Sham Hamiltonian

$$\mathcal{H}^{\mathrm{KS}} = -\nabla^2 + V^{\mathrm{KS}}(\vec{r},t) + \boldsymbol{\vec{\sigma}} \cdot \vec{B}^{\mathrm{KS}}(\vec{r},t) \quad , \tag{6.32}$$

with the Kohn-Sham potentials

$$\begin{aligned} V^{\mathrm{KS}}(\vec{r},t) =& V^{\mathrm{ext}}(\vec{r}) + \delta V(\vec{r},t) + \int \mathrm{d}\vec{r}' \, \frac{2n(\vec{r}',t)}{|\vec{r}-\vec{r}'|} + V^{\mathrm{xc}}[n(\vec{r},t)] \qquad (6.33)\\ \text{and} \qquad \vec{B}^{\mathrm{KS}}(\vec{r},t) =& \mu_B \left(\vec{B}^{\mathrm{ext}}(\vec{r}) + \delta\vec{B}(\vec{r},t)\right) + \vec{B}^{\mathrm{xc}}[n(\vec{r},t)] \quad . \qquad (6.34)\end{aligned}$$

An external electromagnetic perturbation effects the Kohn-Sham Hamiltonian in two ways: On the one hand there are the obvious dependencies of $\mathcal{H}^{\mathrm{KS}}$ on the external potentials. On the other hand the change in the densities influences the Hartree term and the exchange-correlation fields, which affects the total Hamiltonian. Both effects have to be considered up to first order in the perturbation.

The change in the Kohn-Sham Hamiltonian due to the change in the densities can be calculated as follows:

$$\begin{aligned} \delta\mathcal{H}^{\mathrm{KS}}(\vec{r},t) =& \mu_B \boldsymbol{\vec{\sigma}} \cdot \delta\vec{B}(\vec{r},t) + \delta V(\vec{r},t) \\ &+ \int \mathrm{d}\vec{r}'\mathrm{d}t' \; \big[\mathcal{K}^n(\vec{r},\vec{r}',t-t')\delta n(\vec{r}',t') \\ &\qquad + \mathcal{K}^m(\vec{r},\vec{r}',t-t') \cdot \delta\vec{m}(\vec{r}',t')\big] \quad , \end{aligned} \tag{6.35}$$

where we used the functional derivatives of the KS Hamiltonian with respect to the densities, which define the so-called kernels

$$\begin{aligned} \mathcal{K}^n(\vec{r},\vec{r}',t-t') =& \left.\frac{\delta\mathcal{H}^{\mathrm{KS}}}{\delta n(\vec{r}',t')}\right|_{n_0(\vec{r}),\vec{m}_0(\vec{r})}, \qquad (6.36)\\ \text{and} \qquad \mathcal{K}^m(\vec{r},\vec{r}',t-t') =& \left.\frac{\delta\mathcal{H}^{\mathrm{KS}}}{\delta\vec{m}(\vec{r}',t')}\right|_{n_0(\vec{r}),\vec{m}_0(\vec{r})} \quad . \qquad (6.37)\end{aligned}$$

In the adiabatic local density approximation the Kernels are time-independent and given by

$$\mathcal{K}^n(\vec{r},\vec{r}') = \underbrace{\frac{2}{|\vec{r}-\vec{r}'|}}_{\mathcal{K}_{\mathrm{H}}(\vec{r},\vec{r}')} + \delta(\vec{r}-\vec{r}') \underbrace{\left.\frac{\delta V^{\mathrm{xc}}(\vec{r})}{\delta n(\vec{r})}\right|_{n_0,\vec{m}_0}}_{\mathcal{K}^{nn}_{\mathrm{xc}}(\vec{r})} + \delta(\vec{r}-\vec{r}')\boldsymbol{\vec{\sigma}} \cdot \underbrace{\left.\frac{\delta\vec{B}^{\mathrm{xc}}(\vec{r})}{\delta n(\vec{r})}\right|_{n_0,\vec{m}_0}}_{\mathcal{K}^{mn}_{\mathrm{xc}}(\vec{r})}, \tag{6.38}$$

$$\text{and} \qquad \mathcal{K}^m(\vec{r}) = \underbrace{\left.\frac{\delta V^{\mathrm{xc}}(\vec{r})}{\delta\vec{m}(\vec{r})}\right|_{n_0,\vec{m}_0}}_{\mathcal{K}^{nm}_{\mathrm{xc}}(\vec{r})} + \boldsymbol{\vec{\sigma}} \cdot \underbrace{\left.\frac{\delta\vec{B}^{\mathrm{xc}}(\vec{r})}{\delta\vec{m}(\vec{r})}\right|_{n_0,\vec{m}_0}}_{\mathcal{K}^{mm}_{\mathrm{xc}}(\vec{r})} \quad . \tag{6.39}$$

The Hartree kernel $\mathcal{K}_H$ is non-local, whereas the exchange-correlation Kernels are all local due to the ALDA.

An elegant approach to calculate the change in the densities is the usage of the time-dependent Green function and the Dyson equation up to first order. It can be shown that the densities are given in terms of the time-ordered Green functions by [47]

$$n(\vec{r},t) = -i\mathrm{Tr}\; G(\vec{r},\vec{r};t,t^+) \qquad \text{and} \qquad \vec{m}(\vec{r},t) = -i\mathrm{Tr}\; \boldsymbol{\vec{\sigma}} G(\vec{r},\vec{r};t,t^+) \quad . \tag{6.40}$$

Via the Dyson equation the Green function can be expanded in the perturbation:

$$G(\vec{r},\vec{r}';t-t') = G_0(\vec{r},\vec{r}';t-t') + \delta G(\vec{r},\vec{r}';t-t') \tag{6.41}$$

$$\text{with} \quad \delta G(\vec{r},\vec{r}';t-t') = \int \mathrm{d}\vec{r}''\mathrm{d}t''\; G_0(\vec{r},\vec{r}'';t-t'')\delta\mathcal{H}^{\mathrm{KS}}(\vec{r}'',t'')G_0(\vec{r}'',\vec{r}';t''-t') \quad , \tag{6.42}$$

where $G_0(\vec{r},\vec{r}';t-t')$ is the time-dependent Green function of the unperturbed system. In the following, the integrals and the dependencies on $\vec{r}$ and t are skipped to simplify the notations. The change in the charge density is given by

$$\begin{aligned}
\delta n(\vec{r},t) &= -i\mathrm{Tr}\;\delta G(\vec{r},\vec{r};t,t^+) && (6.43)\\
&= -i\int \mathrm{d}\vec{r}'\mathrm{d}t'\;\mathrm{Tr}\;\left[G_0(\vec{r},\vec{r}';t-t')\delta\mathcal{H}^{\mathrm{KS}}(\vec{r}',t')G_0(\vec{r}',\vec{r};t'-t^+)\right] && (6.44)\\
&= -i\int \mathrm{d}\vec{r}'\mathrm{d}t'\;\mathrm{Tr}\;\Big[G_0(\vec{r},\vec{r}';t-t')G_0(\vec{r}',\vec{r};t'-t^+)\delta V^{\mathrm{KS}}(\vec{r}',t') \\
&\qquad + G_0(\vec{r},\vec{r}';t-t')\boldsymbol{\sigma}^b G_0(\vec{r}',\vec{r};t'-t^+)\delta B^{b,\mathrm{KS}}(\vec{r}',t')\Big] \quad , && (6.45)
\end{aligned}$$

where the kernel contribution is omitted. Via eq. (6.45) the so-called Kohn-Sham susceptibilities χ_0, which describe the response of the Kohn-Sham system without taking the density changes in the Hamiltonian into account, can be defined

$$\chi_0^{ab}(\vec{r},\vec{r}';t-t') = -i\mathrm{Tr}\;\left[\boldsymbol{\sigma}^a G_0(\vec{r},\vec{r}';t-t')\boldsymbol{\sigma}^b G_0(\vec{r}',\vec{r};t'-t)\right] \quad , \tag{6.46}$$

with $a,b=\{x,y,z,n\}$ and the index n indicates the unity matrix $\boldsymbol{\sigma}^0$. Omitting the integrals and the dependences on the space and time coordinates the susceptibilities of the interacting system χ^{ab}, which are called renormalized susceptibilities, have to fulfil the following Dyson-like equation

$$\chi^{ab} = \chi_0^{ab} + \chi_0^{an}\mathcal{K}_{\mathrm{H}}\chi^{nb} + \sum_{cd}\chi_0^{ac}\mathcal{K}_{\mathrm{xc}}^{cd}\chi^{db} \quad , \tag{6.47}$$

which can be solved, e.g. by inversion.
At this point, we can discuss the role of the Hartree kernel. The Hartree kernel, which is non-local and therefore numerically cumbersome, couples to the density components of the susceptibility. It describes the Coulomb interaction of an charge element with the surrounding disturbed charge distribution. Without spin-orbit coupling the longitudinal and the transversal susceptibilities are fully decoupled. This means if we only consider the transversal susceptibilities without spin-orbit coupling the Hartree kernel is not used.

Calculations are done in the frequency space. One can show, that the Fourier transform of eq. (6.46) is equivalent to the correlation function showed in eq. (6.21), which uses the retarted Green function and its imaginary part, evaluated with the Pauli matrices as operators.
In the KKR codes, we work in the frequency space and evalute the Kohn-Sham susceptibilities via eq. (6.21), which is discussed in the next section.

6.2.2. Susceptibilities within the KKR formalism

In section 4.3 the actual representation of the Green function within the projection scheme is shown. The basis, which is called Green function basis in the following, consists of a few energy independent radial basis functions and the spherical harmonics. Using this basis the susceptibility can be written as

$$\chi^{ab}(\vec{r},\vec{r}';\omega) = \sum_{L_1b_1\dots L_4b_4} Y_{L_1}(\hat{r})Y_{L_2}(\hat{r})\phi_{nl_1b_1}(r)\phi_{nl_2b_2}(r)\chi^{ab}_{nn';L_1b_1L_2b_2;L_3b_3L_4b_4}(\omega) \\ \times \phi_{n'l_3b_3}(r')\phi_{n'l_4b_4}(r')Y_{L_3}(\hat{r}')Y_{L_4}(\hat{r}') \quad , \tag{6.48}$$

with the matrix element $\chi^{ab}_{nn';L_1b_1L_2b_2;L_3b_3L_4b_4}(\omega)$ being of similar shape as eq. (6.21), but using the Green function matrix elements instead of the full Green function. However, this product basis for the susceptibility is huge, which makes it computationally demanding. The typical basis size for an angular momentum cutoff of $l = 3$ is $N = \left[(l+1)^2 \times \#b \times \#\text{atoms}\right]^2 = 1024 \times \#\text{atoms}^2$. For example, the renormalization of the susceptibility uses an inversion process, which has a cubic scaling $\mathcal{O}(N^3)$. Therefore, it is computationally advisable to reduce the basis size if possible.
Via a contraction of the two spherical harmonics used in the basis, it is possible to simplify the basis. In the KKRsusc code a new orthonormal basis set is used, which typically reduces the basis size by a factor of approximately 4. The Green function basis is mapped on the new basis, which is called in the following density basis, via

$$\phi_{nl_1b_1}(r)\phi_{nl_2b_2}(r)Y_{L_1}(\hat{r})Y_{L_2}(\hat{r}) = \sum_{Lb} C^{Lb}_{L_1b_1L_2b_2}\Phi_{Lb}(r)Y_L(\hat{r}) \quad , \tag{6.49}$$

with the coefficients

$$C^{Lb}_{L_1b_1L_2b_2} = \int \mathrm{d}r\; r^2\phi_{nl_1b_1}(r)\phi_{nl_2b_2}(r)\Phi_{Lb}(r)\underbrace{\int \mathrm{d}\hat{r}\; Y_{L_1}(\hat{r})Y_{L_2}(\hat{r})Y_L(\hat{r})}_{=C^L_{L_1L_2}} \quad , \tag{6.50}$$

which leads to the representation of the susceptibility in the density basis:

$$\chi^{ab}(\vec{r},\vec{r}';\omega) = \sum_{Lb,L'b'} Y_L(\hat{r})\Phi_{nLb}(r)\chi^{ab}_{nn';LbL'b'}(\omega)\Phi_{n'L'b'}(r')Y_{L'}(\hat{r}') \quad . \tag{6.51}$$

Also the Hartree and the exchange-correlation kernel are given in the density basis within the code. Since the basis is orthonormal the evaluation of eq. (6.47) is simply a matrix multiplication and inversion of the corresponding matrix elements.

In addition to the spatial dependence the frequency dependence has to be discussed. The Kohn-Sham susceptibility is calculated by using the Taylor expansion in frequency space given in eq. (6.23). This is a good approximation since the energy scale in which we are interested is characterized by the collective spin precession, which are much lower in energy than the Stoner excitations. Therefore, for the range of frequencies we are interested in, the Kohn-Sham susceptibility is a smooth function.

6.3. Spin-currents within linear response and TDDFT

In this section, the main result of this chaper is discussed – the response of the spin and charge currents to an external perturbation $\delta\underline{V}$. We follow the same steps as the previous section and we will notice the very close connection between magnetic excitations and currents.
The paramagnetic spin and charge current operators are given by

$$\hat{j}^a_k(\vec{r}) = -i\mu_B \lim_{\vec{r}'\to\vec{r}} \left(\partial_k - \partial'_k\right)\boldsymbol{\sigma}^a \quad , \tag{6.52}$$

which leads via the Kubo formula to the charge and spin current response to an external perturbation:

$$\begin{aligned}\delta\Big\langle\hat{j}^a_k(\vec{r},t)\Big\rangle &= -\,i\int \mathrm{d}^3r'\mathrm{d}t'\ \Theta(t-t')\Big\langle\Big[\hat{j}^a_k(\vec{r},t),\boldsymbol{\sigma}^b\Big]\Big\rangle\cdot\delta\underline{V}^b(\vec{r}',t') &(6.53)\\ &=\int \mathrm{d}^3r'\mathrm{d}t'\ \chi^{ab}_{j_km}(\vec{r},\vec{r}',t-t')\delta\underline{V}^b(\vec{r}',t') \quad , &(6.54)\end{aligned}$$

with the spin-current–spin correlation function $\chi^{ab}_{j_km}$. The index a refers to the spin polarization of the current, whereas the index b is the direction of the external field ($a,b=\{x,y,z,0\}$). In addition, the index k refers to the flow direction of the current.

According to eq. (6.21) the spin-current–spin correlation function of the Kohn-Sham system can be calculated via

$$\begin{aligned}&\chi^{ab}_{j_km}(\vec{r},\vec{r}';\omega+i\eta)=\\ &i\mu_B\lim_{\vec{r}''\to\vec{r}}\Bigg\{\frac{1}{\pi}\int\mathrm{d}E\ f(E)\ \mathrm{Tr}\ \Big[\left(\partial_k-\partial''_k\right)\boldsymbol{\sigma}^a G_0(\vec{r},\vec{r}';\omega+E+i\eta)\boldsymbol{\sigma}^b\ \mathrm{Im}\ G_0(\vec{r}',\vec{r}'';E+i0^+)\Big]\\ &\qquad+\frac{1}{\pi}\int\mathrm{d}E\ f(E)\ \mathrm{Tr}\ \Big[\left(\partial_k-\partial''_k\right)\boldsymbol{\sigma}^a\ \mathrm{Im}\ G_0(\vec{r},\vec{r}';E+i0^+)\boldsymbol{\sigma}^b G_0(\vec{r}',\vec{r}'';-\omega+E-i\eta)\Big]\Bigg\} \quad . \qquad (6.55)\end{aligned}$$

At this point, the close connection between the spin-spin susceptibility and the spin-current–spin correlation function is visible.

Let us analyse the structure a bit further within the Green function basis of the KKRsusc code. From eq. (6.55) it is easy to see, that the spin-current–spin correlation function can be written in terms of the spin-spin susceptibility as:

$$\begin{aligned}\chi^{ab}_{j_km}(\vec{r},\vec{r}';\omega)=-i\mu_B\lim_{\vec{r}''\to\vec{r}}\left(\partial_k-\partial''_k\right)&\sum_{L_1b_1\ldots L_4b_4}Y_{L_1}(\hat{r}'')\phi_{nl_1b_1}(r'')Y_{L_2}(\hat{r})\phi_{nl_2b_2}(r)\\ &\times\chi^{ab}_{nn';L_1b_1L_2b_2;L_3b_3L_4b_4}(\omega)\phi_{n'l_3b_3}(r')\phi_{n'l_4b_4}(r')Y_{L_3}(\hat{r}')Y_{L_4}(\hat{r}') \quad . \qquad (6.56)\end{aligned}$$

Using a similar approach as for the groundstate currents, we can construct a basis with one gradient to define the spin-current–spin correlation function by relabeling the summation indices:

$$\begin{aligned}\chi^{ab}_{j_km}(\vec{r},\vec{r}';\omega)=&\sum_{L_1b_1\ldots L_4b_4}\partial_k\left(Y_{L_1}(\hat{r})\phi_{nl_1b_1}(r)\right)Y_{L_2}(\hat{r})\phi_{nl_2b_2}(r)\\ &\times\chi^{ab}_{j_km;nn';L_1b_1L_2b_2;L_3b_3L_4b_4}(\omega)\phi_{n'l_3b_3}(r')\phi_{n'l_4b_4}(r')Y_{L_3}(\hat{r}')Y_{L_4}(\hat{r}') \quad , \qquad (6.57)\end{aligned}$$

with the spin-current–spin correlation function matrix element

$$\chi^{ab}_{j_km;nn';L_1b_1L_2b_2;L_3b_3L_4b_4}(\omega)=i\mu_B\left(\chi^{ab}_{nn';L_1b_1L_2b_2;L_3b_3L_4b_4}(\omega)-\chi^{ab}_{nn';L_2b_2L_1b_1;L_3b_3L_4b_4}(\omega)\right) \quad . \qquad (6.58)$$

Since we are using this gradient basis it is not possible to switch to the density basis, which is used for the magnetic susceptibility. The basis functions of the density basis are constructed to fit the Green function product basis and not the gradients of it. However, we will see that it is convenient to switch to the density basis for the $\vec{r}'$ dependence, which yields

$$\chi^{ab}_{j_km}(\vec{r},\vec{r}';\omega)=\sum_{\substack{L_1b_1L_2b_2\\ Lb}}\partial_k\left(Y_{L_1}(\hat{r})\phi_{nl_1b_1}(r)\right)Y_{L_2}(\hat{r})\phi_{nl_2b_2}(r)\chi^{ab}_{j_km;nn';L_1b_1L_2b_2;Lb}(\omega)\Phi_{n'Lb}(r')Y_L(\hat{r}') \quad , \qquad (6.59)$$

with the matrix elements

$$\chi^{ab}_{j_km;nn';L_1b_1L_2b_2;Lb}(\omega)=\sum_{L_3b_3L_4b_4}\chi^{ab}_{j_km;nn';L_1b_1L_2b_2;L_3b_3L_4b_4}(\omega)C^{Lb}_{L_3b_3L_4b_4} \quad . \qquad (6.60)$$

6.3.1. Renormalized spin-current–spin correlation function

To take the interaction effects in to account, the convenient starting point are time-dependent Green functions. The currents can be written in terms of the time-ordered Green function as:

$$\delta j_k^a(\vec{r},t) = -\mu_B \lim_{\vec{r}'\to\vec{r}} \mathrm{Tr}\ \boldsymbol{\sigma}^a \left(\partial_k - \partial_k'\right) \delta G(\vec{r},\vec{r}',t,t^+) \quad , \tag{6.61}$$

with δG from eq. (6.42), which was discussed in detail in section 6.2.1. Comparing to the structure of the magnetic susceptibility, one can see that the only difference are the additional gradients. The gradients act on the coordinates of the unperturbed Green functions, which are used to define the Kohn-Sham susceptibilities. Thus in total, the calculation is similar to the magnetic susceptibility, but with gradients acting on the Kohn-Sham susceptibilities.

Defining the Kohn-Sham spin-current–spin correlation function as

$$\chi^{ab}_{0;j_k m}(\vec{r},\vec{r}';t-t') = -\mu_B \lim_{\vec{r}''\to\vec{r}} \left(\partial_k - \partial_k''\right) \mathrm{Tr}\ \left[\boldsymbol{\sigma}^a G_0(\vec{r},\vec{r}';t-t')\boldsymbol{\sigma}^b G_0(\vec{r}',\vec{r}'';t'-t)\right] \quad , \tag{6.62}$$

yields for the renormalized correlation function

$$\chi^{ab}_{j_k m} = \chi^{ab}_{0;j_k m} + \chi^{an}_{0;j_k m}\mathcal{K}_{\mathrm{H}}\chi^{nb} + \sum_{cd} \chi^{ac}_{0;j_k m}\mathcal{K}^{cd}_{\mathrm{xc}}\chi^{db} \quad , \tag{6.63}$$

where χ^{ab} are the renormalized magnetic susceptibilities. Thus knowing the kernels and the renormalized magnetic susceptibilites is sufficient to renormalize the spin-current–spin correlation function.

Computational details

To implement the renormalized spin-current–spin correlation function the mixed basis set discussed in the previous section is used. The $\vec{r}$ dependence of the correlation function is treated in the gradient Green function basis, whereas the $\vec{r}'$ dependence is treated in the density basis. Due to the orthonormality of the density basis the evaluation of eq. (6.63) simplifies to a matrix multiplication. Defining $\mathcal{N}_{\mathrm{den}}$ as the number of basis elements in the density basis and $\mathcal{N}_{\mathrm{GF}}$ as the number of basis elements in the Green function basis, the matrix multiplication is of order $\mathcal{O}(\mathcal{N}_{\mathrm{GF}} \times \mathcal{N}^2_{\mathrm{den}})$. Thus the operation is linear in the size of the Green function basis. Therefore, the speed up by decreasing the basis size would be approximately a factor of 4, which is the difference between density and Green function basis. Therefore at the moment it is not worth the effort to set up a new smaller basis for the gradient Green function basis.

6.3.2. Structure of the spin-current–spin correlation function

In this section the structure of the spin-current–spin correlation function is discussed. For systems with spin-orbit coupling, all 16 elements of the magnetic susceptibility and the spin-current–spin correlation function can be finite. However, for collinear systems without spin-orbit coupling both quantities are block diagonal as shown in eq. (6.31), such that the transversal part and the longitudinal part decouple.

In the static limit the structure simplifies even more. Let us discuss the transversal block in more detail. Eq. (6.24) yields the following condition for vanishing elements:

$$\mathrm{Tr}\ \left[\hat{A}G(\vec{r},\vec{r}';E+i0^+)\hat{B}G(\vec{r}',\vec{r};E+i0^+)\right] \overset{!}{=} 0 \quad . \tag{6.64}$$

In the considered case, the Green functions are diagonal and symmetric

$$G(\vec{r},\vec{r}';E+i0^+) = \begin{pmatrix} G^{\uparrow}(\vec{r},\vec{r}';E+i0^+) & 0 \\ 0 & G^{\downarrow}(\vec{r},\vec{r}';E+i0^+) \end{pmatrix} = G(\vec{r}',\vec{r};E+i0^+) \quad , \tag{6.65}$$

which yields for the susceptibility

$$\chi^{ab} \propto 2\begin{cases} G^{\downarrow}(\vec{r},\vec{r}';E+i0^+)G^{\uparrow}(\vec{r}',\vec{r};E+i0^+), & \text{for} \quad ab=\{xx,yy\} \\ 0, & \text{for} \quad ab=\{xy,yx\} \end{cases} \quad , \tag{6.66}$$

such that only the xx and yy-components are finite.
A similar procedure can be done for the spin-current–spin correlation function. The important quantity is

$$\lim_{\vec{r}''\to\vec{r}} \mathrm{Tr}\ \left[\left(\vec{\nabla}-\vec{\nabla}''\right)\boldsymbol{\sigma}^a G(\vec{r},\vec{r}';E+i0^+)\boldsymbol{\sigma}^b G(\vec{r}',\vec{r}'';E+i0^+)\right] \quad , \tag{6.67}$$

which yields due to the additional subtraction with the gradients other possible finite components:

$$\begin{aligned} \chi^{ab}_{jm} \propto & \left(\vec{\nabla}G^{\downarrow}(\vec{r},\vec{r}';E+i0^+)\right)G^{\uparrow}(\vec{r}',\vec{r};E+i0^+) \\ & -\left(\vec{\nabla}G^{\uparrow}(\vec{r},\vec{r}';E+i0^+)\right)G^{\downarrow}(\vec{r}',\vec{r};E+i0^+) \end{aligned}, \qquad \text{for} \quad ab=\{xy,yx\} \quad . \tag{6.68}$$

Thus the static spin-current–spin correlation function can mathematically be non-zero for the xy and the yx-component.

6.4. Model for the excitations within linear response

In this section, a model to describe excitations within linear response is discussed. The Anderson-like model in section 5.2.1, which was used to describe ground state charge currents, can not directly be used to calculate the susceptibilities. However, with a few extensions it is possible to use the model. The main change is the explicit inclusion of the spin, which is done by using a Stoner-like spin splitting described by the parameter U. Furthermore, the spin dependence is added to the spin-orbit coupling term, which is treated purely in the z-direction. To simplify the problem, we stick to the use of the $(l,m)=(2,\pm 2)$ orbitals, which give the leading order contribution with SOC. Furhtermore, the orbitals are of Slater type yielding a simple radial dependence, such that the orbitals are given by

$$\phi_\mu(\vec{r}) = R(r)Y_2^\mu(\hat{r}), \quad \text{with} \quad R(r) = Ar^2e^{-\alpha r} \quad , \tag{6.69}$$

where Y_2^μ are *complex* spherical harmonics, A is a normalization constant and α defines a characteristic length scale of the problem.
The effective Hamiltonian is given by

$$\mathcal{H}^{\text{eff}}_{\mu\mu';ss'} = (E_d - i\Gamma)\,\delta_{\mu\mu'}\sigma^0_{ss'} - \frac{U}{2}m\delta_{\mu\mu'}\sigma^z_{ss'} + \xi L^z_{\mu\mu'}\sigma^z_{ss'} \quad , \tag{6.70}$$

where the index μ refers to the orbitals, s refers to the spins and m is the magnetization, which is assumed to be a parameter and not calculated self-consistently as a first approximation.
The Green function of this Hamiltonian can be written in the eigenbasis as

$$G(E) = \left(E - H^{\mathrm{eff}}\right)^{-1} = \sum_{\mu,s} \frac{|\mu,s\rangle\langle\mu,s|}{E - E_{\mu,s} + i\Gamma} \tag{6.71}$$

$$\Rightarrow \qquad G(\vec{r},\vec{r}\,';E) = \sum_{\mu,s} R(r) Y_2^{\mu}(\hat{r}) \underbrace{G_{\mu s;\mu s}(E)}_{\langle\mu,s|G(E)|\mu,s\rangle} \left[Y_2^{\mu}(\hat{r}')\right]^* R(r') \quad , \tag{6.72}$$

with the eigenenergies

$$E_{\mu,s} = E_d - i\Gamma - \frac{U}{2} m\sigma^z_{ss} + \xi\mu\sigma^z_{ss} \quad . \tag{6.73}$$

Using eq. (6.21) the correlation function of any two observables for this model Hamiltonian can be calculated. A detailed derivation is given in Appendix D, where it is shown that the correlation function can be written as

$$\chi_{AB}(\omega) = \sum_{\mu s,\mu' s'} \mathrm{Tr}\left[\hat{A}|\mu s\rangle\langle\mu s|\hat{B}|\mu' s'\rangle\langle\mu' s'|\right] \tilde{\chi}_{\mu s,\mu' s'}(\omega) \tag{6.74}$$

$$= \sum_{\mu s,\mu' s'} \left[\langle\mu' s'|\hat{A}|\mu s\rangle\langle\mu s|\hat{B}|\mu' s'\rangle\right] \tilde{\chi}_{\mu s,\mu' s'}(\omega) \quad , \tag{6.75}$$

or equivalently in the spatial representation:

$$\chi_{AB}(\vec{r},\vec{r}\,';\omega) = \sum_{\mu s,\mu' s'} \left[\phi^*_{\mu'}(\vec{r})\langle s'|\hat{A}|s\rangle\phi_{\mu}(\vec{r})\phi^*_{\mu}(\vec{r}\,')\langle s|\hat{B}|s'\rangle\phi_{\mu'}(\vec{r}\,')\right] \tilde{\chi}_{\mu s,\mu' s'}(\omega) \quad . \tag{6.76}$$

Magnetic susceptibility

In the case of the magnetic susceptibility the operators $\hat{A}$ and $\hat{B}$ are given by Pauli matrices. To see which elements contribute we have a look at the spin-dependent part

$$\langle s'|\sigma^A|s\rangle\langle s|\sigma^B|s'\rangle \quad , \tag{6.77}$$

which is only non-zero for specific Pauli matrices. One can show that the combinations

$$AB = \{+-,-+,\uparrow\uparrow,\downarrow\downarrow\}, \quad \text{with} \quad \sigma^+ = |\uparrow\rangle\langle\downarrow|, \quad \sigma^- = |\downarrow\rangle\langle\uparrow|, \quad \sigma^\uparrow = |\uparrow\rangle\langle\uparrow|, \quad \sigma^\downarrow = |\downarrow\rangle\langle\downarrow| \quad , \tag{6.78}$$

and thus only 4 of 16 possible components of the susceptibility are finite.

Furthermore, we can analyse the spatial dependence of the magnetization for a homogeneous magnetic field. The integral over $\vec{r}\,'$ in eq. (6.27) yields for a homogeneous perturbation the condition $\delta_{\mu\mu'}$ due to the orthonormality of the orbitals. The resulting spatial distribution of the magnetization has the form

$$R(r)^2 Y_2^2(\hat{r}) Y_2^{-2}(\hat{r}) = R(r)^2 \frac{1}{\sqrt{\pi}} \left[\frac{1}{2} Y_0^0(\hat{r}) - \frac{\sqrt{5}}{7} Y_2^0(\hat{r}) + \frac{1}{14} Y_4^0(\hat{r})\right] \quad . \tag{6.79}$$

Spin-current–spin correlation function

The spin-current–spin correlation function differs from the susceptibility by the additional gradients. For a homogeneous perturbation it is given by:

$$\chi^{ab}_{jkm}(\vec{r}, \vec{r}'; \omega) = \sum_{\mu;s,s'} \left[\left\{ \phi^*_\mu(\vec{r}) \partial_k \left(\phi_\mu(\vec{r}) \right) - \phi_\mu(\vec{r}) \partial_k \left(\phi^*_\mu(\vec{r}) \right) \right\} \langle s' | \boldsymbol{\sigma}^a | s \rangle \langle s | \boldsymbol{\sigma}^b | s' \rangle \right] \tilde{\chi}_{\mu s, \mu s'}(\omega) \quad . \tag{6.80}$$

The evaluation of the spin-dependent part is identical to the magnetic susceptibilities, which yields the same structure as described in eq. (6.78). However, the gradients affect the spatial dependence. Using the relation

$$\left(Y^m_l(\hat{r}) \right)^* = (-1)^m Y^{-m}_l(\hat{r}) \qquad \Rightarrow \qquad \left(Y^2_2(\hat{r}) \right)^* = Y^{-2}_2(\hat{r}) \quad , \tag{6.81}$$

yields for the spatial dependent part of eq. (6.80)

$$\begin{aligned} & R(r) Y^{-\mu}_2(\hat{r}) \partial_k \left[R(r) Y^\mu_2(\hat{r}) \right] - R(r) Y^\mu_2(\hat{r}) \partial_k \left[R(r) Y^{-\mu}_2(\hat{r}) \right] \\ &= R(r)^2 \left\{ Y^{-\mu}_2(\hat{r}) \left[\partial_k Y^\mu_2(\hat{r}) \right] - Y^\mu_2(\hat{r}) \left[\partial_k Y^{-\mu}_2(\hat{r}) \right] \right\} \quad . \end{aligned} \tag{6.82}$$

Plugging in the actual form of the spherical harmonics yields

$$Y^{-\mu}_2(\hat{r}) \left[\partial_k Y^\mu_2(\hat{r}) \right] - Y^\mu_2(\hat{r}) \left[\partial_k Y^{-\mu}_2(\hat{r}) \right] = \mathrm{sgn}(\mu)\; i \sqrt{\frac{3}{\pi}} \frac{1}{r} \begin{cases} -Y_{1,-1} + \frac{1}{\sqrt{14}} Y_{3,-1}, & k = x \\ Y_{1,1} - \frac{1}{\sqrt{14}} Y_{3,1}, & k = y \end{cases} \quad , \tag{6.83}$$

which is a purely swirling field in the x-y–plane.

At this point, a few drawbacks of the model are noticeable. The chosen orbitals may be the most relevant for the spin-orbit coupling part, but the spatial dependence of these orbitals will always lead to a swirling in the x-y–plane as we already saw for the ground state charge current model in section 5.2.1.

Thus we expect this model to describe at most the effects resulting from spin-orbit coupling. However, we already saw for ground state currents that external magnetic fields can lead to finite spin-currents, which is exactly the situation in the linear response calculations. Thus if we consider systems without spin-orbit coupling, we can not expect results which are swirling, since the argument of chosing the specific orbitals is based on spin-orbit coupling.

6.5. Landau-Lifshitz-Gilbert equation

Magnetization dynamics in ferromagnets are often described by the Landau-Lifschitz-Gilbert (LLG) model, which is a phenomenological approach. The basic equation describing the dynamics of a magnetic moment is given by

$$\frac{\mathrm{d}\vec{m}}{\mathrm{d}t} = -\gamma\, \vec{m} \times \vec{B} + \eta \frac{\vec{m}}{m} \times \frac{\mathrm{d}\vec{m}}{\mathrm{d}t} \quad , \tag{6.84}$$

where $\gamma = g\mu_B$ is the gyromagnetic ratio and η is an empirical damping parameter. The g-factor equals 2 for free electrons, whereas for more complex systems it can slightly differ from 2 due to the electronic structure close to the Fermi level and to the presence of an orbital magnetic moment.

For a constant magnetic field the LLG equation describes a precession of the magnetic moment

around the field vector with the precession frequency γB. If damping is turned on ($\eta > 0$) the precession spirals down so that the magnetic moment aligns with the magnetic field.
The LLG equation can be connected to the magnetic susceptibility as follows: Assume a small time-dependent magnetic perturbation, which induces a change in the magnetic moment. The dynamics of the magnetic moment can be described by the magnetic susceptibility. Writing the LLG equation in the frequency space up to first order in the perturbation yields

$$-i\omega\delta\vec{m} = -\gamma\left(\delta\vec{m}\times\vec{B}_0 + \vec{m}\times\delta\vec{B}\right) - i\omega\eta\hat{e}_z\times\delta\vec{m} \quad , \tag{6.85}$$

with the magnetic moment $\delta m^a = \chi^{ab}\delta B^b$. In general, eq. (6.85) describes a set of coupled equations, which can be solved for the elements of the susceptibility. Assuming a homogeneous external field, it can be shown that the transverse magnetic susceptibility in the LLG model is given by [37]

$$\chi^{+-} = \frac{1}{4}\left[\chi^{xx} + \chi^{yy} + i\chi^{xy} - i\chi^{yx}\right] \tag{6.86}$$

$$= \frac{m^z\omega_0}{2B_0}\frac{(1+\eta^2)\omega_0 - \omega + i\eta\omega}{(\omega-\omega_0)^2 + (\eta\omega_0)^2}, \quad \text{with} \quad \omega_0 = \frac{\gamma B_0}{1+\eta^2} \quad . \tag{6.87}$$

Thus by fitting the KKR results to the LLG model function the KKR susceptibility gives access to the gyromagnetic ratio and the damping parameter.

6.5.1. Spin pumping theory

Spin currents and magnetization dynamics are closely connected in two ways: On the one hand, an applied spin current can induce magnetization dynamics, e.g. domain wall motion. On the other hand, magnetization dynamics can induce spin currents, which gives rise to the spin pumping method. Spin pumping is a method for the generation of spin-current, which is of huge interest in the field of spintronics. Tserkovnyak *et al.* [5] showed the connection between dynamical magnetization motion and the pumped spin current in a layered system consisting of a ferromagnetic layer in between two normal metal layers. Using the LLG model to describe the magnetization dynamics, the pumped spin current can be connected to the LLG parameters. The divergence of the pumped spin current with polarization a is given by

$$I^a_{\text{pump}} = \left[A_r\left(\vec{m}\times\frac{\mathrm{d}\vec{m}}{\mathrm{d}t}\right)^a - A_i\frac{\mathrm{d}m^a}{\mathrm{d}t}\right] \quad , \tag{6.88}$$

where A_i and A_r are parameters depending on the reflection and transmission coefficients of the interface for electrons. It is shown by Tserkovnyak, that the interface parameters are connected to the renormalization of the LLG parameters

$$\frac{1}{\gamma} = \frac{1}{\gamma_0}\left[1 + g_L\frac{A_i^{(L)} + A_i^{(R)}}{M}\right] \tag{6.89}$$

$$\eta = \frac{\gamma}{\gamma_0}\left[\eta_0 + g_L\frac{A_r^{(L)} + A_r^{(R)}}{M}\right] \quad , \tag{6.90}$$

where g_L is the Landé factor, M is the total magnetic moment, the subscript 0 indicates the bulk values and the superscripts (L) and (R) the evaluation of the interface parameters at the left and right side of the ferromagnetic layer.

In principle, we can obtain the interface parameter from the KKR simulation via the renormalized LLG parameters. However, in this work we are not dealing with layered systems. Therefore, the model by Tserkovnyak is not directly applicable to our simulation results, but can be used as a approximation without defining the parameters A_i and A_r in more detail.
Within the model of Tserkovnyak, the pumped spin current can be written in terms of the susceptibility by Fourier transforming and linearizing eq. (6.88), which yields

$$I^a_{\text{pump}} = -\frac{\hbar}{4\pi} i\omega \left[A_r \left(\vec{m}_0 \times \delta\vec{m}\right)^a - A_i \delta m^a\right] \quad , \tag{6.91}$$

with $\delta m^a = \chi^{ab}\delta B^b$ and $\vec{m}_0 = m_0 \hat{e}_z$.
An important result is the $\omega = 0$ - limit , where the pumped spin-current should vanish since it is linear in the frequency. In the next chapter we will discuss this limit in more detail.

7. Spin-current excitations in magnetic adatoms

In this chapter the results of the spin-current calculations within linear response are discussed. The KKR procedure for linear response calculations, which was discussed in the previous chapter, is applied to an iron adatom on top of a Pt(111) surface. We restrict ourselves to transversal homogeneous and time-dependent magnetic fields perturbing a static magnetic field, which always points in the z-direction and acts locally on the adatom.

The chapter is structured as follows: In the first part, the dynamical spin-current and magnetization response to an external magnetic field is discussed. The dynamical spin-current–spin density correlation function is analysed as function of frequency. Using the continuity equation and the spin-pumping theory of Tserkovnyak, the spin-current–spin density correlation function is connected to the magnetic susceptibility. In the second part of this chapter, we have a detailed look at the $\omega = 0$ limit of the spin-current–spin density correlation function. In the final part of this chapter, we include spin-orbit-coupling effects, which lead to a more complex spin-current response.

7.1. Dynamical spin-current–spin correlation function

In this section the response to a dynamical homogeneous magnetic field is presented. We consider an iron adatom deposited on a Pt(111) surface with an external static out-of-plane magnetic field of 10 T (0.5788 meV), for which a standard self-consistent ground state DFT calculation is performed. The frequency dependence of the spin-current–spin density correlation function and of the magnetic susceptibility are discussed. Using an unidirectional monochromatic magnetic field perturbation, the resulting magnetization dynamics and the induced spin-currents are discussed. Furthermore, the continuity equation and the spin-pumping theory of Tserkovnyak are used to interpret the results.

Frequency dependence of the response functions

Figure 7.1 shows the renormalized spin-current–spin correlation function (a) and the renormalized magnetic susceptibility (b) as function of the frequency. All elements of the transverse response are shown, separating real and imaginary parts.

Let us first discuss the frequency dependence of the magnetic susceptibility. A characteristic important frequency is the resonance frequency $\omega_0 = gB_{\text{ext}}$, at which the highest density of magnetic excitations is found. As shown in section 6.5, the g-factor can be related to the LLG parameters

$$g = \frac{\gamma}{1+\eta^2} \quad , \tag{7.1}$$

where γ is the gyromagnetic ratio and η is the damping parameter. In a free system there is no damping, so that the g-factor and γ are equal 2. Fitting the linearized LLG equation to the our

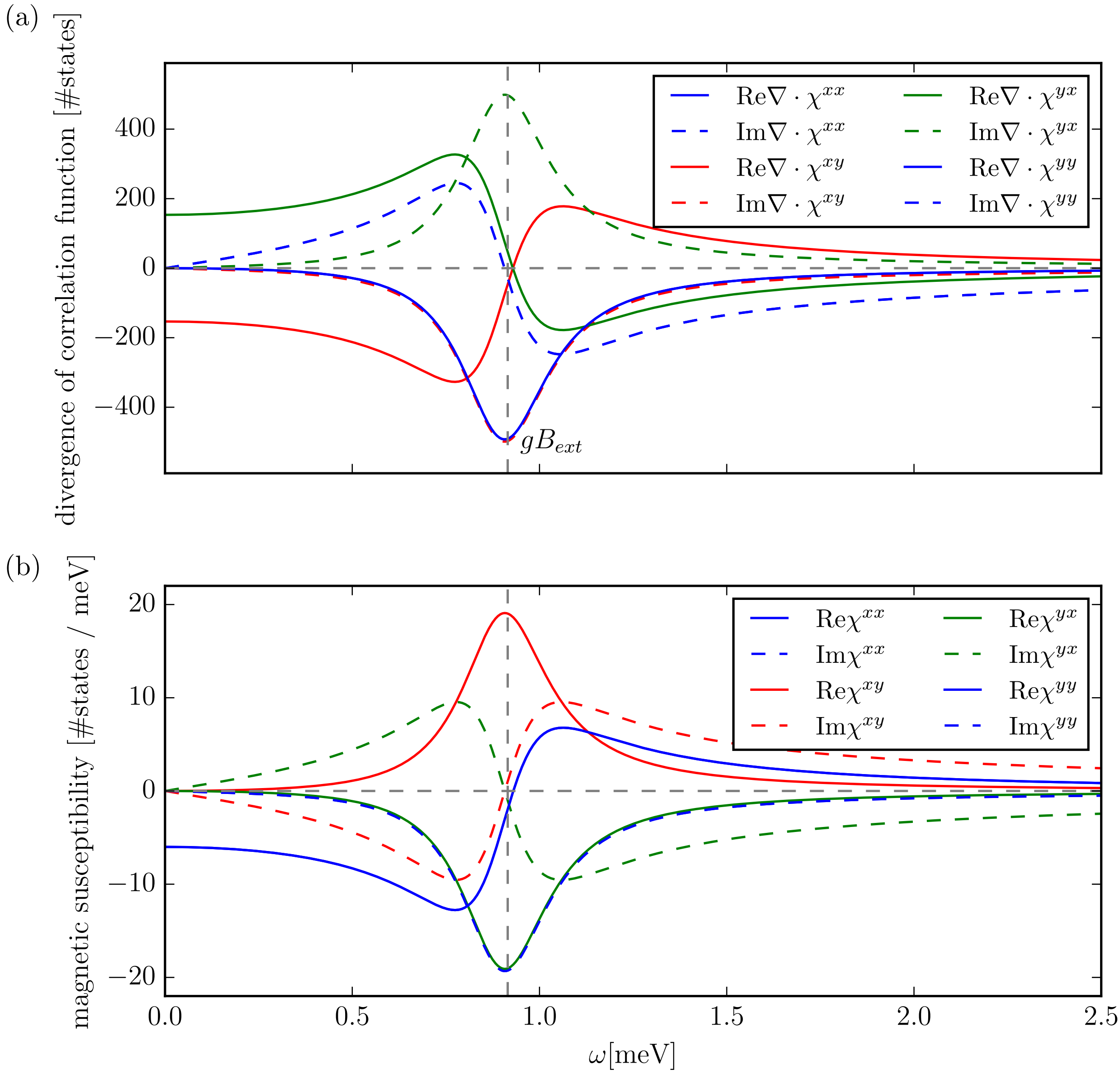

Figure 7.1.: (a) Divergence of the spin-current–spin correlation function of an iron adatom on top of Pt(111) as function of frequency, averaged over the atomic sphere. (b) Magnetic susceptibility as function of frequency, averaged over the atomic sphere.

results yields the values

$$\gamma = 1.581 \quad \text{and} \quad \eta = 0.159 \quad , \tag{7.2}$$

so that γ and g differ by more than 20% from the values of a free system. The reason for this is that the magnetic adatom is strongly coupled to the Pt(111) surface. For the response of the full system, one would find the values of 2 for both quantities. Locally in the adatom, the damping and the deviation of γ from 2 is induced by an emission of spin currents. In order to understand this effect (and many more) in more detail, an in-depth investigation of dynamical induced spin-currents from first-principles is important.

Let us continue with the spin-current–spin density correlation function shown in figure 7.1(a). The frequency dependence of the spin-current–spin density correlation function is quite similar to the frequency dependence of the magnetic susceptibility, which can be seen from the definition of the renormalized spin-current–spin density correlation function:

$$\chi_{jm}^{ab} = \chi_{0,jm}^{ab} + \sum_{cd} \chi_{0,jm}^{ac} \mathcal{K}_{\mathrm{xc}}^{cd} \chi_{mm}^{db} \quad . \tag{7.3}$$

In the considered frequency range, the Kohn-Sham correlation function $\boldsymbol{\chi}_{0,jm}$ depends only weakly on the frequency, while the magnetic susceptibility contains the spin excitation resonance at low frequency. So the dynamical structure of the enhanced spin-current–spin density correlation function is essentially the same as that of the magnetic susceptibility. However, the frequency dependence of the specific elements is not the same, since the Kohn-Sham correlation function is not diagonal in spin space.

To analyse the physical meaning of the shown curves in more detail, let us consider a periodic magnetic perturbation in the x-direction applied only within the adatom atomic sphere given by

$$\delta\vec{B}(t) = \delta B \cos(\omega t)\hat{e}_x = \frac{\delta B}{2}\left(e^{i\omega t} + e^{-i\omega t}\right)\hat{e}_x \quad . \tag{7.4}$$

In linear response the time-dependent magnetization averaged over the atomic sphere can be calculated via

$$\begin{aligned} \delta\vec{m}(t) &= \int \mathrm{d}t' \; \boldsymbol{\chi}_{mm}(t-t')\delta\vec{B}(t') & (7.5) \\ &= \int \mathrm{d}t' \begin{pmatrix} \chi_{mm}^{xx}(t-t') \\ \chi_{mm}^{yx}(t-t') \end{pmatrix} \left(e^{i\omega t'} + e^{-i\omega t'}\right)\frac{\delta B}{2} \quad , & (7.6) \end{aligned}$$

where $\boldsymbol{\chi}_{mm}(t)$ is the magnetic susceptibility averaged over the atomic sphere. Using the transformation $\Delta t = t - t'$ yields

$$\begin{aligned} \delta\vec{m}(t) &= \int \mathrm{d}\Delta t \begin{pmatrix} \chi_{mm}^{xx}(\Delta t) \\ \chi_{mm}^{yx}(\Delta t) \end{pmatrix} \left(e^{i\omega t}e^{-i\omega\Delta t} + e^{-i\omega t}e^{i\omega\Delta t}\right)\frac{\delta B}{2} & (7.7) \\ &= \begin{pmatrix} \chi_{mm}^{xx}(-\omega)e^{i\omega t} + \chi_{mm}^{xx}(\omega)e^{-i\omega t} \\ \chi_{mm}^{yx}(-\omega)e^{i\omega t} + \chi_{mm}^{yx}(\omega)e^{-i\omega t} \end{pmatrix} \frac{\delta B}{2} \quad . & (7.8) \end{aligned}$$

Splitting the susceptibility into real and imaginary part yields using the symmetry relations of eq. (6.22) for $\omega \to -\omega$:

$$\boldsymbol{\chi}_{mm}(-\omega) = \mathrm{Re}\;\boldsymbol{\chi}_{mm}(\omega) - i\;\mathrm{Im}\;\boldsymbol{\chi}_{mm}(\omega) \quad . \tag{7.9}$$

Combining eqs. (7.9) and (7.8) yields the final result for the frequency-dependent magnetization:

$$\delta m^a(t) = \left\{\mathrm{Re}\chi_{mm}^{ax}(\omega)\cos(\omega t) + \mathrm{Im}\chi_{mm}^{ax}(\omega)\sin(\omega t)\right\}\delta B \qquad (a = x, y) \quad . \tag{7.10}$$

A similar approach gives access to the divergence of the spin-current, averaged over the atomic sphere, in terms of the spin-current–spin density correlation function:

$$\delta\vec{\nabla}\cdot\vec{j}^{\,a}(t) = \left\{\mathrm{Re}\left[\vec{\nabla}\cdot\chi_{jm}^{ax}(\omega)\right]\cos(\omega t) + \mathrm{Im}\left[\vec{\nabla}\cdot\chi_{jm}^{ax}(\omega)\right]\sin(\omega t)\right\}\delta B \quad . \tag{7.11}$$

This is an interesting result, since it shows that a unidirectional magnetic field can excite a precessional motion of the magnetic moment and induce spin-currents with both polarizations, which can be seen as follows: Consider for example the excitation frequency gB^{ext}, at which the time-dependent magnetization is given by

$$\delta\vec{m}(t)\Big|_{\omega_0 = gB^{\mathrm{ext}}} = \begin{pmatrix} \mathrm{Im}\chi_{mm}^{xx}(\omega_0)\sin(\omega_0 t) \\ \mathrm{Re}\chi_{mm}^{yx}(\omega_0)\cos(\omega_0 t) \end{pmatrix}\delta B \approx \mathrm{Im}\chi_{mm}^{xx}(\omega_0)\begin{pmatrix} \sin(\omega_0 t) \\ \cos(\omega_0 t) \end{pmatrix}\delta B \quad , \tag{7.12}$$

where we used

$$\mathrm{Re}\chi^{xx}_{mm}(\omega_0) \approx \mathrm{Im}\chi^{yx}_{mm}(\omega_0) \approx 0 \qquad \text{and} \qquad \mathrm{Im}\chi^{xx}_{mm}(\omega_0) \approx \mathrm{Re}\chi^{yx}_{mm}(\omega_0) \quad . \tag{7.13}$$

The same holds for the divergence of the induced spin-current, which is given by

$$\delta\vec{\nabla}\cdot\vec{j}^{\,a}(t)\Big|_{\omega_0=gB^{\mathrm{ext}}} = \begin{pmatrix} \mathrm{Re}\left[\vec{\nabla}\cdot\chi^{xx}_{jm}(\omega_0)\right]\cos(\omega_0 t) \\ \mathrm{Im}\left[\vec{\nabla}\cdot\chi^{yx}_{jm}(\omega_0)\right]\sin(\omega_0 t) \end{pmatrix}\delta B \approx \mathrm{Re}\left[\vec{\nabla}\cdot\chi^{ax}_{jm}(\omega_0)\right]\begin{pmatrix} \cos(\omega_0 t) \\ -\sin(\omega_0 t) \end{pmatrix}\delta B \quad , \tag{7.14}$$

with

$$\mathrm{Im}\left[\vec{\nabla}\cdot\chi^{xx}_{jm}(\omega_0)\right] \approx \mathrm{Re}\left[\vec{\nabla}\cdot\chi^{yx}_{jm}(\omega_0)\right] \approx 0 \qquad \text{and} \qquad \mathrm{Re}\left[\vec{\nabla}\cdot\chi^{xx}_{jm}(\omega_0)\right] \approx -\mathrm{Im}\left[\vec{\nabla}\cdot\chi^{yx}_{jm}(\omega_0)\right] \quad . \tag{7.15}$$

Thus at the excitation frequency both, the magnetic moment and the induced spin-current, are precessing in the clockwise direction, but the phase differs. The x-component of the spin-current is in phase with the external magnetic field, whereas the x-component of the magnetic moment has a phase shift of $-\frac{\pi}{2}$. This is exactly the behaviour we are expecting, since the time-derivative of the magnetic moment, which yields an additional phase of $\frac{\pi}{2}$, is connected to the divergence of the spin-currents via for example the spin continuity equation. To investigate this connection in more detail, let us focus on the spin continuity equation in the whole frequency regime.

Spin continuity equation

The spin continuity equation, eq. (2.37), can be used to connect the time-derivative of the magnetization density and the divergence of the spin current. For the x and y-component of the magnetization one finds

$$\begin{aligned} \partial_t\delta m^x + \vec{\nabla}\cdot\delta\vec{j}^{\,x} &= -\,2\mu_B\left(B^z\delta m^y - m^z\delta B^y\right) = -2\mu_B B^z\delta m^y \\ \partial_t\delta m^y + \vec{\nabla}\cdot\delta\vec{j}^{\,y} &= -\,2\mu_B\left(m^z\delta B^x - B^z\delta m^x\right) \end{aligned} \quad . \tag{7.16}$$

In the linear response calculation only the paramagnetic spin current is calculated. In the non-relativistic continuity equation the paramagnetic and diamagnetic spin current are relevant. However, it is easy to see, that in the discussed case the diamagnetic term does not contribute. Assume the Landau gauge, in which the vector potential is given by

$$\vec{A}(t) = B^z x\hat{e}^y + \delta B^x(t)y\hat{e}_z = A_y(x)\hat{e_y} + \delta A_z(y)\hat{e}_z \quad , \tag{7.17}$$

which yields for the diamagnetic spin current and its divergence in first order

$$\delta j^a_{k,\mathrm{dia}} = -\,2\delta\left(A_k m^a\right) = -2\left(\delta A_k m^a + A_k\delta m^a\right) \tag{7.18}$$

$$\Rightarrow \quad \vec{\nabla}\cdot\delta\vec{j}^{\,a}_{\mathrm{dia}} = \partial_k\delta j^a_{k,\mathrm{dia}} = -2\left[\partial_z\delta A_z(y)m^z + \partial_y A_y(x)\delta m^a\right] = 0 \quad . \tag{7.19}$$

Thus, in the discussed case the diamagnetic spin current does not contribute to the continuity equation.

Plugging eqs. (7.10) and (7.11) into the continuity equation (7.16) and comparing the prefactors of the (time-dependent) linearly independent sin and cos terms yields the following equations

$$x-\text{component:}\begin{cases}\omega\mathrm{Im}\chi^{xx}_{mm}(\omega)+\mathrm{Re}\left[\vec{\nabla}\cdot\chi^{xx}_{jm}(\omega)\right]=-2\mu_B B^z\mathrm{Re}\chi^{yx}_{mm}(\omega)\\-\omega\mathrm{Re}\chi^{xx}_{mm}(\omega)+\mathrm{Im}\left[\vec{\nabla}\cdot\chi^{xx}_{jm}(\omega)\right]=-2\mu_B B^z\mathrm{Im}\chi^{yx}_{mm}(\omega)\end{cases},\tag{7.20}$$

$$y-\text{component:}\begin{cases}\omega\mathrm{Im}\chi^{yx}_{mm}(\omega)+\mathrm{Re}\left[\vec{\nabla}\cdot\chi^{yx}_{jm}(\omega)\right]=2\mu_B B^z\mathrm{Re}\chi^{xx}_{mm}(\omega)-2\mu_B m^z\\-\omega\mathrm{Re}\chi^{yx}_{mm}(\omega)+\mathrm{Im}\left[\vec{\nabla}\cdot\chi^{yx}_{jm}(\omega)\right]=2\mu_B B^z\mathrm{Im}\chi^{xx}_{mm}(\omega)\end{cases}.\tag{7.21}$$

Let us analyse the first equation in (7.20), which corresponds to the $\cos(\omega t)$ time dependence of the continuity equation for x-polarization. Using figure 7.1 we can see all the relevant components of the spin-current–spin density correlation function and the magnetic susceptibility. The frequency dependence of the used quantities, $\mathrm{Im}\chi^{xx}_{mm}$, $\left[\vec{\nabla}\cdot\chi^{xx}_{jm}\right]$ and $\mathrm{Re}\chi^{yx}_{mm}$, is the same – they are peaked around the excitation frequency. However, a more quantitatively analysis shows, that the values do not coincide. At the excitation frequency, the first term ω $\mathrm{Im}\chi^{xx}_{mm}$ is of order ≈ 20, whereas the divergence of the current is $\left[\vec{\nabla}\cdot\chi^{xx}_{jm}\right]\approx 400$. At first sight, this could be related to a missing prefactor or to a mistake in the unit conversion.

However, there is a more fundamental problem in this equations. The scaling of the magnetic susceptibility with the external magnetic field is known to be $\chi_{mm}\propto 1/B_{\text{ext}}$. Applying different static external magnetic field the simulations show, that the Kohn-Sham spin-current–spin density correlation function does not reasonable scale with the external magnetic field. Using eq. (7.3) and the fact that the Kohn-Sham correlation function is much smaller than the enhanced magnetic susceptibility implies that the scaling of the divergence of the spin-current–spin density correlation function is also $\chi_{jm}\propto 1/B_{\text{ext}}$. Therefore, the left-hand side of eq. (7.20) scales like $\propto 1/B_{\text{ext}}$, whereas the right-hand side does not scale with the external magnetic field. Thus, the KKR results do not seem to satisfy the continuity equation in its present form

Spin-pumping theory

Another way to connect the susceptibility to the divergence of the spin-current is the spin-pumping theory discussed in section 6.5.1. To obtain the parameters A_i and A_r the gyromagnetic ratio and the damping parameter from the fit to the linearized LLG equation are used, which yields

$$A_i = 0.23 \quad\text{and}\quad A_r = 0.35 \quad .\tag{7.22}$$

Using eq. (6.88) and the form of the perturbation in eq. (7.4), the divergence of the pumped spin-current is given by

$$\vec{I}_{\text{pump}} = A_r m^z\begin{pmatrix}-\partial_t\delta m^y\\ \partial_t\delta m^x\end{pmatrix} - A_i\begin{pmatrix}\partial_t\delta m^x\\ \partial_t\delta m^y\end{pmatrix}\quad .\tag{7.23}$$

At this point it is not clear if the pumped spin-current $\vec{I}_{\text{pump}}$, which was originally developed for trilayer thin films, should apply to our KKR simulation, which considers a different geometry. However, let us assume for the moment that $I^a_{\text{pump}} = \vec{\nabla}\cdot\delta\vec{j}^{\,a}$.

Using eqs. (7.10) and (7.11) and looking at the prefactors of the linearly-independent sine and cosine terms yields the following four equations, which should be fulfilled:

$$x-\text{component:}\begin{cases}-A_r m^z\omega\ \mathrm{Im}\chi^{yx}_{mm}(\omega)-A_i\omega\ \mathrm{Im}\chi^{xx}_{mm}(\omega)=\mathrm{Re}\left[\vec{\nabla}\cdot\chi^{xx}_{jm}(\omega)\right]\\ A_r m^z\omega\ \mathrm{Re}\chi^{yx}_{mm}(\omega)+A_i\omega\ \mathrm{Re}\chi^{xx}_{mm}(\omega)=\mathrm{Im}\left[\vec{\nabla}\cdot\chi^{xx}_{jm}(\omega)\right]\end{cases}\quad, \tag{7.24}$$

$$y-\text{component:}\begin{cases}-A_r m^z\omega\ \mathrm{Im}\chi^{xx}_{mm}(\omega)-A_i\omega\ \mathrm{Im}\chi^{yx}_{mm}(\omega)=\mathrm{Re}\left[\vec{\nabla}\cdot\chi^{yx}_{jm}(\omega)\right]\\ A_r m^z\omega\ \mathrm{Re}\chi^{xx}_{mm}(\omega)+A_i\omega\ \mathrm{Re}\chi^{yx}_{mm}(\omega)=\mathrm{Im}\left[\vec{\nabla}\cdot\chi^{yx}_{jm}(\omega)\right]\end{cases}\quad. \tag{7.25}$$

This set of equations has two inconsistencies. On the one hand, none of the equations is fulfilled by our KKR results, when we compare the magnetic susceptibility elements to the spin-current–spin density correlation function results, either qualitatively or quantitatively. On the other hand, the equations do not match with the continuity equation, which can be seen as follows: Assuming that the spin-currents in eqs. (7.20) and (7.24) are equal yields the condition

$$A_r m^z\omega\ \mathrm{Im}\chi^{yx}_{mm}(\omega)+A_i\omega\ \mathrm{Im}\chi^{xx}_{mm}(\omega)\overset{!}{=}\omega\mathrm{Im}\chi^{xx}_{mm}(\omega)+2\mu_B B^z\mathrm{Re}\chi^{yx}_{mm}(\omega) \tag{7.26}$$

$$\Rightarrow\qquad \mathrm{Re}\chi^{yx}_{mm}(\omega)\overset{!}{=}\frac{\omega}{2\mu_B B^z}\left(A_r m^z\ \mathrm{Im}\chi^{yx}_{mm}(\omega)+(A_i-1)\ \mathrm{Im}\chi^{xx}_{mm}(\omega)\right)\quad. \tag{7.27}$$

Looking at the explicit curves in figure 7.1 it is obvious without plotting the right-hand side of eq. (7.27), that this equation can not be fulfilled by the KKR results using the values of A_i and A_r from eq. (7.22). Thus, there is an inconsistency between the continuity equation and the spin-pumping theory for the single adatom. However, the spin-pumping theory was developed for a different system – a layered system – so that we assume in the following sections that the continuity equation is the more fundamental equation, which should be fulfilled by the results.

In this section we discussed the dynamical spin-currents and the magnetic moments induced by an unidirectional monochromatic magnetic field. We saw that at the excitation frequency both quantities are precessing in spin space. However, using the simulation results we were not able to quantitatively verify the continuity equation. To investigate this problem in more detail, we go one step back and look at the $\omega = 0$ limit. It is already known, that in this limit there are some numerical issues with the magnetic susceptibility, which were solved by employing a sum rule [37]. Thus, it might be interesting to look at this limit with regard to the spin-current–spin density correlation function.

7.2. Static response

In this section the response to an external magnetic perturbation in the $\omega = 0$ limit is discussed. The same system as in the previous section is considered. We start with the well-known magnetic susceptibility results.

7.2.1. Static magnetic response

Table 7.1 shows the transversal block of the static Kohn-Sham and enhanced magnetic susceptibility, or the spin density–spin density correlation function $\boldsymbol{\chi}_{mm}$. The values are averaged over the Wigner-Seitz sphere of the iron adatom. Since we are not considering spin-orbit coupling, the susceptibility is diagonal and the xx and the yy elements are the same.

Let us focus on the results of the enhanced magnetic susceptibility, which can be explained using

χ^{KS}_{mm}		magnetic field direction	
		x	y
Polarization	x	-0.0013	0.0
	y	0.0	-0.0013

$\chi^{\mathrm{enhanced}}_{mm}$		magnetic field direction	
		x	y
Polarization	x	-3.47	0.0
	y	0.0	-3.47

Table 7.1.: Kohn-Sham (left) and enhanced (right) magnetic transversal susceptibility in [μ_B/ T]. Shown are the contributions averaged over the atomic sphere for the $\omega = 0$ limit.

the LLG picture. Consider for example a perturbing static magnetic field in the x-direction. The magnetic moment starts to precess around the total magnetic field but due to damping it slowly aligns with the magnetic field. After a long time, which is captured by the $\omega = 0$ limit of the magnetic susceptibility, the magnetic moment fully aligns with the magnetic field, which can be seen in the results as follows: Assume a small magnetic perturbation δB_x. The small polar angle θ between magnetic field and the z-axis is given by

$$\theta \approx \frac{\delta B_x}{B_z} = \frac{\delta B_x}{1\mathrm{T}} \quad , \tag{7.28}$$

whereas the polar angle of the magnetic moment is given by

$$\theta \approx \frac{\delta m_x}{m_z} = \frac{\chi_{xx}\delta B_x}{m_z} = \frac{3.473}{3.479}\frac{\delta B_x}{1\mathrm{T}} \quad . \tag{7.29}$$

Hence, up to a small numerical error the results show exactly the described behaviour. One reason for the numerical error is the applied external magnetic field of 10 T, which is quite small compared to the exchange-correlation magnetic field, so that numerics can cause problems. There are also further approximations made when constructing the response functions, which lead to further inaccuracies. To correct this error, a sum rule, which is a property the magnetic susceptibility should fulfil, was introduced in the code [37].

7.2.2. Static spin current response

Table 7.2 (left) shows the averaged Kohn-Sham spin-current–spin density correlation function in the $\omega = 0$ limit. As discussed in section 6.3.2 from the mathematical point of view the diagonal components have to be zero, whereas the off-diagonals can differ from zero. This is exactly what

$\chi^{\mathrm{KS}}_{j^z m}$		magnetic field direction	
		x	y
Polarization	x	0.0	0.0187
	y	-0.0187	0.0

$\chi^{\mathrm{enhanced}}_{j^z m}$		magnetic field direction	
		x	y
Polarization	x	0.0	6.13
	y	-6.13	0.0

Table 7.2.: Kohn-Sham (left) and enhanced (right) spin-current–spin correlation function in [$10^{-3}\mu_B$ / T]. Shown are the contributions averaged over the atomic sphere in the $\omega = 0$ limit. Due to the symmetry of the iron adatom on the Pt(111)-surface the currents are flowing in the z-direction.

we obtain: The off-diagonal components for the flow in the spatial z-direction are non-zero.
A more detailed picture is shown in figure 7.2, which shows the spatial flow of the y-polarized Kohn-Sham current for a static magnetic field perturbation in the x-direction. Shown is the constant $y = 0$-plane. One can see a finite current flowing from the center of the sphere towards the vacuum layers. The currents in the lower half circle are much smaller and have the same symmetry as the lattice. Already at this level, we can say that there is a source generating spin-current, which results in a finite divergence. Figure 7.3 shows the divergence of the y-polarized spin-current. In the top view the symmetry of the lattice is visible. In the side view one can see the strong variation of the divergence in the upper half circle compared to the lower half circle, which is more homogeneous.

Let us go on with the renormalized results of the interacting system shown in table 7.2 (right). The structure is similar to the non-interacting system. Only the actual values vary by approximately 3 orders of magnitude. The enhancement of the spin-current–spin density correlation function comes from the enhanced magnetic susceptibility, see eq. (7.3). The matrix structure itself indicates a precession. A magnetic perturbation in the x-direction induces a y-polarized spin current, whereas a magnetic perturbation in the y-direction induces a x-polarized spin current of opposite sign. Figure 7.4 shows the y-polarized renormalized spin current in a constant $y = 0$ plane. The flow is quite similar to the Kohn-Sham spin current. There is a large flow towards the vacuum spheres, whereas the flow from the surface is smaller, which results in an effective generation of spin current and a finite divergence. However, there are some crucial differences regarding the amplitude. For the Kohn-Sham spin current the flow towards the vacuum is decreasing close to the boundary of the Wigner-Seitz sphere, whereas the amplitude of the renormalized spin current is increasing towards the boundary.
The divergence is shown in figure 7.5. One can see that the divergence is everywhere positive. The top view shows once again the symmetry of the lattice. The side view differs from the Kohn-Sham spin current. Close to the surface the variation in the divergence is larger than close the the vacuum layer. This is related to the more homogeneous flow towards the vacuum layer.

Spin continuity equation

As pointed out in section 7.1, the spin continuity equation is not satisfied by the dynamical simulation results. Let us have a more quantitative look for the $\omega = 0$ limit. The spin continuity equation (2.37) without relativistic corrections for the y-polarization is given by

$$\partial_t m^y + \vec{\nabla} \cdot \vec{j}^{\,y} = 2\mu_B \left(B^z m^x - B^x m^z \right) \quad . \tag{7.30}$$

In frequency space the time derivative simplifies to $\partial_t \to -i\omega$. Assuming the static perturbation in the x-direction the magnetic moment can be written in terms of the susceptibility, which yields

$$-i\omega \chi^{yx}_{mm} \delta B^x + \vec{\nabla} \cdot \vec{j}^{\,y} = 2\mu_B \left(B^z \chi^{xx}_{mm} \delta B^x - m^z \delta B^x \right) \quad . \tag{7.31}$$

The right-hand side of eq. (7.31) corresponds to the torque. As shown in eq. (7.29), in the $\omega = 0$ limit the magnetic moment fully aligns with the magnetic field up to some small numerical error, so that the torque vanishes. Since χ^{yx}_{mm} is not singular at $\omega = 0$ the continuity equation simplifies to

$$\vec{\nabla} \cdot \vec{j}^{\,y} = \mathrm{Re} \left[\vec{\nabla} \cdot \chi^{yx}_{jm}(\omega = 0) \right] \delta B^x = 0 \quad , \tag{7.32}$$

which indicates that there should not be any pumped spin-current for a static magnetic field perturbation.

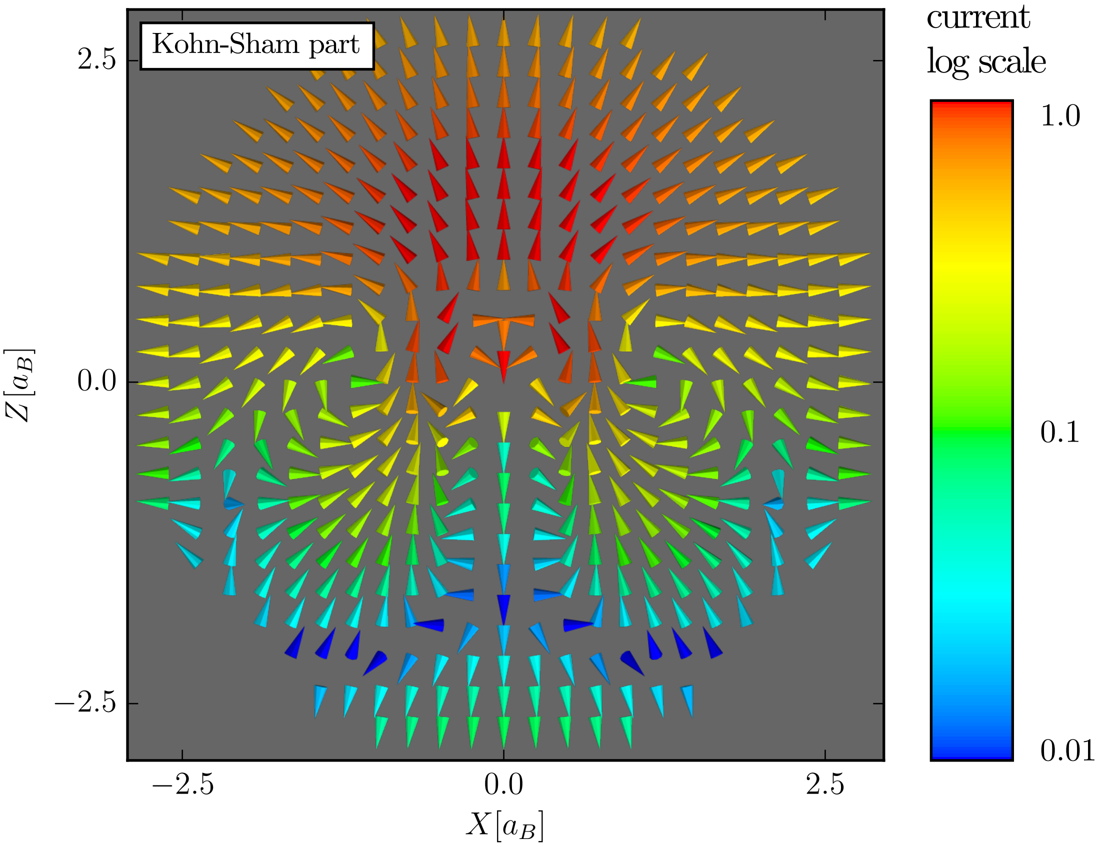

Figure 7.2.: Flow of the y-polarized Kohn-Sham spin current. Shown is the $y = 0$ plane with the platinum surface below the adatom at $z < 0$.

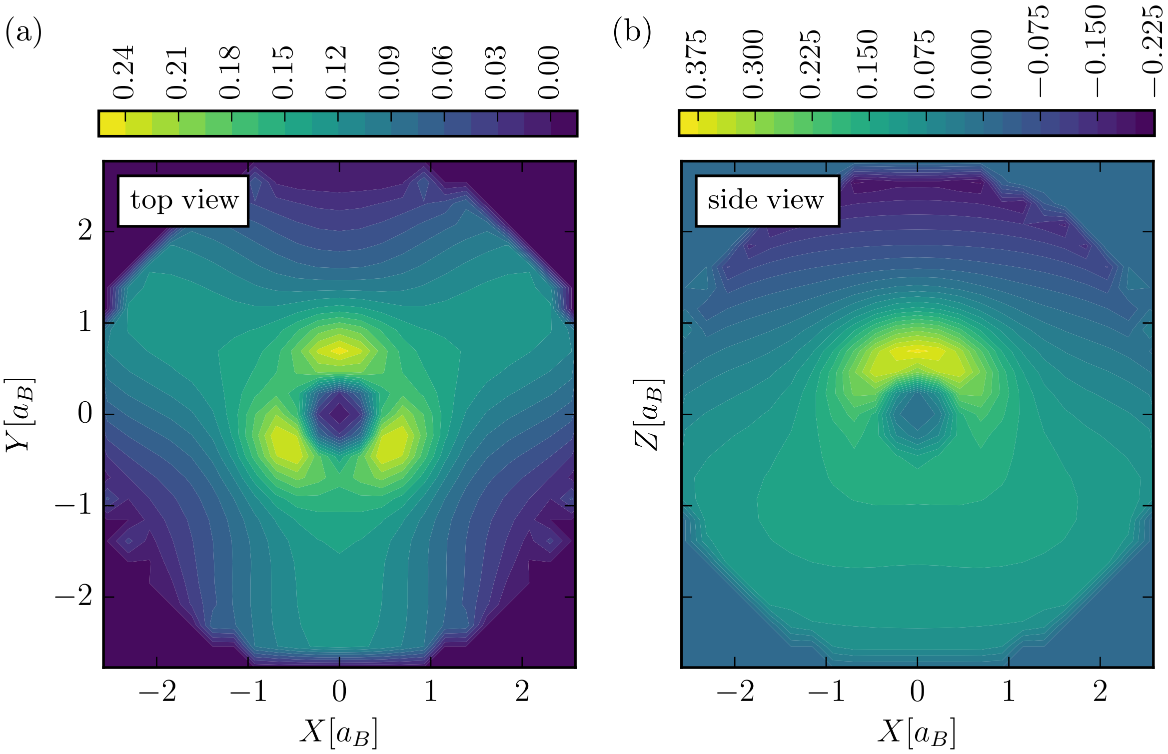

Figure 7.3.: Divergence of the y-polarized Kohn-Sham spin-current shown in fig. 7.2.

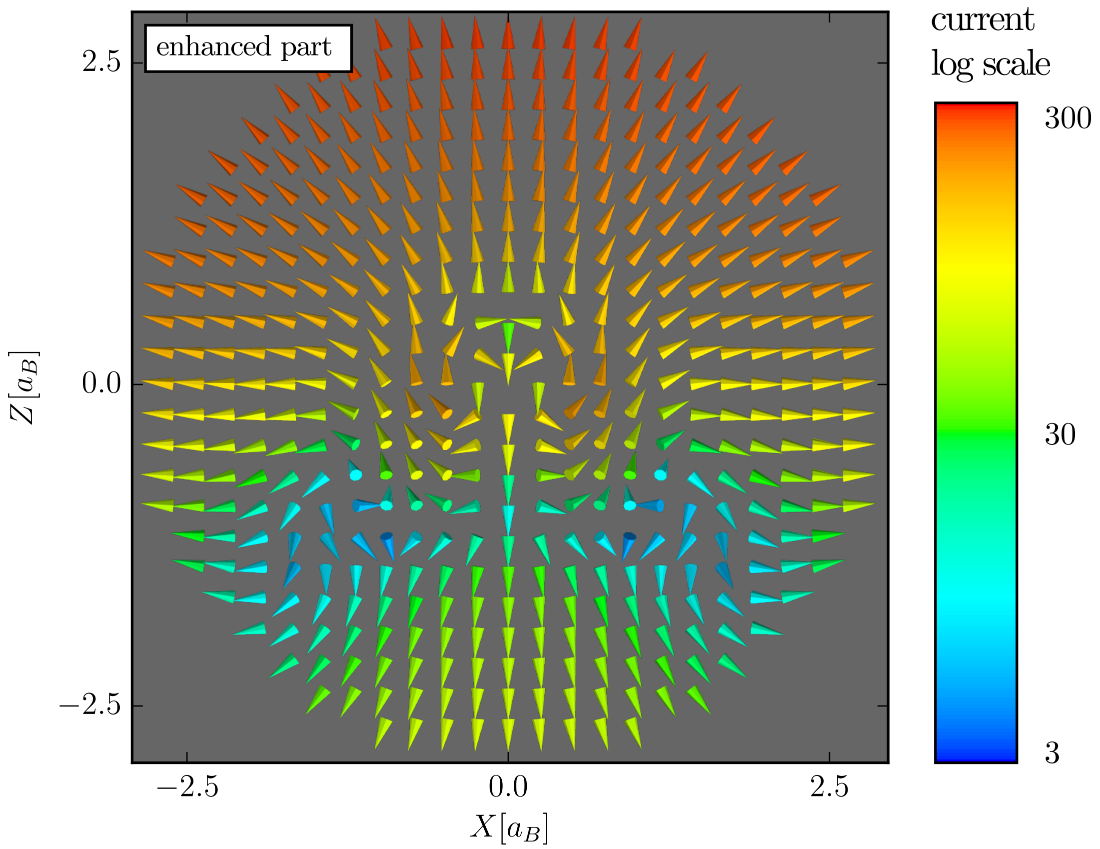

Figure 7.4.: Flow of the y-polarized renormalized spin current. Shown is the $y = 0$ plane with the platinum surface below the adatom at $z < 0$.

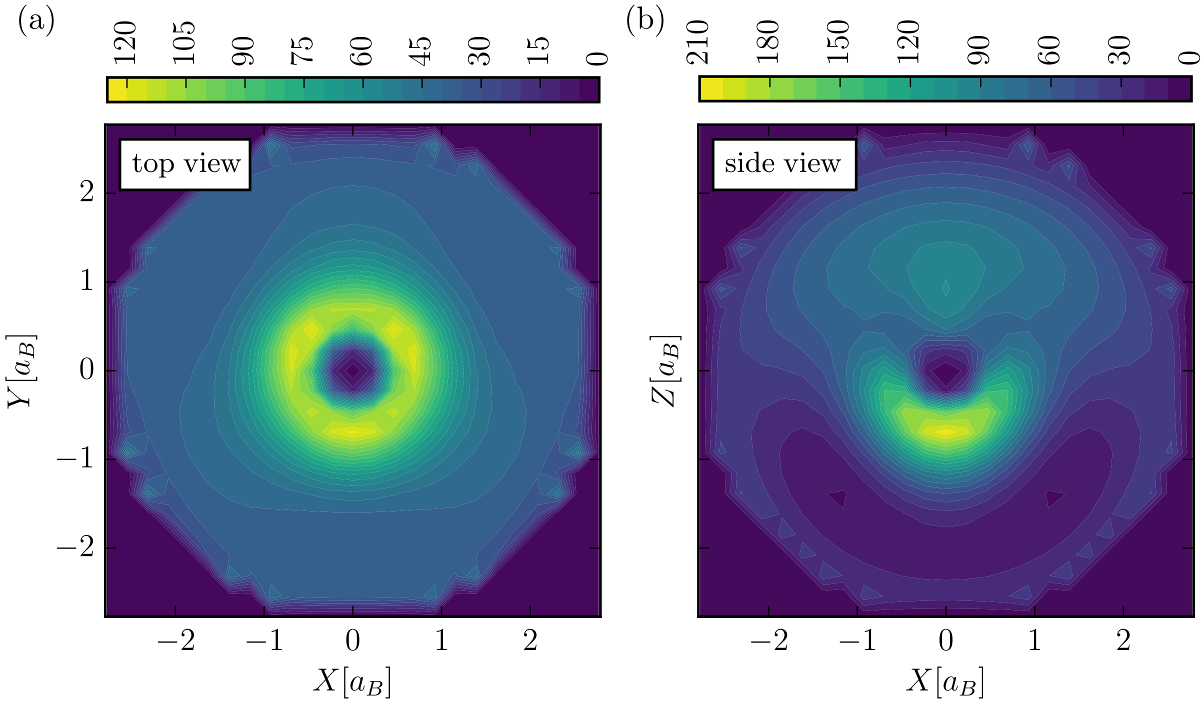

Figure 7.5.: Divergence of the y-polarized spin current shown in fig. 7.4.

However, we know that the torque in the $\omega = 0$ limit is not identically zero in the simulation due to a numerical error. So the reader might ask, if this error could be responsible for the finite divergence of the spin-current. To investigate this further, we look at the scaling with the external magnetic field of all quantities.

Scaling with the external magnetic field

The scaling with the external magnetic field of the torque and the divergence of the spin-current is shown in table 7.3 for three different magnetic fields in the $\omega = 0$ limit. The torque part is nearly constant, explained by the magnetization sum rule [37], but the divergence of the spin current is scaling with $1/B^{\text{ext}}$, so that the numerical error in the torque part can not explain the finite divergence.

Using the definition of the enhanced spin-current–spin correlation function one can easily prove this scaling behavior:

$$\chi^{ab} = \underbrace{\chi_0^{ab}}_{\approx\text{const.}} + \sum_{cd} \underbrace{\chi_0^{ac}\mathcal{K}_{\text{xc}}^{cd}}_{\approx\text{const.}} \underbrace{\chi^{db}}_{\propto 1/B_{\text{ext}}} \quad . \tag{7.33}$$

The Kohn-Sham correlation function is approximately constant with the external magnetic field. The same holds for the exchange-correlation kernel. Thus the only quantity, which has a reasonable scaling is the enhanced magnetic susceptibility with a scaling $\propto 1/B_{\text{ext}}$. In addition, the Kohn-Sham correlation function is usually a few order of magnitude smaller than the enhanced one, such that the total scaling of the enhanced correlation function is approximately $\propto 1/B_{\text{ext}}$.

The only way, to overcome this scaling problem is for the divergence of the static Kohn-Sham correlation function to vanish, so that the scaling does not matter anymore. At present our results contradict this assumption.

Furthermore, the underlying physical picture yields additional doubts about the $\omega = 0$ result, which is discussed in the next paragraph.

Connection to the LLG model

The static magnetic perturbation induces a precessional damped motion of the magnetic moment, which can be described by the LLG equation. During the precession spin currents are periodically induced. However, as we already discussed in section 7.2.1 the precession is damped resulting in a

Quantity	magnetic field strength			scaling
	100 Tesla	20 Tesla	10 Tesla	
$B^z\chi^{xx}$	3.4771	3.4736	3.4736	$\propto$ const.
m^z	3.4831	3.4797	3.4792	$\propto$ const.
$B^z\chi^{xx} - m^z$	-0.0060	-0.0061	-0.0056	$\propto$ const.
$\vec{\nabla} \cdot j^y_{\text{enhanced}}$	15.37	76.7	153.4	$\propto 1/B^{\text{ext}}$

Table 7.3.: Scaling with the external magnetic field of the quantities appearing in the continuity equation (7.31) for the $\omega = 0$ limit.

finite precession time. After the magnetic moment is aligned with the external magnetic field there should not be any induced spin current with finite divergence, which is described by the $\omega = 0$ limit. In total, this physical picture predicts no finite spin currents in the $\omega = 0$ limit, which is a contradiction to the found results.

Possible sources of the error

The errors can have different sources. In our method we are using many approximations, some of which could lead to wrong results. At the moment the most probable reason for the incorrect $\omega = 0$ behavior of the spin-current–spin density correlation function is a numerical error. In case of the magnetic susceptibility we already saw a small numerical error concerning the alignment of the magnetic moments with the external magnetic field in section 7.2.1. The problem was fixed in the code by the introduction of a sum rule, which is basically a property the magnetic susceptibility has to fulfill [37]. However, at the moment we do not have such a check for the spin-current–spin density correlation function, so that numerical errors might lead to incorrect results.

7.3. Spin-orbit coupling effects

Spin-orbit coupling breaks the continuous rotational symmetry in spin space by coupling the spin momentum and the angular momentum. As a result, different effects originate from the coupling of spin space and real space, but the most important one for this section is the magnetic anisotropy, which introduces a dependence of the total energy on the direction of the magnetic moment. Usually there is an easy axis, which is energetically preferred for the alignment. It can be shown that an adatom on the Pt(111) with its C_{3v}-symmetry is well-described by the model spin Hamiltonian [37]

$$\mathcal{H} = -K m_z^2 \quad , \tag{7.34}$$

with the easy axis in-plane or out-of-plane depending on the sign of the parameter K. The magnetic anisotropy energy (MAE) of an iron adatom on top of Pt(111) is approximately $K m_z^2 \approx 1.10\text{meV}$, which is obtained from the KKR simulation by comparing the band energy of the system with out-of-plane magnetization to the one with the in-plane magnetization. Thus, the ground state has an out-of-plane magnetization. The magnetic anisotropy energy corresponds to an magnetic field $\vec{B}^{\text{MAE}}$, which is given by

$$\vec{B}^{\text{MAE}} = -\frac{\partial E^{\text{MAE}}}{\partial \vec{m}} = 2K m_z \hat{e}_z = \frac{2K m_z^2}{m_z} = \frac{2\ 1.1\text{meV}}{3.46\mu_B} = 11.0\text{T} \quad , \tag{7.35}$$

resulting in a total effective magnetic field of $\vec{B}^{\text{eff}} = \vec{B}^{\text{ext}} + \vec{B}^{\text{MAE}}$. Therefore, applying a magnetic perturbation perpendicular to the anisotropy easy axis we expect the magnetic moment to not fully align with the external magnetic field, but to tilt slightly in the direction of the perturbation.
In the simulation we consider a static external magnetic field of 10 T in the z-direction. The static magnetic susceptibility is still diagonal but the amplitude differs drastically from the case without spin-orbit coupling. The polar angle of the induced magnetic moment is given by

$$\theta_m = \frac{\chi^{xx} \delta B^x}{m^z} = \frac{1.336}{3.465} \frac{\delta B^x}{10T} \approx \frac{\delta B^x}{25.9T} \quad , \tag{7.36}$$

whereas the polar angle of the external magnetic field is $\theta_B = \delta B^x / 10T$. The reason for this is the magnetic anisotropy and the corresponding effective magnetic field. From this calculation we obtain a MAE magnetic field of 15.9 T, which slightly differs from eq. (7.35). However, we are comparing two different kinds of calculations, which could yield different results. In particular, the result of the band energy differences is very sensitive to the size of the real-space cluster [49].

Let us continue with the static spin-current–spin correlation function. Without spin-orbit coupling, only the off-diagonal elements of this function were finite. With spin-orbit coupling also the diagonal elements of the static spin-current–spin correlation function are finite.
Consider a magnetic perturbation in the x-direction. The resulting y-polarized spin-current looks qualitatively similar to the induced spin-current without spin-orbit coupling. The amplitude changes, but the direction of the flow is quite similar, so that the main problem concerning the continuity equation remains the same.
However, spin-orbit coupling yields an additional x-polarized spin-current, which was not present before. Figure 7.6 shows the flow of the x-polarized spin-current. The currents are obviously bound, which can be seen in the divergence shown in figure 7.7. The integrated divergence vanishes, which means that in total there is no net flow of the spin-current out of the Wigner-Seitz sphere. However, the divergence is not zero everywhere, which could be related to the rigid spin approximation. The rigid spin approximation assumes a uniform spin quantization axis in each atomic sphere, which is not correct in case of spin-orbit coupling since spin-orbit coupling naturally leads to a three-dimensional spin density. Therefore, the actual ground state of the system could be different resulting in finite spin currents.

In addition to the static behavior, figure 7.8 shows the frequency dependence of the divergence of the spin-current–spin correlation function and the magnetic susceptibility. One can notice that the excitation frequency is shifted compared to the case without spin-orbit coupling by a factor of 2.59, which corresponds to a MAE magnetic field of 15.9 T. Apart from the overall shift, the frequency dependence of all the elements is similar to the frequency dependence without spin-orbit coupling.

To summarize, spin-orbit coupling results in finite diagonal components of the spin-current–spin density correlation function, which means that for an magnetic perturbation in the x-direction an additional finite x-polarized spin current is induced. However, the finite diagonal components vanish within the divergence calculation, so that the frequency dependence of the divergence, which is the important quantity, is similar to the calculations without spin-orbit coupling.

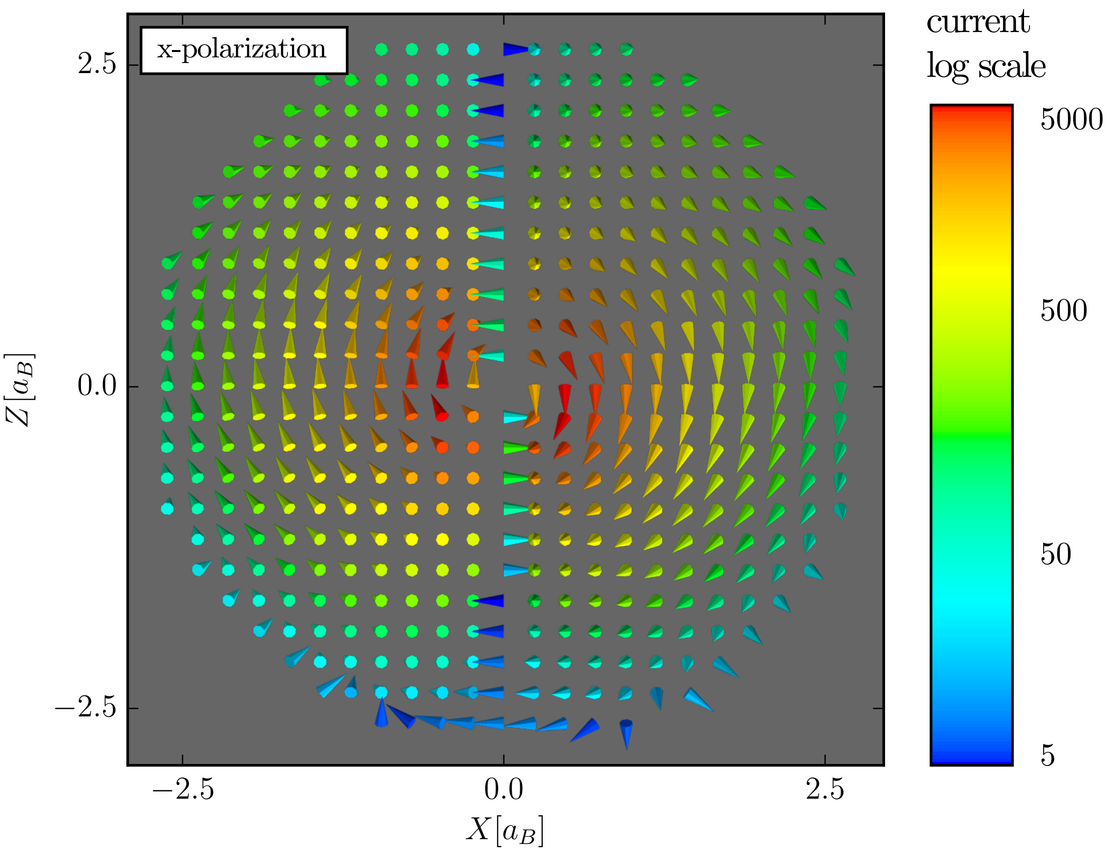

Figure 7.6.: Flow of the x-polarized renormalized spin current with SOC. Shown is the $y = 0$ plane with the platinum surface below the adatom at $z < 0$.

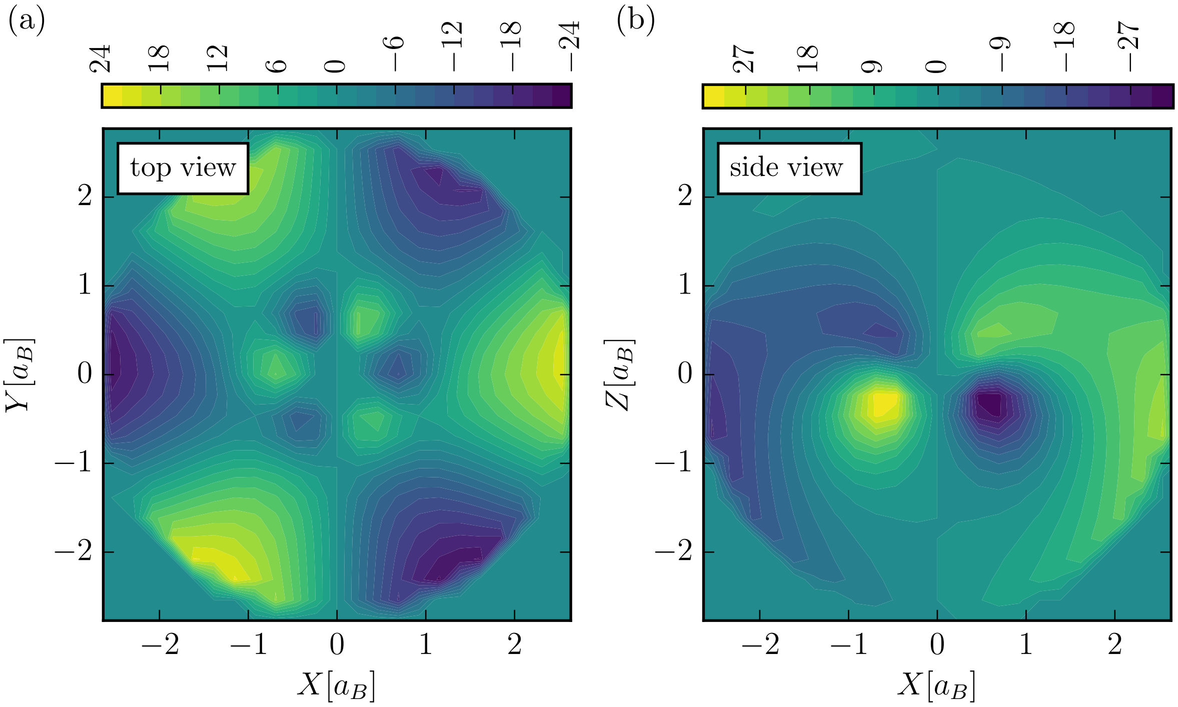

Figure 7.7.: Divergence of the x-polarized spin current shown in fig. 7.6.

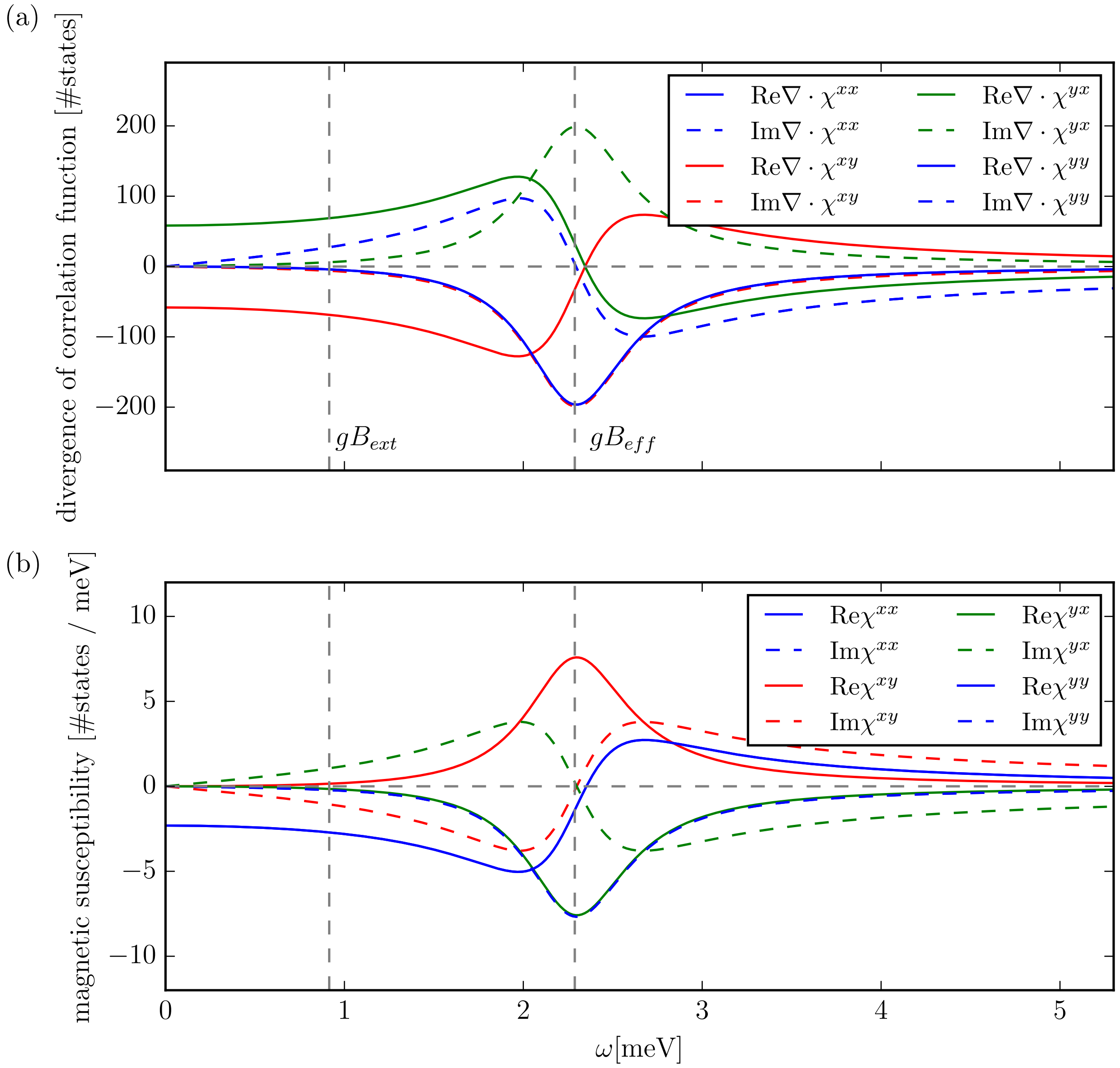

Figure 7.8.: (a) Divergence of the spin-current–spin correlation function as function of frequency with spin-orbit coupling averaged over the atomic sphere. (b) Magnetic susceptibility as function of frequency with spin-orbit coupling averaged over the atomic sphere. The leftmost dashed vertical line indicates the peak position without spin-orbit coupling, whereas the rightmos dashed line corresponds to the excitation frequency with spin-orbit coupling.

7.4. Summary

In this chapter, spin currents and magnetization dynamics induced by an (dynamical) external magnetic field were discussed. The magnetic susceptibility and the spin-current–spin density correlation function were calculated for an iron atom deposited on Pt(111).
In the first part, the frequency dependence of the dynamical spin-current–spin density correlation function and the magnetic susceptibility were discussed. Applying an unidirectional periodical magnetic perturbation, we found both quantities – the magnetic moment and the divergence of

the spin current – precessing in spin space. Using the results in the continuity equation indicated some problems, which could be related to the $\omega = 0$ limit. Therefore in the second part, the $\omega = 0$ limit was discussed by using a static magnetic field perturbation. Using the magnetic susceptibility we were able to describe the alignment of the magnetic moment moment with the static external magnetic field. However, the spin-current–spin density correlation function showed an unexpected behaviour in the $\omega = 0$ limit, finite spin currents. The underlying physical picture predicts that there should not be finite spin currents in the $\omega = 0$ limit. A possible reason for this is a numerical error. We believe that developing a sum rule similar to the one used to correct the dynamical magnetic susceptibility will clarify this matter.

In the final part of this chapter, we discussed the effects of spin-orbit coupling on the magnetic susceptibility and the spin-current–spin density correlation function. We found the MAE to shift the excitation frequency, since it is acting as an effective magnetic field. Furthermore, spin-orbit coupling induces finite diagonal components in the spin-current–spin correlation function, which vanish for $\omega = 0$ in the divergence calculation, but might play a role in dynamical processes.

8. Summary and outlook

The main focus of this work was the study of charge and spin currents in magnetic nanostructures. Within the KKR-DFT scheme I was able to develop two methods describing charge and spin currents of static and dynamical origins. On the one hand, I investigated ground state charge and spin currents, which are induced by spin-orbit coupling and other symmetry-breaking effects such as non-collinear magnetism. On the other hand, dynamical spin currents were also investigated, which were induced by dynamical external magnetic fields, and are important for understanding spin dynamics.

In case of the ground state charge currents, I presented simulations of single iron adatoms deposited on different platinum surfaces. Using the electronic structure of the adatom on top of the hexagonal surface, I could motivate an Anderson-like model Hamiltonian, which yielded first insights to the charge current distribution in the adatom. The model as well as the KKR calculation showed a purely swirling charge current.

Furthermore, I investigated the connection between ground state charge currents and orbital magnetic moments. Using a simple relation, which is even known from classical electrodynamics but strictly valid only for finite systems, I could calculate the orbital magnetic moment via the ground state charge current. I have analyzed an additional contribution resulting from the net currents flowing through the Wigner-Seitz spheres, which was neglected in previous calculations of the orbital magnetic moment within the KKR scheme.

In addition to single adatoms, I presented calculations of an iron dimer, an iron trimer and a non-collinear iron trimer, which was calculated without spin-orbit coupling. In the non-collinear iron trimer the finite scalar spin chirality, $\vec{S}_1 \cdot \left(\vec{S}_2 \times \vec{S}_3\right)$, was responsible for the emergence of finite ground state charge currents and the resulting finite orbital magnetic moments.

For the simulation of ground state spin currents, I reported only on a single system – an iron adatom deposited on Pt(111). The most important result was the emergence of finite net spin currents through the whole cluster. At the surface the simulation predicted finite x- and y-polarized spin currents, which are not bounded. Even if this result sounds strange at first sight, I showed that the spin currents have a vanishing divergence, such that the results are in accordance with the continuity equation. Furthermore, I highlighted the possibility of finite spin currents at surfaces as it is known for example for Rashba systems [46].

In the second part of this work, I investigated dynamical spin currents induced by external magnetic fields within linear response. I developed a KKR based method to calculate the spin-current–spin density correlation function, which can be divided into two steps: First, the spin-current–spin correlation function of the Kohn-Sham system has to be calculated, which is closely connected to the magnetic susceptibility of the Kohn-Sham system. Then the exchange-correlation effects have to be considered, resulting in a renormalization of the Kohn-Sham spin-current–spin density correlation function. A detailed description of the implementation of these two steps was given.

Furthermore, I discussed how magnetization dynamics described by the LLG equation can be connected to spin currents, which are induced by the magnetization dynamics, using the description of Tserkovnyak [5].

The developed method was applied to an iron adatom deposited on Pt(111) without spin-orbit coupling. The frequency dependence of the spin-current–spin correlation function was analyzed. It was shown that the frequency dependence of the spin-current–spin correlation function is fully governed by the frequency dependence of the magnetic susceptibility. Applying an unidirectional periodical magnetic field perturbation, it was shown that both – the magnetization and the divergence of the spin-current – are precessing in spin space. The continuity equation was used to connect the resulting time-dependent magnetic moment to the resulting divergence of the spin-current. Qualitatively the frequency dependence of the connected quantities matched, but using the actual numbers I found a discrepancy. To analyze this discrepancy, I went one step back and discussed the $\omega = 0$ limit of the simulations. In this limit, which corresponds to the long time behavior, I expected no finite spin-currents, since the magnetic moment is fully aligned with the external magnetic field. However, the results showed a finite spin-current, in disagreement with the continuity equation and the spin-pumping theory of Tserkovnyak, which predicts pumped spin-currents linear in the frequency. A possible reason for the discrepancy is a numerical error. For the magnetic susceptibility, there is a well-known numerical error in the $\omega = 0$ limit, which was corrected by using a sum rule [37]. However, at the moment I do not know of any sum rule for the spin-current–spin density correlation function to correct the $\omega = 0$ limit.

In the last part of the results, I discussed the effects of spin-orbit coupling on the induced spin currents. First I showed that the magnetic anisotropy yields a shift in the excitation frequency, since it acts as an additional effective magnetic field. Furthermore, I analyzed the occurrence of diagonal elements of the spin-current–spin density correlation function in the static limit, which were exactly zero without spin-orbit coupling. I showed that these currents are bound such that the divergence is vanishing and the continuity equation is fulfilled.

To conclude the summary, I provide an outlook of what can still be done and what I could improve. Regarding the ground state currents and the orbital magnetic moment, the new method could be used to analyze more complex systems. I found, that the net current contribution of the orbital magnetic moment in the non-collinear compact trimer had the same order of magnitude as the on-site contribution. The reason was the presence of the flowing net currents in the trimer. As a next step, I could investigate a larger ring-like structure, in which even larger net current contributions to the orbital magnetic moment might be expected. Another interesting target system would be nano-skyrmions, which are currently attracting a lot of attention [50]. Due to the magnetic structure of a two dimensional skyrmion, I expect ground state ring-like currents resulting in a large net current contribution to the orbital magnetic moment, which was not captured by previous first-principles simulations.

Regarding the implementation of the dynamical spin-currents induced by magnetic fields, more theoretical and numerical development is still needed. To check the numerics, which are believed to cause the discussed discrepancies, I have to find an analytical property of the spin-current–spin density correlation function, as it was done in case of the magnetic susceptibility with the sum rule. Therefore, it might be useful to develop a model for a single adatom, which captures more details than the model discussed in this thesis, to understand the physics of dynamical induced spin-currents in more detail. After achieving this goal, there are a lot of interesting systems which could be analyzed. For example a detailed analysis of the dynamics of a skyrmion induced by an external magnetic field will surely uncover new and interesting effects.

A. Atomic Rydberg units

Within this work atomic Rydberg units are used. In the unit system the following fundamental physical constants are defined:

Definition	Quantity
$\hbar = 1$	Planck constant
$a_B = 1$	Bohr radius
$\mathrm{Ry} = 1$	Rydberg energy
$4\pi\epsilon_0 = 1$	Coulomb constant

Furthermore, the following important quantities are defined via these fundamental constants:

	Quantity
$e = \sqrt{2}$	elementary charge
$m_e = \frac{1}{2}$	electron mass
$\mu_B = \sqrt{2}$	Bohr magneton

However, in this work usually the Bohr magneton is kept in the equation to allow easy comparison to other unit systems for magnetic quantities and to avoid factors of $\sqrt{2}$.

B. Maxwell equations

The Maxwell equations are the fundamental equations in electromagnetism [13]. They are a closed set of differential equations describing electromagnetic fields via charges and charge currents:

$$\vec{\nabla} \cdot \vec{E} = 4\pi\rho \quad , \tag{B.1}$$

$$\vec{\nabla} \cdot \vec{B} = 0 \quad , \tag{B.2}$$

$$\vec{\nabla} \times \vec{E} = -\frac{1}{c}\frac{\partial \vec{B}}{\partial t} \quad , \tag{B.3}$$

$$\vec{\nabla} \times \vec{B} = \frac{4\pi}{c}\vec{j} + \frac{1}{c}\frac{\partial \vec{E}}{\partial t} \quad , \tag{B.4}$$

where $\vec{E}$ is the electric field, $\vec{B}$ is the magnetic field, ρ is the charge density and $\vec{j}$ is the charge current. One can show that the electric field and the magnetic field can be written in terms of a potential ϕ and a vector potential $\vec{A}$:

$$\vec{E} = -\vec{\nabla}\phi - \frac{1}{c}\frac{\partial \vec{A}}{\partial t} \quad , \tag{B.5}$$

$$\vec{B} = \vec{\nabla} \times \vec{A} \quad . \tag{B.6}$$

In this work the potential ϕ corresponds to the ionic potential v.

C. Dirac equation

The Dirac equation for an particle in an electromagnetic field is given by

$$i\hbar\frac{\partial\Psi}{\partial t}(\vec{r};t) = \left(c\vec{\alpha}\cdot\left(\vec{p} - e\vec{A}(\vec{r};t)\right) + \beta mc^2 + V(\vec{r};t)\right)\Psi(\vec{r};t) \quad , \tag{C.1}$$

where the matrices $\vec{\alpha}$ and β are given by

$$\vec{\alpha} = \begin{pmatrix} 0 & \vec{\boldsymbol{\sigma}} \\ \vec{\boldsymbol{\sigma}} & 0 \end{pmatrix} \qquad \text{and} \qquad \beta = \begin{pmatrix} \boldsymbol{\sigma}_0 & 0 \\ 0 & -\boldsymbol{\sigma}_0 \end{pmatrix} \quad . \tag{C.2}$$

The wavefunction Ψ is a four-component vector, which can be decomposed into two spinors – ϕ called big component and χ called small component

$$\Psi = \begin{pmatrix} \phi_\uparrow \\ \phi_\downarrow \\ \chi_\uparrow \\ \chi_\downarrow \end{pmatrix} = \begin{pmatrix} \phi \\ \chi \end{pmatrix} \quad , \tag{C.3}$$

such that the Dirac equation simplifies to a set of coupled differential equations:

$$i\hbar\frac{\partial\phi}{\partial t} = c\vec{\boldsymbol{\sigma}}\cdot\left(\vec{p} - e\vec{A}\right)\chi + \left(V + mc^2\right)\phi \quad , \tag{C.4}$$

$$i\hbar\frac{\partial\chi}{\partial t} = c\vec{\boldsymbol{\sigma}}\cdot\left(\vec{p} - e\vec{A}\right)\phi + \left(V - mc^2\right)\chi \quad , \tag{C.5}$$

where the dependencies on $\vec{r}$ and t were skipped to simplify the notation. To explain why the small component χ is actually small compared to the big component ϕ, the replacement

$$i\hbar\frac{\partial\chi}{\partial t} \to \left(i\hbar\frac{\partial\chi}{\partial t} - mc^2\chi\right) + mc^2\chi \quad , \tag{C.6}$$

can be inserted to eq. (C.5) yielding

$$\chi = \frac{1}{2mc}\vec{\boldsymbol{\sigma}}\cdot\left(\vec{p} - e\vec{A}\right)\phi + \frac{1}{2mc^2}\underbrace{\left(-i\hbar\frac{\partial}{\partial t} + V + mc^2\right)}_{\approx V}\chi \tag{C.7}$$

$$\approx \frac{1}{2mc}\vec{\boldsymbol{\sigma}}\cdot\left(\vec{p} - e\vec{A}\right)\phi, \quad , \tag{C.8}$$

so that the small component is approximately by the factor $\frac{v}{c} \ll 1$ smaller than the big component, which is only valid for sufficiently small scalar potentials V.

Furthermore, the expansion of the small component can be used to arrive at the non-relativistic limit of the Dirac equation by plugging eq. (C.8) into eq. (C.4) yielding

$$i\hbar\frac{\partial\phi}{\partial t} = \frac{1}{2m}\left(\vec{\boldsymbol{\sigma}}\cdot\left(\vec{p} - e\vec{A}\right)\right)^2\phi + \left(v + mc^2\right)\phi \quad . \tag{C.9}$$

Using the following relation for the Pauli matrices,

$$\left(\vec{\boldsymbol{\sigma}} \cdot \vec{a}\right)\left(\vec{\boldsymbol{\sigma}} \cdot \vec{b}\right) = \vec{a} \cdot \vec{b}\,\boldsymbol{\sigma}_0 + i\left(\vec{a} \times \vec{b}\right) \cdot \vec{\boldsymbol{\sigma}} \quad , \tag{C.10}$$

eq. (C.9) simplifies to the Pauli equation:

$$i\hbar\frac{\partial\phi}{\partial t} = \frac{1}{2m}\left(\vec{p} - e\vec{A}\right)^2 \phi - \frac{e\hbar}{2m}\vec{\boldsymbol{\sigma}} \cdot \vec{B}\phi + \left(v + mc^2\right)\phi \quad . \tag{C.11}$$

An important point is the normalization of the big component ϕ. The whole wavefunction Ψ is normalized by construction:

$$1 = \int \mathrm{d}\vec{r}\ \Psi^\dagger\Psi \tag{C.12}$$

$$= \int \mathrm{d}\vec{r}\ \left(\phi^\dagger\phi + \chi^\dagger\chi\right) \quad . \tag{C.13}$$

Using the expansion given in eq. (C.8) for the small component one finds

$$1 = \int \mathrm{d}\vec{r}\ \left[\phi^\dagger\phi + \mathcal{O}\left(\left(\frac{v}{c}\right)^2\right)\right] \quad , \tag{C.14}$$

so that the big component is normalized up to first order in $\frac{v}{c}$.
Eq. (C.7) can be used to systematically expand the Dirac equation in higher orders of $\frac{v}{c}$ by iteratively plugging the resulting small component into eq. (C.4). The first relativistic corrections are found by using

$$\chi = \frac{1}{2mc}\vec{\boldsymbol{\sigma}} \cdot \left(\vec{p} - e\vec{A}\right)\phi + \frac{1}{2mc^2}\left(-i\hbar\frac{\partial}{\partial t} + V + mc^2\right)\frac{1}{2mc}\vec{\boldsymbol{\sigma}} \cdot \left(\vec{p} - e\vec{A}\right)\phi + \mathcal{O}\left(\left(\frac{v}{c}\right)^3\right) \quad . \tag{C.15}$$

Before we start, the normalization of the big component can be analyzed.

$$1 = \int \mathrm{d}\vec{r}\ \left\{\phi^\dagger\left[1 - \frac{1}{2mc}\vec{\boldsymbol{\sigma}} \cdot \left(\overleftarrow{p} + e\vec{A}\right)\right] \times \left[1 + \frac{1}{2mc}\vec{\boldsymbol{\sigma}} \cdot \left(\vec{p} - e\vec{A}\right)\right]\phi\right\} \tag{C.16}$$

$$= \int \mathrm{d}\vec{r}\ \left\{\phi^\dagger\left[1 + \frac{1}{4m^2c^2}\left(\vec{\boldsymbol{\sigma}} \cdot \left(\vec{p} - e\vec{A}\right)\right)^2\right]\phi\right\} \quad , \tag{C.17}$$

where we used the $\overleftarrow{p}$ notation to denote the action of $\vec{p}$ to the left and we used partial integration in the second step. Eq. (C.17) yields an expression for the renormalized big component $\tilde{\phi}$ and defines an normalization operator $\hat{N}$:

$$\tilde{\phi} = \left[1 + \frac{1}{8m^2c^2}\left(\vec{\boldsymbol{\sigma}} \cdot \left(\vec{p} - e\vec{A}\right)\right)^2\right]\phi = \hat{N}\phi = \left(1 + \frac{1}{c^2}\hat{N}_2\right)\phi \quad . \tag{C.18}$$

The Dirac equation for the big component eq. (C.4) can be written in terms of an operator $\hat{L}$,

$$\hat{L}\phi = 0 \quad , \tag{C.19}$$

which can be expanded in orders of $\frac{1}{c}$,

$$\hat{L} = \hat{L}_0 + \frac{1}{c^2}\hat{L}_2 + \mathcal{O}\left(\frac{1}{c^4}\right) \quad , \tag{C.20}$$

yielding for example the Pauli equation $\hat{L}_0\phi = 0$.
Pluggin eq. (C.7) into eq. (C.4) yields

$$\hat{L}_0 = i\hbar\frac{\partial}{\partial t} - V - mc^2 - \frac{1}{2m}\left(\vec{\boldsymbol{\sigma}}\cdot\left(\vec{p}-e\vec{A}\right)\right)^2 \tag{C.21}$$

$$\hat{L}_2 = \frac{1}{4m^2}\vec{\boldsymbol{\sigma}}\cdot\left(\vec{p}-e\vec{A}\right)\hat{L}_0\vec{\boldsymbol{\sigma}}\cdot\left(\vec{p}-e\vec{A}\right) + \frac{1}{8m^3}\left(\vec{\boldsymbol{\sigma}}\cdot\left(\vec{p}-e\vec{A}\right)\right)^4 \quad . \tag{C.22}$$

Since we want an equation for a normalized wavefunction the normalization operator has to be used:

$$\left(\hat{L}\hat{N}^{-1}\right)\left(\hat{N}\phi\right) = \left(\hat{L}\hat{N}^{-1}\right)\tilde{\phi} = 0 \quad . \tag{C.23}$$

The effective operator is given by

$$\left(\hat{L}_0 + \frac{1}{c^2}\hat{L}_2\right)\left(1 - \frac{1}{c^2}\hat{N}_2\right)\tilde{\phi} = 0 \tag{C.24}$$

$$\Rightarrow \qquad \hat{L}_0\tilde{\phi} + \frac{1}{c^2}\left(\hat{L}_2 - \hat{L}_0\hat{N}_2\right)\tilde{\phi} = 0 + \mathcal{O}\left(\frac{1}{c^4}\right) \quad . \tag{C.25}$$

Let us consider the operators $\hat{L}_2$ and $\hat{L}_0\hat{N}_2$ in more detail. Using $\hat{L}_0\phi = 0$ under the assumption that it also holds for the renormalized wavefunction yields

$$\hat{L}_0\hat{N}_2\tilde{\phi} = \left[\hat{L}_0, \hat{N}_2\right]\tilde{\phi} + \hat{N}_2\underbrace{\hat{L}_0\tilde{\phi}}_{=0} = \left[\hat{L}_0, \hat{N}_2\right]\tilde{\phi} \quad . \tag{C.26}$$

Furthermore, the same argument yields

$$\hat{L}_0\vec{\boldsymbol{\sigma}}\cdot\left(\vec{p}-e\vec{A}\right)\tilde{\phi} = \left[\hat{L}_0, \vec{\boldsymbol{\sigma}}\cdot\left(\vec{p}-e\vec{A}\right)\right]\tilde{\phi} \quad , \tag{C.27}$$

which can be simplified by using eq. (C.21):

$$\left[\hat{L}_0, \vec{\boldsymbol{\sigma}}\cdot\left(\vec{p}-e\vec{A}\right)\right] = \left[i\hbar\frac{\partial}{\partial t} - V, \vec{\boldsymbol{\sigma}}\cdot\left(\vec{p}-e\vec{A}\right)\right] \tag{C.28}$$

$$= \left(i\hbar\frac{\partial}{\partial t} - V\right)\vec{\boldsymbol{\sigma}}\cdot\left(\vec{p}-e\vec{A}\right) - \vec{\boldsymbol{\sigma}}\cdot\left(\vec{p}-e\vec{A}\right)\left(i\hbar\frac{\partial}{\partial t} - V\right) \tag{C.29}$$

$$= \vec{\boldsymbol{\sigma}}\cdot\left(-ie\hbar\frac{\partial\vec{A}}{\partial t} - i\hbar\vec{\nabla}V\right) = \vec{\boldsymbol{\sigma}}\cdot\left(ie\hbar\vec{E}\right) \quad , \tag{C.30}$$

where in the last step Maxwell's equations were used.
Using eq. (C.27) to rewrite $\hat{L}_2$ yields:

$$\hat{L}_2 = \frac{1}{4m^2}\vec{\boldsymbol{\sigma}}\cdot\left(\vec{p}-e\vec{A}\right)\left[\hat{L}_0, \vec{\boldsymbol{\sigma}}\cdot\left(\vec{p}-e\vec{A}\right)\right] + \frac{1}{8m^3}\left(\vec{\boldsymbol{\sigma}}\cdot\left(\vec{p}-e\vec{A}\right)\right)^4 \quad . \tag{C.31}$$

Inserting eq. (C.30) into eq. (C.31) yields

$$\hat{L}_2 = \frac{1}{4m^2}\vec{\boldsymbol{\sigma}}\cdot\left(\vec{p}-e\vec{A}\right)\vec{\boldsymbol{\sigma}}\cdot\left(ie\hbar\vec{E}\right) + \frac{1}{8m^3}\left(\vec{\boldsymbol{\sigma}}\cdot\left(\vec{p}-e\vec{A}\right)\right)^4 \quad . \tag{C.32}$$

In addition to $\hat{L}_2$, eq. (C.25) needs the commutator of $\left[\hat{L}_0, \hat{N}_2\right]$, which is given by

$$\left[\hat{L}_0, \hat{N}_2\right] = \frac{1}{8m^2}\left[\hat{L}_0, \left(\vec{\boldsymbol{\sigma}}\cdot\left(\vec{p}-e\vec{A}\right)\right)^2\right] \tag{C.33}$$

$$= \frac{1}{8m^2}\left(\vec{\boldsymbol{\sigma}}\cdot\left(\vec{p}-e\vec{A}\right)\vec{\boldsymbol{\sigma}}\cdot\left(ie\hbar\vec{E}\right) + \vec{\boldsymbol{\sigma}}\cdot\left(ie\hbar\vec{E}\right)\vec{\boldsymbol{\sigma}}\cdot\left(\vec{p}-e\vec{A}\right)\right) \quad . \tag{C.34}$$

Using eq. (C.10) yields for the terms in eq. (C.34)

$$\begin{aligned}\vec{\boldsymbol{\sigma}} \cdot \left(\vec{p} - e\vec{A}\right) \vec{\boldsymbol{\sigma}} \cdot \left(ie\hbar\vec{E}\right) =& ie\hbar\vec{E} \cdot \left(\vec{p} - e\vec{A}\right) + ie\hbar \left(\vec{p} \cdot \vec{E}\right) \\ &+ e\hbar\vec{\boldsymbol{\sigma}} \cdot \vec{E} \times \left(\vec{p} - e\vec{A}\right) - e\hbar\vec{\boldsymbol{\sigma}} \cdot \left(\vec{p} \times \vec{E}\right) \quad ,\end{aligned} \tag{C.35}$$

and

$$\vec{\boldsymbol{\sigma}} \cdot \left(ie\hbar\vec{E}\right) \vec{\boldsymbol{\sigma}} \cdot \left(\vec{p} - e\vec{A}\right) = ie\hbar\vec{E} \cdot \left(\vec{p} - e\vec{A}\right) - e\hbar\vec{\boldsymbol{\sigma}} \cdot \vec{E} \times \left(\vec{p} - e\vec{A}\right) \quad . \tag{C.36}$$

Collecting all terms gives

$$\begin{aligned}\frac{1}{c^2}\left(\hat{L}_2 - \hat{L}_0\hat{N}_2\right) =& \frac{1}{8m^3c^2}\left(\vec{\boldsymbol{\sigma}} \cdot \left(\vec{p} - e\vec{A}\right)\right)^4 + \frac{ie\hbar}{8m^2c^2}\left(\vec{p} \cdot \vec{E}\right) \\ &- \frac{e\hbar}{8m^2c^2}\vec{\boldsymbol{\sigma}} \cdot \left(\vec{p} \times \vec{E}\right) - \frac{e\hbar}{4m^2c^2}\vec{\boldsymbol{\sigma}} \cdot \vec{E} \times \left(\vec{p} - e\vec{A}\right) \quad ,\end{aligned} \tag{C.37}$$

which are the relativistic corrections to the Pauli Hamiltonian $\hat{L}_0$. The first term is a relativistic correction to the kinetic energy and to the Zeeman term:

$$\frac{1}{8m^3c^2}\left(\vec{\boldsymbol{\sigma}} \cdot \left(\vec{p} - e\vec{A}\right)\right)^4 = \frac{1}{8m^3c^2}\left(\left(\vec{p} - e\vec{A}\right)^2 - \mu_B\vec{\boldsymbol{\sigma}} \cdot \vec{B}\right)^2 \quad . \tag{C.38}$$

The second term is the Darwin term, which affects in case of an ionic potential only the s-electrons:

$$\frac{ie\hbar}{8m^2c^2}\left(\vec{p} \cdot \vec{E}\right) = \frac{e\hbar^2}{8m^2c^2}\left(\vec{\nabla} \cdot \vec{E}\right) \quad . \tag{C.39}$$

The third term describes relativistic corrections due to a time-dependent magnetic field:

$$-\frac{e\hbar}{8m^2c^2}\vec{\boldsymbol{\sigma}} \cdot \left(\vec{p} \times \vec{E}\right) = -i\frac{e\hbar^2}{8m^2c^2}\vec{\boldsymbol{\sigma}} \cdot \frac{\partial\vec{B}}{\partial t} \quad . \tag{C.40}$$

Finally, the last term is the spin-orbit coupling term:

$$-\frac{e\hbar}{4m^2c^2}\vec{\boldsymbol{\sigma}} \cdot \vec{E} \times \left(\vec{p} - e\vec{A}\right) \quad . \tag{C.41}$$

D. Simplified model for the correlation function

In this appendix the details of the calculation in section 6.4 are shown. The correlation function of any two observables $\hat{A}$ and $\hat{B}$ can be calculate via eq. (6.21). Using the Green function in its spectral representation

$$G(E) = \left(E - H^{eff}\right)^{-1} = \sum_{\mu,s} \frac{|\mu, s\rangle\langle\mu, s|}{E - E_{\mu,s} + i\Gamma} \tag{D.1}$$

yields for the correlation function

$$\chi_{AB}(\omega + i\eta) = -\frac{1}{\pi}\int^{E_F} \mathrm{d}E \ \mathrm{Tr} \ \left[\hat{A}G(E+\omega+i\eta)\hat{B} \ \mathrm{Im}G(E) + \hat{A} \ \mathrm{Im}G(E)\hat{B} \underbrace{G(E-\omega-i\eta)}_{=G(E-w+i\eta)^*}\right] \tag{D.2}$$

$$\begin{aligned} = -\frac{1}{2\pi i}\sum_{\mu s;\mu' s'}\int^{E_F} \mathrm{d}E \ \mathrm{Tr} \ \Bigg[\hat{A}\frac{|\mu, s\rangle\langle\mu, s|}{E+\omega-E_{\mu s}+i\Gamma}\hat{B}|\mu', s'\rangle\langle\mu', s'|\left(\frac{1}{E-E_{\mu' s'}+i\Gamma} - \frac{1}{E-E_{\mu' s'}-i\Gamma}\right) \\ + \hat{A}|\mu, s\rangle\langle\mu, s|\left(\frac{1}{E-E_{\mu s}+i\Gamma} - \frac{1}{E-E_{\mu s}-i\Gamma}\right)\hat{B}\frac{|\mu', s'\rangle\langle\mu', s'|}{E-\omega-E_{\mu' s'}-i\Gamma}\Bigg] \quad . \end{aligned} \tag{D.3}$$

The energy integration and the trace over the expectation values of the observables decouple yielding:

$$\begin{aligned} \chi_{AB}(\omega) = & -\frac{1}{2\pi i}\sum_{\mu s,\mu' s'} \mathrm{Tr} \ \left[\hat{A}|\mu s\rangle\langle\mu s|\hat{B}|\mu' s'\rangle\langle\mu' s'|\right] \\ & \times \int^{E_F} \mathrm{d}E \Bigg\{\frac{1}{E+\omega-E_{\mu s}+i\Gamma}\left(\frac{1}{E-E_{\mu' s'}+i\Gamma} - \frac{1}{E-E_{\mu' s'}-i\Gamma}\right) \\ & \qquad + \frac{1}{E-\omega-E_{\mu' s'}-i\Gamma}\left(\frac{1}{E-E_{\mu s}+i\Gamma} - \frac{1}{E-E_{\mu s}-i\Gamma}\right)\Bigg\} \quad . \end{aligned} \tag{D.4}$$

Thus one can perform the energy integration independently of the observables.
To simplify the integrand partial fraction decomposition is used:

$$\frac{1}{E-A}\frac{1}{E-B} = \frac{1}{A-B}\left(\frac{1}{E-A} - \frac{1}{E-B}\right) \quad , \tag{D.5}$$

which yields

$$
\begin{aligned}
\chi_{AB}(\omega) = &-\frac{1}{2\pi i}\sum_{\mu s,\mu' s'} \mathrm{Tr}\;\left[\hat{A}|\mu s\rangle\langle\mu s|\hat{B}|\mu' s'\rangle\langle\mu' s'|\right] \\
&\times\int^{E_F}\mathrm{d}E\left\{\frac{1}{\omega+E_{\mu' s'}-E_{\mu s}}\left(\frac{1}{E-E_{\mu' s'}+i\Gamma}-\frac{1}{E+\omega-E_{\mu s}+i\Gamma}\right)\right. \\
&\qquad -\frac{1}{\omega+E_{\mu' s'}-E_{\mu s}+2i\Gamma}\left(\frac{1}{E-E_{\mu' s'}-i\Gamma}-\frac{1}{E+\omega-E_{\mu s}+i\Gamma}\right) \\
&\qquad +\frac{1}{\omega+E_{\mu' s'}-E_{\mu s}+2i\Gamma}\left(\frac{1}{E-\omega-E_{\mu' s'}-i\Gamma}-\frac{1}{E-E_{\mu s}+i\Gamma}\right) \\
&\qquad \left.-\frac{1}{\omega+E_{\mu' s'}-E_{\mu s}}\left(\frac{1}{E-\omega-E_{\mu' s'}-i\Gamma}-\frac{1}{E-E_{\mu s}-i\Gamma}\right)\right\}
\end{aligned}
\tag{D.6}
$$

$$
\begin{aligned}
= &-\frac{1}{2\pi i}\sum_{\mu s,\mu' s'} \mathrm{Tr}\;\left[\hat{A}|\mu s\rangle\langle\mu s|\hat{B}|\mu' s'\rangle\langle\mu' s'|\right] \\
&\times\int^{E_F}\mathrm{d}E\left\{\frac{1}{\omega+E_{\mu' s'}-E_{\mu s}}\left(\frac{1}{E-E_{\mu' s'}+i\Gamma}-\frac{1}{E-\omega-E_{\mu' s'}-i\Gamma}\right.\right. \\
&\qquad\qquad \left.+\frac{1}{E-E_{\mu s}-i\Gamma}-\frac{1}{E+\omega-E_{\mu s}+i\Gamma}\right) \\
&\qquad +\frac{1}{\omega+E_{\mu' s'}-E_{\mu s}+2i\Gamma}\left(\frac{1}{E-\omega-E_{\mu' s'}-i\Gamma}-\frac{1}{E-E_{\mu' s'}-i\Gamma}\right. \\
&\qquad\qquad \left.\left.+\frac{1}{E+\omega-E_{\mu s}+i\Gamma}-\frac{1}{E-E_{\mu s}+i\Gamma}\right)\right\} \quad .
\end{aligned}
\tag{D.7}
$$

The second part of the integrand the summands cancel each other for most energies. One can calculate this part by shifting the integration interval for one summand to $E \to E \pm \omega$ leaving an energy integration from E_F to $E_F \pm \omega$:

$$
\begin{aligned}
&\int^{E_F}\mathrm{d}E\left\{\frac{1}{\omega+E_{\mu' s'}-E_{\mu s}+2i\Gamma}\left(\frac{1}{E-\omega-E_{\mu' s'}-i\Gamma}-\frac{1}{E-E_{\mu' s'}-i\Gamma}\right.\right. \\
&\qquad\qquad \left.\left.+\frac{1}{E+\omega-E_{\mu s}+i\Gamma}-\frac{1}{E-E_{\mu s}+i\Gamma}\right)\right\}
\end{aligned}
\tag{D.8}
$$

$$
=\frac{1}{\omega+E_{\mu' s'}-E_{\mu s}+2i\Gamma}\left\{\int_{E_F}^{E_F+\omega}\mathrm{d}E\frac{1}{E-E_{\mu s}+i\Gamma}-\int_{E_F-\omega}^{E_F}\mathrm{d}E\frac{1}{E-E_{\mu' s'}-i\Gamma}\right\}
\tag{D.9}
$$

$$
=\frac{1}{\omega+E_{\mu' s'}-E_{\mu s}+2i\Gamma}\left\{\ln\left(\frac{E_F+\omega-E_{\mu s}+i\Gamma}{E_F-E\mu s+i\Gamma}\right)-\ln\left(\frac{E_F-E_{\mu' s'}-i\Gamma}{E_F-\omega-E\mu' s'-i\Gamma}\right)\right\} \quad .
\tag{D.10}
$$

For the first part of the integrand we can not do this since the imaginary part differs. Thus we have to integrate over the full energy range. To overcome convergence problems a lower bound energy E_B is introduced.

In total, we obtain for the correlation function

$$
\begin{aligned}
\chi_{AB}(\omega) = &-\frac{1}{2\pi i} \sum_{\mu s,\mu' s'} \mathrm{Tr}\ \Big[\hat{A}|\mu s\rangle\langle\mu s|\hat{B}|\mu' s'\rangle\langle\mu' s'|\Big] \\
&\times \Bigg[\frac{1}{E_{\mu' s'} - E_{\mu s} + \omega} \Bigg\{\frac{1}{2}\ln\big((E_F - E_{\mu' s'})^2 + \Gamma^2\big) + i\arctan\left(\frac{\Gamma}{E_F - E_{\mu' s'}}\right) \\
&\qquad - \frac{1}{2}\ln\big((E_F - \omega - E_{\mu' s'})^2 + \Gamma^2\big) + i\arctan\left(\frac{\Gamma}{E_F - \omega - E_{\mu' s'}}\right) \\
&\qquad + \frac{1}{2}\ln\big((E_F - E_{\mu s})^2 + \Gamma^2\big) - i\arctan\left(\frac{\Gamma}{E_F - E_{\mu s}}\right) \\
&\qquad - \frac{1}{2}\ln\big((E_F + \omega - E_{\mu s})^2 + \Gamma^2\big) - i\arctan\left(\frac{\Gamma}{E_F + \omega - E_{\mu s}}\right) \\
&\qquad - \frac{1}{2}\ln\big((E_B - E_{\mu' s'})^2 + \Gamma^2\big) - i\arctan\left(\frac{\Gamma}{E_B - E_{\mu' s'}}\right) \\
&\qquad + \frac{1}{2}\ln\big((E_B - \omega - E_{\mu' s'})^2 + \Gamma^2\big) - i\arctan\left(\frac{\Gamma}{E_B - \omega - E_{\mu' s'}}\right) \\
&\qquad - \frac{1}{2}\ln\big((E_B - E_{\mu s})^2 + \Gamma^2\big) + i\arctan\left(\frac{\Gamma}{E_B - E_{\mu s}}\right) \\
&\qquad + \frac{1}{2}\ln\big((E_B + \omega - E_{\mu s})^2 + \Gamma^2\big) + i\arctan\left(\frac{\Gamma}{E_B + \omega - E_{\mu s}}\right)\Bigg\} \\
&+ \frac{1}{\omega + E_{\mu' s'} - E_{\mu s} + 2i\Gamma} \Bigg\{\frac{1}{2}\ln\big((E_F + \omega - E_{\mu s})^2 + \Gamma^2\big) + i\arctan\left(\frac{\Gamma}{E_F + \omega - E_{\mu s}}\right) \\
&\qquad - \frac{1}{2}\ln\big((E_F - E_{\mu s})^2 + \Gamma^2\big) - i\arctan\left(\frac{\Gamma}{E_F - E_{\mu s}}\right) \\
&\qquad - \frac{1}{2}\ln\big((E_F - E_{\mu' s'})^2 + \Gamma^2\big) + i\arctan\left(\frac{\Gamma}{E_F - E_{\mu' s'}}\right) \\
&\qquad + \frac{1}{2}\ln\big((E_F - \omega - E_{\mu' s'})^2 + \Gamma^2\big) - i\arctan\left(\frac{\Gamma}{E_F - \omega - E_{\mu' s'}}\right)\Bigg\}\Bigg]
\end{aligned}
\tag{D.11}
$$

$$
= \sum_{\mu s,\mu' s'} \mathrm{Tr}\ \Big[\hat{A}|\mu s\rangle\langle\mu s|\hat{B}|\mu' s'\rangle\langle\mu' s'|\Big]\, \tilde{\chi}_{\mu s,\mu' s'}(\omega) \quad . \tag{D.12}
$$

Bibliography

[1] G. Binasch, P. Grünberg, F. Saurenbach, and W. Zinn, "Enhanced magnetoresistance in layered magnetic structures with antiferromagnetic interlayer exchange," *Physical Review B*, vol. 39, no. 7, pp. 4828–4830, Mar. 1989. [Online]. Available: http://link.aps.org/doi/10.1103/PhysRevB.39.4828

[2] M. N. Baibich, J. M. Broto, A. Fert, F. N. Van Dau, F. Petroff, P. Etienne, G. Creuzet, A. Friederich, and J. Chazelas, "Giant Magnetoresistance of (001)Fe/(001)Cr Magnetic Superlattices," *Physical Review Letters*, vol. 61, no. 21, pp. 2472–2475, Nov. 1988. [Online]. Available: http://link.aps.org/doi/10.1103/PhysRevLett.61.2472

[3] S. A. Wolf, D. D. Awschalom, R. A. Buhrman, J. M. Daughton, S. von Molnár, M. L. Roukes, A. Y. Chtchelkanova, and D. M. Treger, "Spintronics: A Spin-Based Electronics Vision for the Future," *Science*, vol. 294, no. 5546, pp. 1488–1495, 2001, bibtex: Wolf1488. [Online]. Available: http://science.sciencemag.org/content/294/5546/1488

[4] S. Maekawa, *Spin current*, 1st ed., ser. Oxford science publications. Oxford: Oxford University Press, 2012, no. 17.

[5] Y. Tserkovnyak, A. Brataas, and G. E. W. Bauer, "Enhanced Gilbert Damping in Thin Ferromagnetic Films," *Physical Review Letters*, vol. 88, no. 11, Feb. 2002. [Online]. Available: http://link.aps.org/doi/10.1103/PhysRevLett.88.117601

[6] S. Loth, K. von Bergmann, M. Ternes, A. F. Otte, C. P. Lutz, and A. J. Heinrich, "Controlling the state of quantum spins with electric currents," *Nature Physics*, vol. 6, no. 5, pp. 340–344, May 2010. [Online]. Available: http://www.nature.com/nphys/journal/v6/n5/full/nphys1616.html

[7] P. Strange, *Relativistic Quantum Mechanics.* Cambridge University Press, 1998.

[8] P. Bruno, "Tight-binding approach to the orbital magnetic moment and magnetocrystalline anisotropy of transition-metal monolayers," *Physical Review B*, vol. 39, no. 1, pp. 865–868, Jan. 1989. [Online]. Available: http://link.aps.org/doi/10.1103/PhysRevB.39.865

[9] E. I. Rashba, "Properties of semiconductors with an extremum loop .1. Cyclotron and combinational resonance in a magnetic field perpendicular to the plane of the loop," *Soviet Physics Solid State*, vol. 2, no. 1109, 1960.

[10] G. Dresselhaus, "Spin-orbit coupling effects in zinc blende structures," *Physical Review*, vol. 100, no. 2, p. 580, 1955. [Online]. Available: http://journals.aps.org/pr/abstract/10.1103/PhysRev.100.580

[11] I. Dzyaloshinsky, "A thermodynamic theory of weak ferromagnetism of antiferromagnetics,"

Journal of Physics and Chemistry of Solids, vol. 4, no. 4, pp. 241–255, 1958. [Online]. Available: http://www.sciencedirect.com/science/article/pii/0022369758900763

[12] T. Moriya, “Anisotropic superexchange interaction and weak ferromagnetism,” *Physical Review*, vol. 120, no. 1, p. 91, 1960. [Online]. Available: http://journals.aps.org/pr/abstract/10.1103/PhysRev.120.91

[13] J. D. Jackson, *Classical Electrodynamics*, 3rd ed. John Wiley & Sons, Inc., 1999.

[14] A. S. Davydov, *Quantum Mechanics.* Oxford: Pergamon, 1965.

[15] T. Thonhauser, “Theory of orbital magnetization in solids,” *International Journal of Modern Physics B*, vol. 25, no. 11, pp. 1429–1458, Apr. 2011. [Online]. Available: http://www.worldscientific.com/doi/abs/10.1142/S0217979211058912

[16] S. Qiao, A. Kimura, H. Adachi, K. Iori, K. Miyamoto, T. Xie, H. Namatame, M. Taniguchi, A. Tanaka, T. Muro, S. Imada, and S. Suga, “Direct evidence of ferromagnetism without net magnetization observed by x-ray magnetic circular dichroism,” *Physical Review B*, vol. 70, no. 13, p. 134418, Oct. 2004. [Online]. Available: http://link.aps.org/doi/10.1103/PhysRevB.70.134418

[17] J.-P. Hanke, F. Freimuth, A. K. Nandy, H. Zhang, S. Blügel, and Y. Mokrousov, “Role of Berry phase theory for describing orbital magnetism: From magnetic heterostructures to topological orbital ferromagnets,” *Physical Review B*, vol. 94, no. 12, p. 121114, Sep. 2016. [Online]. Available: http://link.aps.org/doi/10.1103/PhysRevB.94.121114

[18] L. L. Hirst, “The microscopic magnetization: concept andapplication,” *Reviews of Modern Physics*, vol. 69, no. 2, pp. 607–628, Apr. 1997. [Online]. Available: http://link.aps.org/doi/10.1103/RevModPhys.69.607

[19] T. Thonhauser, D. Ceresoli, D. Vanderbilt, and R. Resta, “Orbital Magnetization in Periodic Insulators,” *Physical Review Letters*, vol. 95, no. 13, p. 137205, Sep. 2005. [Online]. Available: http://link.aps.org/doi/10.1103/PhysRevLett.95.137205

[20] I. Souza and D. Vanderbilt, “Dichroic \$f\$-sum rule and the orbital magnetization of crystals,” *Physical Review B*, vol. 77, no. 5, p. 054438, Feb. 2008. [Online]. Available: http://link.aps.org/doi/10.1103/PhysRevB.77.054438

[21] R. M. Martin, *Electronic Structure Basic Theory and Practical Methods.* Cambridge University Press, 2004.

[22] M. Born and R. Oppenheimer, “Zur Quantentheorie der Molekeln,” *Annalen der Physik*, vol. 389, no. 20, pp. 457–484, 1927. [Online]. Available: http://onlinelibrary.wiley.com/doi/10.1002/andp.19273892002/abstract

[23] P. Hohenberg and W. Kohn, “Inhomogeneous Electron Gas,” *Physical Review*, vol. 136, no. 3B, pp. B864–B871, 1964.

[24] W. Kohn and L. J. Sham, “Self-Consistent Equations Including Exchange and Correlation Effects,” *Physical Review*, vol. 140, no. 4A, pp. A1133–A1138, 1965.

[25] S. H. Vosko, L. Wilk, and M. Nusair, "Accurate spin-dependent electron liquid correlation energies for local spin density calculations: a critical analysis," *Canadian Journal of physics*, vol. 58, no. 8, pp. 1200–1211, 1980. [Online]. Available: http://www.nrcresearchpress.com/doi/abs/10.1139/p80-159

[26] M. A. L. Marques, C. A. Ulrich, F. Nogueira, A. Rubio, K. Burke, and E. K. U. Gross, *Time-Dependent Density Functional Theory.* Springer-Verlag Berlin Heidelberg, 2006.

[27] E. Runge and E. K. U. Gross, "Density-functional theory for time-dependent systems," *Physical Review Letters*, vol. 52, no. 12, p. 997, 1984. [Online]. Available: http://journals.aps.org/prl/abstract/10.1103/PhysRevLett.52.997

[28] G. Vignale and M. Rasolt, "Density-functional theory in strong magnetic fields," *Physical Review Letters*, vol. 59, no. 20, pp. 2360–2363, Nov. 1987. [Online]. Available: http://link.aps.org/doi/10.1103/PhysRevLett.59.2360

[29] H. Ebert, M. Battocletti, and E. K. U. Gross, "Current density functional theory of spontaneously magnetised solids," *Europhysics Letters (EPL)*, vol. 40, no. 5, pp. 545–550, Dec. 1997. [Online]. Available: http://stacks.iop.org/0295-5075/40/i=5/a=545?key=crossref.fef63e9b35b0e242ce4cce8c54285ea6

[30] K. Capelle, G. Vignale, and B. L. Györffy, "Spin Currents and Spin Dynamics in Time-Dependent Density-Functional Theory," *Physical Review Letters*, vol. 87, no. 20, Oct. 2001. [Online]. Available: http://link.aps.org/doi/10.1103/PhysRevLett.87.206403

[31] J. Korringa, "On the calculation of the energy of a Bloch wave in a metal," *Physica*, vol. 13, no. 6-7, pp. 392–400, 1947. [Online]. Available: http://www.sciencedirect.com/science/article/pii/003189144790013X

[32] W. Kohn and N. Rostoker, "Solution of the Schr\"odinger Equation in Periodic Lattices with an Application to Metallic Lithium," *Physical Review*, vol. 94, no. 5, pp. 1111–1120, 1954.

[33] J. Zabloudil, *Electron scattering in solid matter: a theoretical and computational treatise*, ser. Springer series in solid-state sciences. Berlin ; New York: Springer, 2005, no. 147.

[34] J. Grotendorst and Forschungszentrum, *Computational nanoscience: do it yourself!: winter school, 14-22 February 2006, Forschungszentrum Jülich, Germany ; lecture notes.* Jülich: NIC, 2006.

[35] H. Bruus and K. Flensberg, *Many-Body Quantum Theory in Condensed Matter Physics.* Oxford University Press, 2004.

[36] D. S. G. Bauer, "Development of a relativistic full-potential first-principles multiple scattering Green function method applied to complex magnetic textrues of nano structures at surfaces," Phd Thesis, Juelich, 2013.

[37] M. dos Santos Dias, B. Schweflinghaus, S. Blügel, and S. Lounis, "Relativistic dynamical spin excitations of magnetic adatoms," *Physical Review B*, vol. 91, no. 7, Feb. 2015. [Online]. Available: http://link.aps.org/doi/10.1103/PhysRevB.91.075405

[38] B. Schweflinghaus, "First-principles investigation of inelastic magnetic excitations in nanos-

tructures deposited on surfaces," Phd thesis, RWTH Aachen, 2015.

[39] N. Papanikolaou, R. Zeller, and P. H. Dederichs, "Conceptual improvements of the KKR method," *Journal of Physics: Condensed Matter*, vol. 14, pp. 2799–2823, 2002. [Online]. Available: http://iopscience.iop.org/article/10.1088/0953-8984/14/11/304/meta;jsessionid=9E4A8D49EF298BA74E84E7077230B6B0.c1.iopscience.cld.iop.org

[40] M. dos Santos Dias, J. Bouaziz, M. Bouhassoune, and S. Lounis, "Chirality-driven orbital magnetic moments: fingerprints of topological magnetic structures," *ArXiv e-prints*, 2016.

[41] P. Giannozzi, S. Baroni, N. Bonini, M. Calandra, R. Car, C. Cavazzoni, D. Ceresoli, G. L. Chiarotti, M. Cococcioni, I. Dabo, A. D. Corso, S. d. Gironcoli, S. Fabris, G. Fratesi, R. Gebauer, U. Gerstmann, C. Gougoussis, A. Kokalj, M. Lazzeri, L. Martin-Samos, N. Marzari, F. Mauri, R. Mazzarello, S. Paolini, A. Pasquarello, L. Paulatto, C. Sbraccia, S. Scandolo, G. Sclauzero, A. P. Seitsonen, A. Smogunov, P. Umari, and R. M. Wentzcovitch, "QUANTUM ESPRESSO: a modular and open-source software project for quantum simulations of materials," *Journal of Physics: Condensed Matter*, vol. 21, no. 39, p. 395502 (19pp), 2009. [Online]. Available: http://www.quantum-espresso.org

[42] P. W. Anderson, "Localized Magnetic States in Metals," *Physical Review*, vol. 124, no. 1, pp. 41–53, Oct. 1961. [Online]. Available: http://link.aps.org/doi/10.1103/PhysRev.124.41

[43] J. Friedel, "The distribution of electrons round impurities in monovalent metals," *The London, Edinburgh, and Dublin Philosophical Magazine and Journal of Science*, vol. 43, no. 337, pp. 153–189, Feb. 1952. [Online]. Available: http://dx.doi.org/10.1080/14786440208561086

[44] G. Tatara and N. Garcia, "Quantum Toys for Quantum Computing: Persistent Currents Controlled by the Spin Josephson Effect," *Physical Review Letters*, vol. 91, no. 7, Aug. 2003. [Online]. Available: http://link.aps.org/doi/10.1103/PhysRevLett.91.076806

[45] S. Lounis, "Non-collinear magnetism induced by frustration in transition-metal nanostructures deposited on surfaces," *Journal of Physics: Condensed Matter*, vol. 26, no. 27, p. 273201, Jul. 2014. [Online]. Available: http://stacks.iop.org/0953-8984/26/i=27/a=273201?key=crossref.4db0c776a67a887bb5dc11bb36642abb

[46] E. I. Rashba, "Spin currents in thermodynamic equilibrium: The challenge of discerning transport currents," *Physical Review B*, vol. 68, no. 24, Dec. 2003. [Online]. Available: http://link.aps.org/doi/10.1103/PhysRevB.68.241315

[47] A. Fetter and J. Walecka, *Quantum Theory of Many-Particle Systems.* Dover Publications, 2003.

[48] G. Giuliani and G. Vignale, *Quantum Theory of the Electron Liquid.* Leiden: Cambridge University Press, 2005. [Online]. Available: http://public.eblib.com/choice/publicfullrecord.aspx?p=347182

[49] M. Bouhassoune, M. d. S. Dias, B. Zimmermann, P. H. Dederichs, and S. Lounis, "RKKY-like contributions to the magnetic anisotropy energy: $3d$ adatoms on Pt(111) surface," *Physical Review B*, vol. 94, no. 12, p. 125402, Sep. 2016. [Online]. Available: http://link.aps.org/doi/10.1103/PhysRevB.94.125402

[50] D. M. Crum, M. Bouhassoune, J. Bouaziz, B. Schweflinghaus, S. Blügel, and S. Lounis, "Perpendicular reading of single confined magnetic skyrmions," *Nature Communications*, vol. 6, p. 8541, Oct. 2015. [Online]. Available: http://www.nature.com/doifinder/10.1038/ncomms9541